

**Synthetic modulation of layer dependent  
MoS<sub>2</sub> nanosheet and enhanced  
electrochemical HER and ORR kinetics  
through Zinc doping**

*A thesis submitted towards partial fulfillment of the  
requirements for the degree of*

**Master of Technology in Nano science and Technology**

*Submitted by:*

***Md Imran Ansari***

**Examination Roll No.: M4NST22020**

**Registration No.: 154589 of 2020-2021**

**Prof. (Dr).Kalyan Kumar Chattopadhyay**

**School of Materials Science and Nanotechnology**

**Jadavpur University**

**Kolkata -700032**

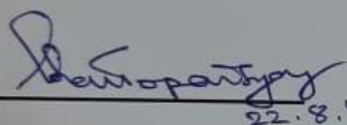
**COURSE AFFILIATED TO  
FACULTY OF INTERDISCIPLINARY STUDIES,  
LAW AND MANAGEMENT  
JADAVPUR UNIVERSITY  
KOLKATA-700032  
INDIA**

**2022**

M.Tech. (Nano science and Technology)  
Course affiliated to  
Faculty of Interdisciplinary Studies,  
Law and Management  
Jadavpur University  
Kolkata, India

## CERTIFICATE OF RECOMMENDATION

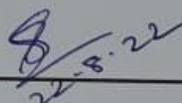
This is to certify that MD IMRAN ANSARI's thesis, "Synthetic modulation of layer dependent MoS<sub>2</sub> nanosheet and enhanced electrochemical HER and ORR kinetics through Zinc doping," is a genuine piece of work completed under our direction and supervision in part to fulfill the requirements for the Master of Technology in Nano science and Technology at the School of Materials Science and Nanotechnology for the academic year 2020–2022.

  
22.8.22

**THESIS ADVISOR**

**Dr. Kalyan Kumar Chattopadhyay**  
School of Materials Science and  
Nanotechnology  
Jadavpur University, Kolkata-700032

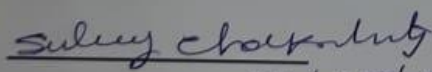
Prof. Kalyan Kr. Chattopadhyay  
Professor and Head  
Department of Physics  
Jadavpur University  
Kolkata-700 032

  
22.8.22

**DIRECTOR**

**Dr. Sourav Sarkar**  
School of Materials Science and  
Nanotechnology  
Jadavpur University, Kolkata-700032

Dr. Sourav Sarkar  
Director  
Associate Professor  
School of Materials Science & Nanotechnology  
Jadavpur University  
Kolkata-700032

  
22/08/2022

**DEAN**

Faculty Council of Interdisciplinary Studies  
Law and Management  
Jadavpur University, Kolkata-700032

Dean  
Faculty of Interdisciplinary Studies  
Law & Management  
Jadavpur University, Kolkata-700032

**M.Tech. (Nano science and Technology)**  
**Course affiliated to**  
**Faculty of Interdisciplinary Studies,**  
**Law and Management**  
**Jadavpur University**  
**Kolkata, India**

---

**CERTIFICATE OF APPROVAL \*\***

This foregoing thesis is hereby approved as a credible study of an engineering subject carried out and presented in a manner satisfactorily to warranty its acceptance as a prerequisite to the degree for which it has been submitted. It is understood that by this approval the undersigned do not endorse or approve any statement made or opinion expressed or conclusion drawn therein but approve the thesis only for purpose for which it has been submitted.

**Committee of final examination**

**for evaluation of Thesis**

---

---

---

---

**\*\* Only in case the thesis is approved.**

## **DECLARATION OF ORIGINALITY AND COMPLIANCE OF ACADEMIC ETHICS**

I hereby certify that the undersigned candidate completed the literature review and original research for this thesis as a requirement for his **Master of Technology (Nano science and Technology)** studies during the academic year **2020–2022**.

All information in this document has been obtained and presented in accordance with academic standards and ethical conduct.

I further declare that I have properly cited and referred to all information and findings that are not original to this work, as required by these rules and conduct.

**Name: MD IMRAN ANSARI**

**Examination Roll Number: M4NST22020**

**Registration Number: 154589 of 2020-2021**

**Thesis Title: Synthetic modulation of layer dependent MoS<sub>2</sub> nanosheet and enhanced electrochemical HER and ORR kinetics through Zinc doping.**

**SIGNATURE:**

**DATE:**

Dedicated to my parents

# Acknowledgement

First and foremost, I would like to convey my sincere gratitude to my supervisor, **Prof. (Dr). Kalyan Kumar Chattopadhyay**, for his direction and counsel during this research project as well as for providing me with exceptional experiences. He gave me the ongoing inspiration and assistance I most needed in a number of ways. I also want to thank you for welcoming me into the "Thin Film & Nano science" lab and for the excellent working atmosphere that makes it possible for me to do extended study there. All of these gave me tremendous support and enabled me to get through my project's challenging times; without them, I don't believe I could have finished it.

I want to express my sincere thanks to my mentor, **Mr. Dipayan Roy**, for his suggestions, guidance, and essential assistance during my work. His assistance and kind collaboration are just above my comprehension.

I would also like to express my sincere gratitude to Dr. Sourav Sarkar, Dr. Mahua Ghosh, and Dr. Chandan Kumar Ghosh for their help, support, encouragement, suggestion and advice during the course of the research. Their enthusiasm provided me a helpful and effective way of learning which in turn inspired me to follow the research project with great enthusiasm.

I want to express my sincere thanks to Brajesh Kumar and Pravin Kumar Saini for their continuous support and motivation throughout my work. Without their encouragement, I would not have been able to finish my job. In light of their enormous support, the thanks I express to them are insufficient.

I also want to sincerely thank Himanshu Shekhar, Tanay Toppo, Manas Thakur, Dipa Bala Sarkar, Swagata Das, Mrinmoy Patra, and Avinash Shaw for their help and encouragement during the course of my project work.

For making my project an amazing experience, I would like to express my sincere gratitude to my seniors, Sk Najes Riaz, Ankita Chandra, Dimitra Das, Bikram Kumar Das, Nabanita Sen, Ratna Sarkar, Suvankar Mondal, Suvankar Poddar, Anibrata Banerjee, Arnab Das, Karamjyoti Panigrahi, Antika Das, and all my seniors. They also gave me many insightful scientific ideas that motivated me to keep working hard.

Finally, I want to specifically thank my parents and all of my supporters for their unwavering love, support, and encouragement.

# **Abstract**

The works presented in the thesis “Synthetic modulation of layer dependent MoS<sub>2</sub> nanosheet and enhanced electrochemical HER and ORR kinetics through Zinc doping” has its prime focus on two things: first, to synthesize 2H-MoS<sub>2</sub> nanosheet and separate its different layers without metal intercalation, and second, to measure the HER and ORR kinetics of different concentrations of Zinc doped in MoS<sub>2</sub>.

Due to both its novel physical properties and its potential for use, the two-dimensional nanomaterial MoS<sub>2</sub> is extremely fascinating. The utilisation of liquid exfoliation, a vital production method, is constrained by our inability to quickly and correctly monitor nanosheet size, thickness, or concentration. We have developed a simple and flexible centrifugation strategy based on Band sedimentation to rapidly sort liquid-suspended TMDs according to their mass using a conventional tabletop centrifuge. This procedure resulted in a range of fractions (samples) with distinctly different extinction spectra. While the measurements of size and thickness are based on the influence of edges and quantum confinement on the optical spectra, the concentration measurement is based on the size independence of the low-wavelength extinction coefficient. The controllability of concentration, size, and thickness that results makes it simpler to produce dispersions with predetermined characteristics, including high monolayer content. These techniques are generic and can be used to a wide range of two-dimensional materials, including WS<sub>2</sub>, MoSe<sub>2</sub>, and WSe<sub>2</sub>.

For the advancement of future energy, non-noble metal electrocatalysts with superior performance and financial advantages for the hydrogen evolution reaction (HER) and oxygen reduction reaction (ORR) are essential. MoS<sub>2</sub> based materials in particular, which are two-dimensional transition-metal sulphides, are thought to be excellent substitute catalysts for the HER and ORR, where doping engineering has shown to be an efficient technique to modify their electrocatalytic activity. In this work, we have reported that Zn-doped MoS<sub>2</sub> exhibits increased electrochemical activity when compared to pure MoS<sub>2</sub>. The produced Zn-doped MoS<sub>2</sub> (MoS<sub>2</sub>-30) exhibits outstanding HER and ORR performance. Doping engineering thus offers an effective way to increase the intrinsic activity of transition-metal sulphides and may aid in the creation of nonprecious electrocatalysts for HER and ORR.

# **Table of Contents**

<b>Certificate of Recommendation.....</b>	<b>i</b>
<b>Certificate of Approval.....</b>	<b>ii</b>
<b>Declaration.....</b>	<b>iii</b>
<b>Acknowledgement.....</b>	<b>iv</b>
<b>Abstract.....</b>	<b>v</b>
<b>Chapter 1</b>	
<b>1. Introduction.....</b>	<b>1-20</b>
1.1 Semiconductor.....	1
1.2 Nanoscience and technology.....	2
1.3 Vision of Nanotechnology.....	3
1.4 History and development in Nanoscience and technology.....	4
1.5 Classification of Nanomaterials.....	6
1.5.1 Zero dimensional materials (0-D).....	8
1.5.2 One dimensional materials (1-D).....	8
1.5.3 Two dimensional materials (2-D).....	9
1.6 Optical and Electrical properties of nanomaterials.....	9
1.6.1 Transmittance and Absorption.....	9
1.6.2 Electrical Conductivity.....	9
1.7 Why 2-D materials? .....	10
1.8 Introduction of MoS <sub>2</sub> .....	12
1.8.1 Crystal structures of MoS <sub>2</sub> .....	13
1.8.2 Different synthesis methods of MoS <sub>2</sub> .....	14
1.9 Objectives of the work.....	15
<b>References.....</b>	<b>16</b>



## Chapter 2

<b>2. Introduction to HER and ORR.....</b>	<b>21-38</b>
2.1 Introduction to Hydrogen Evolution Reaction (HER).....	21
2.2 Mechanisms of Electrochemical HER.....	22
2.2.1 HER in Acidic Media.....	22
2.2.2 HER in Alkaline Media.....	23
2.3 General Approaches for Evaluating catalytic performance.....	24
2.3.1 Overpotential.....	24
2.3.2 Tafel Slope and Exchange Current Density.....	25
2.3.3 Turnover Frequency.....	25
2.3.4 Stability.....	26
2.4 Introduction to Oxygen Reduction Reaction (ORR).....	27
2.5 Electrochemical O <sub>2</sub> reduction reactions.....	27
2.6 Mechanism of ORR.....	28
2.7 Techniques used in Electrocatalytic O <sub>2</sub> reduction.....	30
2.7.1 Steady state polarization.....	30
2.7.2 Cyclic voltammetry.....	31
2.7.3 Rotating disk electrode (RDE).....	32
2.7.4 Rotating ring-disk electrode (RRDE).....	32
2.8 Kinetics of Oxygen reduction reaction.....	33
2.8.1 Tafel Slope.....	34
2.8.2 Exchange current density.....	34
References.....	35

## Chapter 3

<b>3. Review of Past work.....</b>	<b>39-53</b>
3.1 General Idea.....	39
3.2 Synthesis and Characterization of MoS <sub>2</sub> nanosheets.....	39
3.2.1 Ion-intercalation/Exfoliation Methods.....	40
3.2.2 Surfactant/Polymer-Assisted Exfoliation Methods.....	41
3.2.3 Solvent-Assisted Exfoliation Methods.....	42
3.2.4 Sonication Methods.....	42
3.2.5 Wet chemical synthesis Methods.....	43
3.3 Sorting and separation strategies.....	44
3.4 Heteroatom doping in MoS <sub>2</sub> .....	45
3.4.1 Metal-Atom doping.....	45
3.4.2 Non-metal-Atom doping.....	46
3.4.3 Zn doping.....	47
References.....	49

## Chapter 4

<b>4. Instruments and Apparatus.....</b>	<b>54-71</b>
4.1 Crystal structure Analyses.....	54
4.1.1 X-RAY Diffractometer.....	54
4.2 Optical property Analysis.....	57
4.2.1 Ultraviolet Visible Spectrophotometer.....	57
4.2.2 Raman Analysis.....	61
4.3 Morphological Analysis.....	63
4.3.1 Field Emission Scanning Electron Microscope (FESEM).....	63
4.4 Surface Analysis.....	67
4.4.1 X-Ray Photoelectron Spectroscopy.....	67

4.5 Electrochemical property Analysis.....	70
4.5.1 Cyclic Voltammetry.....	70

## Chapter 5

<b>5. Layer separation of 2H-MoS<sub>2</sub> without metal intercalation.....</b>	<b>72-88</b>
5.1 Introduction.....	72
5.2 Experimental section.....	74
5.2.1 Sample preparation.....	74
5.2.1.1 Exfoliation/synthesis of 2H-MoS <sub>2</sub> nanosheet.....	74
5.2.1.2 Preparation of layer separation of 2H-MoS <sub>2</sub> nanosheet..	74
5.2.2 Characterizations.....	75
5.3 Results and discussion.....	76
5.3.1 Size selection of MoS <sub>2</sub> nanosheets.....	76
5.3.2 Length metric based on nanosheet edge effects.....	78
5.3.3 The effect of nanosheet length on optical spectra.....	79
5.3.4 Surface Analysis.....	80
5.3.5 Crystal structure Analysis.....	80
5.3.6 Raman and FT-IR Analysis.....	82
5.3.7 Optical Analysis.....	83
5.4 Conclusion.....	84
References.....	85

## Chapter 6

<b>6. HER and ORR kinetics of Zn doped MoS<sub>2</sub>.....</b>	<b>89-105</b>
6.1 Introduction.....	89
6.2 Experimental section.....	91
6.2.1 Sample preparation.....	91
6.2.1.1 Hydrothermal synthesis of Zinc doped MoS <sub>2</sub> .....	91
6.2.2 Characterizations.....	92
6.2.3 Electrochemical property measurements.....	92
6.3 Results and discussion.....	94
6.3.1 Structural and Raman Study.....	94
6.3.2 Morphology Study.....	95
6.3.3 Surface Study.....	95
6.3.4 Experimental HER activity.....	97
6.3.5 Experimental ORR activity.....	99
6.4 Conclusion.....	101
References.....	102

## Chapter 7

<b>7. Conclusion and Scope for Future works.....</b>	<b>106-107</b>
7.1 Conclusion.....	106
7.2 Scope for Future works.....	107

# **CHAPTER 1**

## **INTRODUCTION**

## 1.1 Semiconductor

A semiconductor is a material, typically a solid chemical element or compound having band gap in the range of 1- 3 eV. Generally semiconductor devices transmit electricity in some situations but not in others, making it an effective medium for controlling electrical current. The amount of current or voltage provided to a control electrode, or the intensity of infrared (IR), visible light, ultraviolet (UV), or X-ray radiation, affects the conductance of the material. Group IV of the periodic table contains certain pure semiconducting elements (such as silicon or germanium). Some ternary compounds as well as some binary compounds, particularly those involving elements of groups III-V, II-VI, IV-VI, and between various elements of group IV, exhibit semiconducting properties.

The impurities or dopants that are added to a semiconductor determine its unique properties. Similar to the flow of current in a wire, an N-type semiconductor mostly transports negatively charged electrons. In a P-type semiconductor, holes are the most common form of current transport. A hole has an effective electric charge that is positive, the exact opposite of what an electron has. The direction of the flow of holes in a semiconductor material is the exact opposite of the direction of the flow of electrons [1]. High electrical resistivity is found in insulators, while high electrical conductivity is found in metals. However, semiconductors' electrical conductivity can vary by several orders of magnitude. The foundation of modern electronics is now semiconductors because of their distinctive feature. With the invention of transistors and microprocessor processors, human lifestyle has transformed.

Scientists have achieved major and quick advancements in the field of semiconductor physics throughout the past century. Due to their numerous practical uses in things like solar cells [2], photo electrochemical [3], sensors [4], photo luminescence devices [5], photocatalysts [6], etc., semiconductor materials have drawn a lot of attention. In addition to these, they offer essential understandings of the involved electronic processes. Material processing has consequently grown in significance as a topic of study. There are presently many novel materials on the market that have particular qualities for particular uses. But the biggest obstacle to the development of new technologies is frequently material constraints. The synthesis of materials with high performance multifunctional functions and the discovery of low cost, high yield synthesis methods are currently of considerable interest to material scientists.

## 1.2 Nanoscience and technology

In order to push the frontiers of the nanoscale, material scientists, mechanical and electrical engineers, biologists, chemists, and physicists collaborate in the field of nanotechnology. In essence, it is the engineering of molecularly scaled functional systems [7, 8]. This covers both the most recent research and more complex ideas. The term "nanotechnology" originally referred to the anticipated capacity to build things from the bottom up utilising currently being developed tools and processes to create complete, high performance products.

The following definition is provided by the United States National Nanotechnology Initiative (NNI): Understanding and manipulating matter at scales between 1 and 100 nanometers, where unique phenomena enable for novel applications, is known as nanotechnology [7]. Nanotechnology includes imaging, measuring, modelling, and manipulating materials at this scale. Nanoscale science, engineering, and technology are all included in this field.

"Nanotechnology is the principle of manipulation atom by atom, through control of the structure of matter at the molecular level. It entails the ability to build molecular systems with atom-by-atom precision, yielding a variety of nanomachines"-K. Eric Drexler.

When K. Eric Drexler first used the term "nanotechnology" in the 1980s, he was referring to the construction of motors, robot arms, and even entire computers that were much smaller than a cell, on the scale of molecules, a few nanometers across. The following ten years were devoted to Drexler's description and analysis of these amazing machines as well as his denial of claims that they were science fiction. On a molecular level, mundane technology was becoming capable of creating straightforward structures. As the idea of nanotechnology gained acceptance, the definition of the term changed to include the more basic forms of nanometer-scale technology. This type of nanotechnology is covered by the U.S. National Nanotechnology Initiative, which defines it as anything with unique properties that is smaller than 100 nanometers. The eminent physicist Richard Feynman foresaw this potential capability as early as 1959.

"I want to build a billion tiny factories, models of each other, which are manufacturing simultaneously. The principles of physics, as far as I can see, do not speak against the possibility of maneuvering things atom by atom. It is not an attempt to violate any laws; it is something, in principle, that can be done; but in practice, it has not been done because we are too big."- Richard Feynman, Nobel Prize winner in physics.

The word "nano" is a scientific jargon term that derives from the Greek word for dwarf and signifies one billionth [9]. A nanometer, often known as 1 nm, is one billionth of a meter. We frequently use the analogy of a human hair to demonstrate how little a thing is. The typical diameter of a human hair is around 50,000 nanometers, so that gives you an idea of the nanoscale. The tiniest features that can now be etched on a commercial microprocessor are less than 100 nm, in contrast. The smallest object that the human eye can resolve without assistance is 10,000 nm in size.

### **1.3 Vision of Nanotechnology**

Richard Feynman, a 1959 Nobel laureate, initially presented the original idea that had a significant influence on the direction of nanoscience in a speech at the American Physical Society's annual conference on December 29, 1959 [10]. "There's Plenty of Room at the Bottom," with the following illustrations by Feynman:

"I would like to describe a field, in which little has been done, but in which an enormous amount can be done in principle. This field is not quite the same as the others in that it will not tell us much of fundamental physics (in the sense of, "What are the strange particles?") But it is more like solid state Physics in the sense that it might tell us much of great interest about the strange phenomena that occur in complex situations. Furthermore, a point that is most important is that it would have an enormous number of Technical applications."

This serves as a reminder that, under a reductionist worldview—that is, one that attempts to limit the description of the universe to the same mathematical equations—Nano science does not provide us with any basic insights into the nature of the universe. This is so because nanoscience only studies particles that are atomic in size, while physics is well aware that the fundamental objects are at least 10 orders of magnitude smaller than that, with sizes comparable to quarks and leptons, at which they are at least as small. On the other hand, nanoscience may provide crucial insights into emergence, the idea that a complex whole might evolve from a sufficient number of simple interactions ("more is different"). Computer simulations have directly demonstrated this idea. Nanoscience may therefore provide crucial insights into an emerging worldview! With time, it became clear that nanosized structures not only have numerous applications in physics and quantum mechanics, but are also crucial in engineering, chemistry, biological sciences, and medicine, opening the door to wonderful innovations through interdisciplinary collaboration between those fields.



## 1.4 History and development in Nanoscience and Technology

Although nanotechnology is a relatively recent field of study, research on the nanometer scale is not. The nanometer regime has long been used in the study of biological systems and the engineering of numerous materials, including colloidal dispersions, metallic quantum dots, and catalysts. Historical data demonstrates that nanotechnology has existed in some form or another since the dawn of human civilization. Early examples of nanostructured materials were based on the material manipulation and empirical understanding of craftspeople. Due to inventions and tremendous development of spectroscopic and characterization tools, such as Transmission Electron Microscopy, Field Emission Scanning Electron Microscopy, and so on and so forth, the most significant scientific breakthroughs with vivid application and implications in nanotechnology emerge in the modern era.

**4th century:** Glass colored by Ag and Au nanoparticles (Lycurgus cup, British Museum).

**9th to 17th century:** Glowing, glittering "lustre" glazes.

**About 2000 years ago:** In ancient Egypt, common men use nanoparticles called galenite (lead sulfide), a dying paste to their hair black, a few nanometers in size. They were able to make this by reacting lime, lead oxide and small amount of water.

**More than 1000 years ago:** Chinese are known to use Au nanoparticles as an inorganic dye to introduce red color into their ceramic porcelains.

**19th century:** Photography using Ag nanoparticles.

**1857:** Colloidal dispersion of gold (Au) prepared by Michael Faraday.

**1931:** The first Transmission Electron Microscope was built by Max Knoll and Ernst Ruska in 1931, with this group developing the first TEM with resolution greater than that of light in 1933 and the first commercial TEM in 1939. In 1986, Ruska was awarded the Nobel Prize in physics for the development of Transmission Electron Microscopy.

**1936:** Erwin Muller invented the field emission Microscope.

**1950:** Victor La Mer and Robert Dinegar developed the theory and a process for growing monodisperse Colloids.

**1956:** Arthur von Hippel introduced "molecular engineering".

**1958:** Jack Kilby built the first integrated circuit.

**1959:** Richard Feynman projected engineering at the atomic scale.

**1965:** Moore's Law.

**1972:** Field Emission Scanning Electron Microscope was invented by Albert with the help of Hitachi

**1974:** Professor Norio Taniguchi at the University of Tokyo first invented the term "nanotechnology".

**1981:** Gerd Binnig and Heinrich Rohrer invented the Scanning Tunneling Microscope. They awarded Nobel Prize in physics in 1986.

**1985:** Discovery of Buckminsterfullerene (C<sub>60</sub>) at Rice University by Richard Smalley, Robert Curl, James Heath, Sean O'Brien, and Harold Kroto.

**1986:** Gerd Binnig, Calvin Quate, and Christoph Gerber invented the atomic force Microscope.

**1991:** Carbon nanotube was discovered by Prof. Sumio Iijima.

**1992:** C.T. Kresge and colleagues discovered the nanostructured MCM-41 and MCM-48.

**1993:** Invention of controlled synthesis of nanocrystals.

**1998:** Dr. Nadrian, C. Seeman and his co-workers at New York University announced in January a major advance along one potential path toward molecular nanotechnology that involves making devices from branched DNA molecules.

**1999:** Dip pin nano lithography was invented by the Mirkin Group.

**2003:** 21st century Nanotechnology Research Report.

**2005:** DNA based computer and "algorithmic self-assembly".

**2007:** Lithium-ion battery with a common type of virus.

**2009:** Several DNA-like robotic Nanoscale assembly devices.

**2010:** Graphene, two dimensional, one of the allotropes of carbon was discovered in 2004 by Ande Geim and Konstantin Novoselov at the University of Manchester and they were awarded Nobel Prize in physics in 2010.

**2014:** The NNI release the updated 2014 Strategic plan.

## 1.5 Classification of nanomaterials

Due to the discovery of innovative synthesis pathways, characterization techniques, and manipulation tools, nanoscience and nanotechnology have grown rapidly during the last few decades. Nanoscale structures come in a variety of forms, including thin films, nanowires, and nanoparticles, among others. The term "quantum dot" is frequently used to refer to nanoparticles, which are essentially zero-dimensional systems. Theoretical study has provided a comprehensive explanation for the new properties of the aforementioned systems, which are nothing more than applications of Basic Physics. It is crucial to briefly describe the density of states (DOS) of quantum dots (0 dimension), quantum wires (1 dimension), and quantum wells (2 dimensions) in order to comprehend these systems.

In solid-state and condensed matter physics, the density of states (DOS) of a system refers to the number of states per interval of energy at each energy level that are available to be occupied. The dimensional boundaries of the thing itself determine the DOS.

The units of DOS show the role dimensions play ( $\text{Energy}^{-1} \text{Volume}^{-1}$ ). A volume becomes an area in the limit that the system has two dimensions and a length in the limit that the system has one dimension. It is crucial to remember that the volume being discussed is the volume of  $k$  space, or the area bounded by the system's constant energy surface, which is obtained via a dispersion relation that connects  $E$  and  $k$ . The electronic band structure determines the dispersion relation for electrons within a material.

The available electron states in a system can be calculated by the well known Schrodinger's equation:

$$H\Psi = E\Psi.$$

The general expression to obtain the density of states in k-space/volume is as follows:

$$N(E)dE \propto E^{\frac{d}{2}-1}dE \quad d = 1,2,3$$

The energy is calculated from the top of the valence band for holes and the bottom of the conduction band for electrons in this case, where  $d$  is the degree of dimension.  $N(E)$  is a smooth square-root energy function in the three-dimensional (3-D) system. Since  $N(E)$  in a 2-D system is constant, it differs significantly from a 3-D system. Although the density of states is a step function in a 2-D system, the energy spectrum is quasi-continuous [11]. The dependence of DOS on energy changes by  $E^{-1/2}$  each time we transition to a lower dimensionality system.

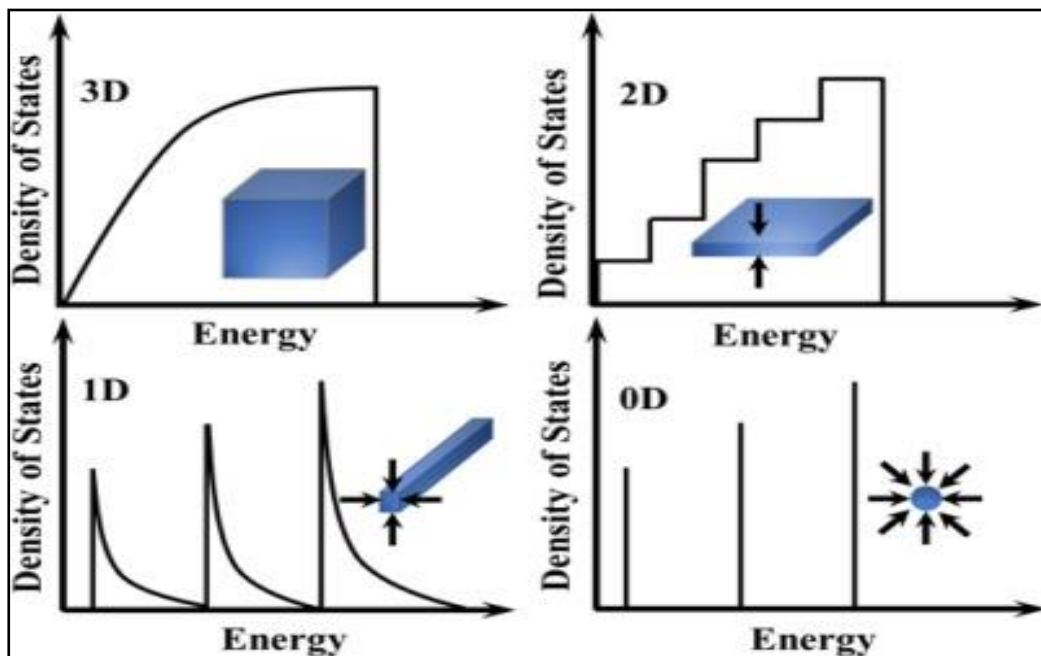


**Fig 1.1** Schematic illustration of structural dimensionality of materials with density of states [12]

Now a quick discussion of the "quantum size effect" is necessary. To achieve this, materials' electrical characteristics are altered while their particle sizes are noticeably reduced. If the reduction in dimension is restricted from macro to micro, this effect has no bearing. On the other hand, the quantum effect becomes quite noticeable at the nanoscale. The electrical structure of nanocrystals is altered by the quantum confinement effect when the diameters of the nanoparticles are equivalent to the Bohr excitonic radius ( $r_B$ ) of those materials. Strong

quantum confinement effects occur if the particle radius ( $r$ ) in the nanocrystalline materials is less than the Bohr radius ( $r_B$ ). The presence of weak quantum confinement effects is observed in particles with radii greater than the Bohr radius ( $r > r_B$ ).

When compared to a macroscopic system, a number of physical characteristics, including electrical, optical, and mechanical ones, alter in the nanoscale dimension. For instance, the thermal, mechanical, and catalytic properties of materials are altered by an increase in the surface to volume ratio. The rate of reaction diffusion for nanostructured materials and the characteristics of charge transport in nanodevices both accelerate.

### **1.5.1 Zero dimensional materials (0-D)**

Materials having zero dimensions, or 0-D, are those larger than 100 nm in which all dimensions are measured at the nanoscale. Nanoparticles are the most typical form of zero-dimensional nanomaterials. Nanoparticles come in a variety of shapes and sizes, can exist alone or as part of a matrix, and can be made of metallic, ceramic, or polymeric materials. They can also be amorphous, crystalline, single-crystalline, or polycrystalline, and can be made of one or more chemical elements. An electron is constrained in 3-D space for 0-D nanomaterials, where all dimensions are nanoscale. There is no movement or delocalization of the electrons.

### **1.5.2 One dimensional material (1-D)**

This results in nanomaterials with a form resembling a needle in the one dimension outside the nanoscale. Nanotubes, nanorods, and nanowires are examples of 1-D materials. 1-D nanomaterials can be metallic, ceramic, polymeric, single-crystalline or polycrystalline, chemically pure or impure, amorphous or crystalline, single-crystalline or polycrystalline, standalone materials or embedded in another medium. In 1-D nanomaterials, electron confinement takes place in 2-D, whereas delocalization happens along the nanomaterial's long axis of the nanowire/rod/tube.

### **1.5.3 Two dimensional materials (2-D)**

Materials that are not restricted to the nanoscale in any dimension are referred to as bulk nanomaterials. These materials can be identified by their three arbitrary dimensions that are above 100 nm. Materials either have a nanocrystalline structure or contain nanoscale characteristics. Bulk nanomaterials can be made up of various arrangements of nano-sized crystals, usually in various orientations, according to nanocrystalline structures. Regarding the presence of nanoscale characteristics, 3-D nanomaterials can include multilayers, bundles of nanowires and nanotubes, and dispersions of nanoparticles. The electrons are totally delocalized for 3-D nanomaterials.

## **1.6 Optical and Electrical properties of nanomaterials**

### **1.6.1 Transmittance and Absorption**

Any material's transmission and absorption are influenced by the particle size. Nanoscale materials display unique characteristics. Controlling the external parameters will affect these qualities. Quantum confinement of the carriers may result from a change in particle size, and it may get worse as dimensions get smaller [13]. Dopant inclusion, which modifies the band gaps, may also control it. The change in lattice characteristics caused by annealing [14, 15] or impurity doping [16, 17] is typically the cause of band gap variation.

### **1.6.2 Electrical conductivity**

Charge transfer phenomenon for materials of nanoscale dimension mostly depends on the grain boundary [18]. Since the grain boundary's interface has a high density of defects like vacancies, dangling bonds, vacancy clusters, etc., it has a substantial impact [19]. As a result, in the presence of an external field, charge transport at grain boundary interfaces may take place via dipole reorientation, electronic relaxation polarisation, and space charge distribution. The grain boundary flaws have a significant influence in changing the material's dielectric properties when heated externally.

## 1.7 Why 2-D materials?

The study of materials with at least one dimension in the nanometer range is the focus of the discipline of material science known as nanomaterials [20]. At this scale, the number of atoms or molecules that make up the material is related to qualitative changes in its physicochemical qualities and reactivity. For instance, size-effect qualities can be seen in semiconductor particles' quantum confinement, metal nanoparticles' surface plasmon resonance, and magnetic nanomaterials' superparamagnetism.

If just one dimension is constrained, the material will be layered or 2D; if both dimensions are constrained, the material will be wired or 1D; and if all dimensions are constrained to a few nanometers or less, the material is typically referred to as 0D.

Therefore, one of the most important factors in establishing a material's attributes is its dimensionality, not just its size. This is especially true for  $sp^2$  carbon materials (**Fig. 1.2**), where highly diverse characteristics are displayed by 0D fullerenes, 1D nanotube, 2D graphene, and 3D graphite. Additionally, the case of carbon serves as a good illustration when examining the chronological order of the discoveries of the various dimensional forms of a certain material: Since the sixteenth century, graphite has been used extensively in industry to make steel, as brake linings, and as a dry lubricant in various other devices. But it wasn't until 1985 that fullerenes [21] were discovered, substantially increasing the number of carbon allotropes that were previously known and also raising the possibility that its 1D form, carbon nanotubes, which were first observed in 1991 [22], might exist.

Although single layers of graphite were used as starting materials for theoretical investigations of graphite, fullerenes, and nanotubes, it wasn't until 2004 [23] that researchers were able to isolate a monolayer graphene sheet for the first time. The recent rise of graphene literature demonstrates both the fundamental scientific interest in this material as well as its potential technological significance. In fact, it is anticipated that two-dimensional materials will significantly influence a wide range of applications, including electronics, gas storage or separation, catalysis, high-performance sensors, support membranes, and inert coatings, to name a few.

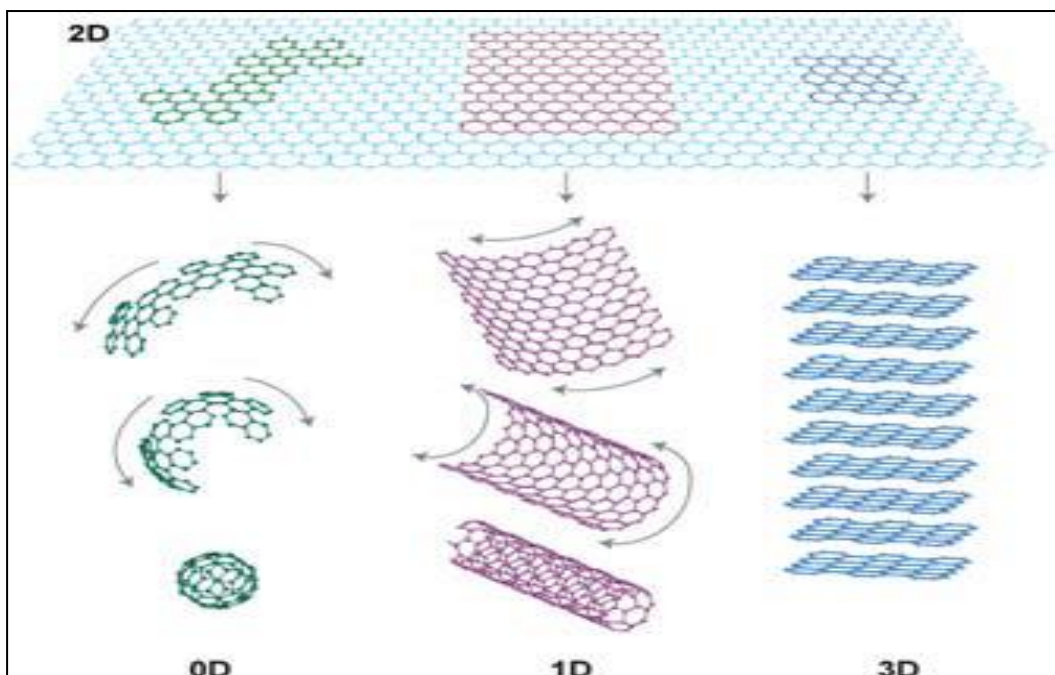


**Fig 1.2** Graphene can be envisaged as a 2D material for carbon materials among all other dimensionalities. It can be wrapped up into 0D bucky-balls, rolled into 1D nanotube or stacked into 3D graphite [24].

The production and physical characteristics of graphene have been covered in a huge number of articles and reviews. These findings have prompted the development of numerous novel 2D materials, but the body of literature on the subject is still small and dispersed. This review first seeks to highlight how the extensive literature on concepts and methods already known for the isolation and characterization of graphene can be applied to a whole new family of 2D materials in order to have a unified viewpoint of the subject. Second, fresh viewpoints and prospective uses for these 2D materials are offered.

Size restrictions in one or more dimensions actually alter some material qualities. Therefore, 2D materials generally have some different properties from their bulk form. Due to the confinement of electrons as well as the absence of interlayer interactions, which, despite being often relatively weak, are crucial in determining band structure, optical and electrical properties are typically distinct from one another. Other changes in characteristics, such those in mechanical and chemical reactivity, are mostly brought on by geometry effects and the high surface-to-bulk ratio (which can even be infinite in the thinnest materials).



## 1.8 Introduction of MoS<sub>2</sub>

Since it was originally physically exfoliated from three-dimensional (3D) graphite in 2004 [25], graphene, a typical two-dimensional (2D) layered material, has reached its golden age. Monolayer graphene has been found to have a number of strikingly highlighted properties, including high specific surface area (2630 m<sup>2</sup>/g), high Young's modulus (1.1 TPa), high thermal conductivity at room temperature (3x10<sup>3</sup> W/m K), high electrical conductivity (~10<sup>4</sup> Ω<sup>-1</sup> cm<sup>-1</sup>), and high transparency (97.7 percent transmittance in the visible spectrum) [26, 27]. The use of graphene in a variety of applications, such as transparent electrodes [28], energy storage [29], solar cells [30, 31], wearable technology, and catalysis [32], is made possible by all these exceptional features.

Because of its unique  $\pi$ - $\pi^*$  band structure, graphene is classified as a semi-metallic substance. Since the valence and conduction bands are symmetrical about the Dirac point, the Dirac equation—rather than the Schrodinger equation—can be used to describe the electrical properties of the material close to the K point. Graphene is a zero-gap material because the Fermi surface is simply where the valence and conduction bands intersect [25]. The exceptional electrical properties of graphene are due to its special structure, which also places restrictions on its use in logical circuits for low-power electronic switching.

In order to overcome the scarcity of graphene and increase the scope of its applications, research has recently shifted its attention to alternative 2D materials that resemble graphene [33, 34]. Similar characteristics exist in 3D bulk materials and their analogous 2D layered materials [35]. These materials should be surface stable at ambient temperature and chemically inert despite having melting points more than 1000 °C. Because most metallic materials are chemically active by nature, 2D insulating and semiconducting materials are generally easier to obtain. In this contest, which initially includes many lubricants, graphite, hBN and molybdenum disulfide (MoS<sub>2</sub>) stand out. hBN serves as a gate dielectric in capacitors and is a common electrical insulator [36]. One of the most investigated layered transition metal dichalcogenides (TMDCs) is MoS<sub>2</sub>, which has been widely found in nature as molybdenite. A semiconductor called monolayer MoS<sub>2</sub> has a direct bandgap of 1.8 eV [34]. Inspiringly, this ability of MoS<sub>2</sub> will largely make up for gapless graphene's weakness, enabling the adoption of 2D materials in the next generation of switching and optoelectronic devices. MoS<sub>2</sub> has so far made significant advancements in the following areas: energy conversion [37], energy storage [38], and hydrogen evolution reaction (HER) [39].

Furthermore, MoS<sub>2</sub> with an odd number of layers was capable of generating oscillating piezoelectric voltage and current outputs, indicating its potential use in supplying power to stretchable electronics and nanodevices [40].

TMDCs, which have a vast family of materials with the generalised formula MX<sub>2</sub> (M = Transition metal (Ti, Zr, Hf, V, Nb, Ta, Mo, W, Tc, Re, Co, Rh, Ir, Ni, Pd, Pt), X = Chalcogen (S, Se, Te)), can have semiconducting, metallic, or superconducting electronic characteristics [36]. Mo (+4) and S (-2) are structured to a sandwich structure in a single layer of MoS<sub>2</sub> films by covalent bonds in a sequence of S-Mo-S [41], with the sandwich layers being contacted by relatively weak van der Waals forces. Each layer typically has a thickness of ~0.65 nm. It has been discovered that monolayer MoS<sub>2</sub> with trigonal prismatic polytype is semiconducting (2H), but monolayer MoS<sub>2</sub> with octahedral crystal symmetry configuration is metallic (1T) [42]. MoS<sub>2</sub> has a mechanically flexible Young's modulus of 0.33±0.07 TPa, which is quite similar to that of graphene [43].

### 1.8.1 Crystal structures of MoS<sub>2</sub>

The single layer of MoS<sub>2</sub> has the Lamellar S-Mo-S structure, as depicted in **Fig. 1.3**, and has a thickness of around ~0.7 nm [45]. Each MoS<sub>2</sub> 2D crystal layer is made up of two S atoms in a trigonal prismatic shape and two S atoms in a hexagonal plane that are both modified by covalent interactions. Weak van der Waals forces connect adjacent atomic sandwich units. The distance between the upper and lower sulphur atoms, the crystal lattice constant, and the Mo-S length are each 2.4, 3.2, and 3.1 Å, respectively [46, 47]. The two primary phase types in MoS<sub>2</sub> are 2H and 3R phases. The former has two layers per unit cell stack in a trigonal prismatic coordination hexagonal symmetry, whereas the later has three layers per unit cell stack in a trigonal prismatic coordination rhombohedral symmetry [48]. In comparison to the 3R phase, the 2H phase is more stable and dominates in nature. The 1T metallic phase, in which Mo atoms are coupled in an octahedral way, was also identified by Frindt and coworkers [44]. Single-layer MoS<sub>2</sub> generated by exfoliating lithium-intercalated MoS<sub>2</sub> powder was evaluated for its detailed structural details using X-ray diffraction. Unique electrical characteristics exist in the metallic phase [49–52]. The 1T phase, which is a metastable structure, can change into the 2H phase through heating or ageing.

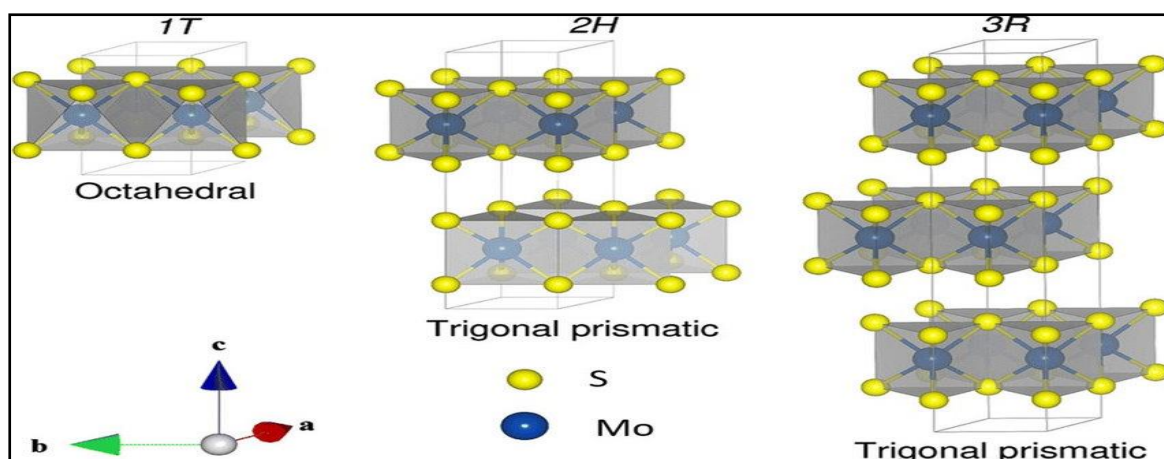


**Fig. 1.3** Crystal structure of MoS<sub>2</sub>: Octahedral (1T), Trigonal prismatic (2H) and Trigonal prismatic (3R) unit cell structures [53].

### 1.8.2 Different synthesis methods of MoS<sub>2</sub>

A top-down method, such as mechanical exfoliation [54, 55] and chemical exfoliation [56–58], and a bottom-up approach, such as chemical vapour deposition on substrates [58, 59] and chemical synthesis [60–62], were both used in the synthesis process. MoS<sub>2</sub> has been created using a variety of techniques as a co-catalyst:

- *Impregnation method* is widely used for the dispersion of nanoparticulate MoS<sub>2</sub> (2H) on photosensitizer (e.g., CdS, TiO<sub>2</sub>) for both powdered photocatalysis and PEC processes. For example, MoS<sub>2</sub> on CdS can be prepared by impregnating CdS with an aqueous solution of (NH<sub>4</sub>)<sub>2</sub>MoS<sub>4</sub>, followed by treatment in H<sub>2</sub>S flow at high temperature [63].
- *Hydrothermal method* could use low toxic thiourea as a sulfur source to react with molybdenum salt (such as Na<sub>2</sub>MoO<sub>4</sub>), together with semiconductor powders [64].
- *Ball-milling method* was employed to mix (NH<sub>4</sub>)<sub>2</sub>MoS<sub>4</sub> and semiconductor powder in the presence of ethanol, followed by high temperature calcination in inert atmosphere [65].
- *Photodeposition approach* could be used to decorate MoS<sub>2</sub> nanocrystals on TiO<sub>2</sub> under UV irradiation with (NH<sub>4</sub>)<sub>2</sub>MoS<sub>4</sub> as precursor in ethanol/water solution [66].
- *Anion exchange reaction* was applied to synthesize MoS<sub>2</sub> nanotube photoelectrode from Mo<sub>3</sub>O<sub>10</sub>(C<sub>2</sub>H<sub>10</sub>N<sub>2</sub>) nanowires and L-cysteine by heating at 200°C for 14 h [67].
- *Chemical exfoliation process* was usually exploited to prepare 1T metallic MoS<sub>2</sub> catalysts by ion intercalation [68].

## 1.9 Objectives of the work

- Following are the main objectives of this thesis:
  1. To synthesize 2H-MoS<sub>2</sub> nanosheets and separate the layers of 2H-MoS<sub>2</sub> without metal intercalation.
  2. Doping Zinc in MoS<sub>2</sub> by simple Hydrothermal route and study its electrochemical property.
  
- The specific objective of this work is as follows:
  1. To study various structural, optical, morphological and surface analysis of the prepared samples.
  2. To study HER and ORR kinetics of different Zn doped MoS<sub>2</sub>.

Characterization of the as-synthesized materials with some sophisticated tools like X-Ray Diffractometer (XRD), Field Emission Scanning Electron Microscope (FESEM), X-Ray Photoelectron Spectroscopy (XPS), UV-Vis Spectrophotometer, etc. is another objective of this thesis.

## References:

1. Newton, Marshall D., et al. "Electron transfer in chemistry ." (2001).
2. ArnulfJager-Waldau, Solar Energy Materials and Solar Cells, Volume 95, Issue 6, June 2011, Pages 1509-1517
3. K. Aryal, B. N. Pantha, J. Li, J. Y. Lin, and H. X. Jiang, Applied Physics Letters 96, 052110 (2010)
4. Ludmila P. Oleksenko, Nelly P. Maksymovych, Evgeniy V. Sokovykh, Igor P. Matushko, Andrii I. Buvailo, Norman Dollahon, Sensors and Actuators B 196 (2014) 298-305
5. A. Ohtomo, M. Kawasaki, T. Koida, K. Masubuchi, H. Koinuma, Y. Sakurai, Y. Yoshida, T. Yasuda, and Y. Segawa, Applied Physics Letters 72, 2466 (1998)
6. Ryu Abe, Kazuhiro Sayama, and Hideki Sugihara, J. Phys. Chem. B 2005, 109, 16052-16061
7. Nanostructures and Nanomaterials: Synthesis, Properties and Applications; Guozhong Cao.
8. [https://www.nano.gov/nanotech-101/what/ definition](https://www.nano.gov/nanotech-101/what/definition).
9. Journal of Faculty of Engineering & Technology, 2007, 2008, pages, 1120.
10. Introduction to Nanoscience, Kai Nordlund 2005.
11. P. Motiarty, Rep. Prog. Phys. 64 (2001) 297.
12. Sinha, Tridib Kumar. "Morphology-dependent visible light photocatalysis." *Nanostructured Materials for Visible Light Photocatalysis*. Elsevier, 2022. 375-412.
13. Kuo-Feng Lin, Hsin-Ming Cheng, Hsu-Cheng Hsu, Li-Jiaun Lin, Wen-Feng Hsieh, Chemical Physics Letters 409 (2005) 208-211
14. O. Vigil, F. Cruz, A. Morales-Acevedob, G. Contreras-Puente, Materials Chemistry and Physics 68 (2001) 249-252
15. G. Anil Kumar, M. V. Ramana Reddy, KattaNarasimha Reddy, Journal of Physics: Conference Series 365 (2012) 012031
16. H. Merzouk, A. Chelouche, S. Saoudi, D. Djouadi, A. Aksas, ApplPhys A (2012) 109: 841-844
17. B. SrinivasaRao, V. Rajagopal Reddy, B. Rajesh Kumar, T. SubbaRao, International Journal of Nanoscience, Vol. 11, No. 3 (2012) 1240006(5pages)
18. SoumenDhara, P. K Giri, Journal of Experimental Nanoscience, 8(2013) 3, 332-340

19. C. Suryanarayana, Bull. Mater. Sci., 17 (1994) 307
20. G. A. Ozin and A. C. Arsenault, Nanochemistry, RSC Publishing, Cambridge, UK, 2005.
21. H. W. Kroto, J. R. Heath, S. C. O'Brien, R. F. Curl and R. E. Smalley, Nature, 1985, 318, 162–163.
22. S. Iijima, Nature, 1991, 354, 56–58.
23. K. S. Novoselov, A. K. Geim, S. V. Morozov, D. Jiang, Y. Zhang, S. V. Dubonos, I. V. Grigorieva and A. A. Firsov, Science, 2004, 306, 666–669.
24. Gomez-Navarro, M. B. C., J. Gomez-Herrero, and F. Zamora. "2D materials: To graphene and beyond." *Nanoscale* 3.1 (2011): 20.
25. Novoselov KS, Geim AK, Morozov SV, Jiang D, Zhang Y, Dubonos SV, et al. Electric field effect in atomically thin carbon films. Science 2004;306:666e9.
26. Allen MJ, Tung VC, Kaner RB. Honeycomb carbon: a review of graphene. Chem Rev 2010;110:132e45.
27. Soldano C, Mahmood A, Dujardin E. Production, properties and potential of graphene. Carbon 2010;48:2127e50.
28. Bae S, Kim H, Lee Y, Xu X, Park JS, Zhang Y, et al. Roll-to-roll production of 30-inch graphene films for transparent electrodes. Nat Nanotechnol 2010;5:574e8.
29. Zang X, Chen Q, Li P, He Y, Li X, Zhu M, et al. Highly flexible and adaptable, all-solid-state supercapacitors based on graphene woven fabric film electrodes. Small 2014;10:2583e8.
30. Li X, Zang X, Li X, Zhu M, Chen Q, Wang K, et al. Hybrid heterojunction and solid-state photoelectrochemical solar cells. Adv Energy Mater 2014;4:1400224.
31. Li X, Xie D, Park H, Zeng Helen T, Wang K, Wei J, et al. Anomalous behaviors of graphene transparent conductors in graphene-silicon heterojunction solar cells. Adv Energy Mater 2014;3:1029e34.
32. Wang Y, Wang L, Yang T, Li X, Zang X, Zhu M, et al. Wearable and highly sensitive graphene strain sensors for human motion monitoring. Adv Funct Mater 2014;24:4666e70.
33. Ganatra R, Zhang Q. Few-layer MoS<sub>2</sub>: a promising layered semiconductor. ACS Nano 2014;8:4074e99.
34. Chhowalla M, Shin HS, Eda G, Li LJ, Loh KP, Zhang H. The chemistry of two-dimensional layered transition metal dichalcogenide nanosheets. Nat Chem 2014;5:263e75.

35. Geim AK, Grigorieva IV. van der Waals heterostructures. *Nature* 2013;499:419e25.
36. Yu GL, Jalil R, Belle B, Mayorov AS, Blake P, Schedin F, et al. Interaction phenomena in graphene seen through quantum capacitance. *PNAS* 2013;110:3282e6.
37. Wi S, Kim H, Chen M, Nam H, Guo LJ, Meyhofer E, et al. Enhancement of photovoltaic response in multilayer MoS<sub>2</sub> induced by plasma doping. *ACS Nano* 2014;8:5270e81.
38. Ding S, Zhang D, Chen JS, Lou XW. Facile synthesis of hierarchical MoS<sub>2</sub> microspheres composed of few-layered nanosheets and their lithium storage properties. *Nanoscale* 2012;4:95e8.
39. Li Y, Wang H, Xie L, Liang Y, Hong G, Dai H. MoS<sub>2</sub> nanoparticles grown on graphene: an advanced catalyst for the hydrogen evolution reaction. *J Am Chem Soc* 2011;133:7296e9.
40. Wu W, Wang L, Li Y, Zhang F, Lin L, Niu S, et al. Piezoelectricity of single-atomic-layer MoS<sub>2</sub> for energy conversion and piezotronics. *Nature* 2014;514:470e4.
41. Jariwala D, Sangwan VK, Lauhon LJ, Marks TJ, Hersam MC. Emerging device applications for semiconducting two-dimensional transition metal dichalcogenides. *ACS Nano* 2014;8:1102e20.
42. Eda G, Yamaguchi H, Voiry D, Fujita T, Chen M, Chhowalla M. Photoluminescence from chemically exfoliated MoS<sub>2</sub>. *Nano Lett* 2011;11:5111e6.
43. Akinwande D, Petrone N, Hone J. Two-dimensional flexible nanoelectronics. *Nat Commun* 2014;5(5678):1e12.
44. Yang, D., S. J. Sandoval, W. M. R. Divigalpitiya, J. C. Irwin, and R. F. Frindt. 1991. Structure of single-molecular-layer MoS<sub>2</sub>. *Phys. Rev. B* 43:12053–12056.
45. Late, D. J., B. Liu, H. S. S. R. Matte, V. P. Dravid, and C. N. R. Rao. 2012. Hysteresis in single-layer MoS<sub>2</sub> field effect transistors. *ACS Nano* 6:5635–5641.
46. Ataca, C., M. Topsakal, E. Aktürk, and S. Ciraci. 2011. A comparative study of lattice dynamics of three-and two-dimensional MoS<sub>2</sub>. *J. Phys. Chem. C* 115:16354–16361.
47. Ataca, C., H. Sahin, and S. Ciraci. 2012. Stable, single-layer MX<sub>2</sub> transition-metal oxides and dichalcogenides in a honeycomb-like structure. *J. Phys. Chem. C* 116:8983–8999.
48. Beal, A. R., J. C. Knights, and W. Y. Liang. 1972. Transmission spectra of some transition metal dichalcogenides. II. Group via: trigonal prismatic coordination. *J. Phys. C: Solid State Phys.* 5:3540.

49. Shirodkar, S. N., and U. V. Waghmare. 2014. Emergence of ferroelectricity at a metal-semiconductor transition in a 1T monolayer of MoS<sub>2</sub>. *Phys. Rev. Lett.* 112:157601.
50. Acerce, M., D. Voiry, and M. Chhowalla. 2015. Metallic 1t phase MoS<sub>2</sub> nanosheets as supercapacitor electrode materials. *Nat. Nanotechnol.* 10:313–318.
51. Cheng, P., K. Sun, and Y. H. Hu. 2016. Memristive behavior and ideal memristor of 1T phase MoS<sub>2</sub> nanosheets. *Nano Lett.* 16:572–576.
52. Cheng, P., K. Sun, and Y. H. Hu. 2016. Mechanically-induced reverse phase transformation of MoS<sub>2</sub> from stable 2H to metastable 1T and its memristive behavior. *RSC Adv.* 6:65691–65697.
53. Kuc, A. 2015. Low-dimensional transition-metal dichalcogenides. Pp. 1–29 *in* M. Springborg, and J. Joswig, ed. *Chemical modelling: volume 11*. The Royal Society of Chemistry, London, UK.
54. Novoselov, K. S., D. Jiang, F. Schedin, T. J. Booth, V. V. Khotkevich, S. V. Morozov, et al. 2005. Two-dimensional atomic crystals. *Proc. Natl Acad. Sci. USA* 102:10451–10453.
55. Li, H., Z. Yin, Q. He, H. Li, X. Huang, G. Lu, et al. 2012. Fabrication of single-and multilayer MoS<sub>2</sub> film-based field-effect transistors for sensing no at room temperature. *Small* 8:63–67.
56. Coleman, J. N., et al. 2011. Two-dimensional nanosheets produced by liquid exfoliation of layered materials. *Science* 331:568–571.
57. Zhou, K.-G., N.-N. Mao, H.-X. Wang, Y. Peng, and H.-L. Zhang. 2011. A mixed-solvent strategy for efficient exfoliation of inorganic graphene analogues. *Angew. Chem. Int. Ed.* 50:10839–10842.
58. Wang, X., H. Feng, Y. Wu, and L. Jiao. 2013. Controlled synthesis of highly crystalline MoS<sub>2</sub> flakes by chemical vapor deposition. *J. Am. Chem. Soc.* 135:5304–5307.
59. Huang, X., Z. Zeng, and H. Zhang. 2013. Metal dichalcogenide nanosheets: preparation, properties and applications. *Chem. Soc. Rev.* 42:1934–1946.
60. Ramakrishna Matte, H. S. S., A. Gomathi, A. K. Manna, D. J. Late, R. Datta, S. K. Pati, et al. 2010. MoS<sub>2</sub> and WS<sub>2</sub> analogues of graphene. *Angew. Chem. Int. Ed.* 49:4059–4062.



61. Altavilla, C., M. Sarno, and P. Ciambelli. 2011. A novel wet chemistry approach for the synthesis of hybrid 2D free-floating single or multilayer nanosheets of MS<sub>2</sub>@Oleylamine (M=Mo, W). *Chem. Mater.* 23:3879–3885.
62. Peng, Y., Z. Meng, C. Zhong, J. Lu, W. Yu, Y. Jia, et al. 2001. Hydrothermal synthesis and characterization of single-molecular-layer MoS<sub>2</sub> and MoSe<sub>2</sub>. *Chem. Lett.* 30:772–773.
63. Zong, X., H. Yan, G. Wu, G. Ma, F. Wen, L. Wang, et al. 2008. Enhancement of photocatalytic H<sub>2</sub> evolution on CdS by loading MoS<sub>2</sub> as cocatalyst under visible light irradiation. *J. Am. Chem. Soc.* 130:7176–7177.
64. Liu, Y., H. Yu, X. Quan, and S. Chen. 2013. Green synthesis of feather-shaped MoS<sub>2</sub>/CdS photocatalyst for effective hydrogen production. *Int. J. Photoenergy* 2013, 247516–247521.
65. Chen, G., D. Li, F. Li, Y. Fan, H. Zhao, Y. Luo, et al. 2012. Ball-milling combined calcination synthesis of MoS<sub>2</sub>/CdS photocatalysts for high photocatalytic H<sub>2</sub> evolution activity under visible light irradiation. *Appl. Catal. A* 443–444:138–144.
66. Kanda, S., T. Akita, M. Fujishima, and H. Tada. 2011. Facile synthesis and catalytic activity of MoS<sub>2</sub>/TiO<sub>2</sub> by a photodeposition-based technique and its oxidized derivative MoO<sub>3</sub>/TiO<sub>2</sub> with a unique photochromism. *J. Colloid Interface Sci.* 354:607–610.
67. Zhuo, S., Y. Xu, W. Zhao, J. Zhang, and B. Zhang. 2013. Hierarchical nanosheet-based MoS<sub>2</sub> nanotubes fabricated by an anion-exchange reaction of MoO<sub>3</sub>– amine hybrid nanowires. *Angew. Chem. Int. Ed.* 52:8602–8606.
68. Maitra, U., U. Gupta, M. De, R. Datta, A. Govindaraj, and C. N. R. Rao. 2013. Highly effective visible-light- induced H<sub>2</sub> generation by single-layer 1t-MoS<sub>2</sub> and a nanocomposite of few-layer 2H-MoS<sub>2</sub> with heavily nitrogenated graphene. *Angew. Chem. Int. Ed.* 52:13057–13061.

**CHAPTER 2**  
**INTRODUCTION TO**  
**HER AND ORR**

## 2.1 Introduction to Hydrogen Evolution Reaction (HER)

The world has been paying close attention to environmental pollution, global warming, and the energy problem brought on by huge fossil fuel burning [1]. To address environmental and energy concerns, it is essential to develop sustainable and renewable energy sources as well as effective energy storage and conversion technologies. One of the most promising strategies is the integration of grid scale renewable energy gathering technology with electrochemical water splitting. In addition, hydrogen is thought to be the best clean energy transporter because it has the highest mass-energy density of any fuel.

The discovery of low-cost, highly active, and long-lasting catalysts for oxygen evolution reactions (OERs) and hydrogen evolution reactions (HERs) is crucial for the practical realisation of water splitting. The extraordinary electrocatalytic performance of heterostructured catalysts, which are typically made up of electrochemically active materials and various functional additives, has recently been demonstrated toward HER and OER. In particular, a number of precious-metal free heterostructures delivered comparable activity with precious-metal based catalysts.

In a conventional water electrolysis system, the HER and OER at the cathode and anode, respectively, create  $\text{H}_2$  and  $\text{O}_2$ , and an external current is used to go above the reaction's energy barrier ( $237 \text{ kJ mol}^{-1}$ ). Pt is the most advanced catalyst for HER at this time, while noble-metal based catalysts continue to be the most effective catalysts for HER and OER [2-5]. Therefore, one of the main priorities for the development of affordable and effective water electrolysis systems is the creation of high activity, earth-abundant catalysts.

Numerous earth-abundant catalysts have been identified to date [6–13] with significant catalytic activity toward OER and in particular HER. Transition metal dichalcogenides (TMDs), transition metal phosphides (TMPs), carbides, [24–26] and nitrides, [27, 28] are the subject of substantial research with relation to HER. Recently, a range of heterostructured catalysts have distinguished themselves from the competition by outperforming their equivalents in terms of catalytic performance for electrochemical water splitting [29–33].

## 2.2 Mechanisms of Electrochemical HER

Redox reactions happen at the electrode/electrolyte interface during electrocatalytic HER, which is essentially an electrochemical process. H<sub>2</sub> is produced either through the reduction of proton (H<sup>+</sup>) or H<sub>2</sub>O, both of which involve a number of fundamental processes, depending on the electrolyte's pH level.

### 2.2.1 HER in Acidic Media

It is widely acknowledged that the HER occurs in two phases in acidic environments at the surface of different catalysts[34-36]. A H<sup>+</sup> forms an adsorbed hydrogen atom (H\*) at the start of the hydrogen evolution reaction (HER), where \* denotes an active site on the catalyst surface. Equation (1) refers to this procedure as the **Volmer step** or discharge step.

The **Heyrovsky step**, also known as the electrochemical desorption step, is when a H\* joins forces with an H<sup>+</sup>, an electron (e), and an H<sub>2</sub> molecule, as shown in Equation (2). A different method of producing H<sub>2</sub> is through the Tafel step, also known as the chemical desorption step, which involves combining two H\* on the catalyst surface (Equation 3). Equation (4), which uses the standard electrode potential (E°) as a point of comparison when assessing the standard electrode potential of electrochemical processes, represents the total reaction of HER [37]. The interaction between the catalyst and H\*[39] is crucial for the HER kinetics, according to the Sabatier principle [38].

- *Acidic media:*



### 2.2.2 HER in Alkaline Media

Regarding the HER in alkaline media, it has been found that these exchange current densities are often two to three orders of magnitude lower in alkaline solutions than in acidic electrolytes [40, 41]. The fact that the alkaline HER follows a different pathway from that in acidic solutions is one of the most significant causes of this poorer catalytic activity. Since  $H^+$  is not present, the HER in alkaline media begins by dissociating  $H_2O$  molecules to produce protons. This process is involved in both the Volmer step (Equation 5) and the Heyrovsky step (Equation 6) of alkaline HER, although the Tafel step is the same as it is in acid solutions. Equation (7) outlines the general reaction mechanism, and the reaction's  $E^0$  in relation to the standard hydrogen electrode (SHE) is -0.826 V.

The HER kinetics on most catalysts is slower in alkaline electrolytes because more energy is needed to produce protons in alkaline medium. Alkaline HER activity is reportedly regulated by a fine equilibrium between  $\Delta GH^\circ$  and the energy needed to dissociate  $H_2O$  [36].  $MoS_2$  and  $Co_2P$  are two HER catalysts that are not preferred for the water dissociation process, albeit [42, 43]. Consequently, a useful method for creating effective catalysts for alkaline HER is to encourage the process of water dissociation while maintaining a moderate hydrogen adsorption energy.

- *Alkaline media:*



## 2.3 General Approaches for Evaluating Catalytic Performance

### 2.3.1 Overpotential

Since a large overpotential is what causes the electrochemical water electrolysis system's poor energy conversion efficiency, overpotential is one of the most crucial values for evaluating a water splitting catalyst [35]. Overpotential is the difference between the experimentally observed potential and the thermodynamically determined potential of an electrochemical reaction. Small sweep rates (e.g., 2 mV s<sup>-1</sup>, 5 mV s<sup>-1</sup>) are frequently used to reduce the nonfaradic current while doing linear sweep voltammetry (LSV), which is frequently used to obtain the overpotential. The activation of the reaction, the diffusion of charge carriers, and the series resistance could be the causes of the overpotential. To be more specific, the overpotentials brought on by series resistance and charge-carrier diffusion primarily originate from the water electrolysis system, whereas the overpotentials brought on by activation directly relate to catalytic activity. To more accurately quantify the catalytic activity of the materials, the activation overpotential should therefore be carefully studied. The diffusion overpotential can be effectively reduced by using a rotate disc electrode (RDE) technology, in which the electrode rotates continuously while LSV curves are being recorded. In the meantime, IR compensation (Equation (8)), where  $I$  is the current flowing in the circuit and  $R_s$  is the series resistance, can be used to rectify the resistance overpotential.

$$E_{corrected} = E_{uncorrected} - IR_s \quad (8)$$

Traditionally, a benchmark for measuring catalyst performance is provided using the overpotential at 10 mA cm<sup>2</sup>, which corresponds to the working current density of the most economically viable photoelectrochemical water splitting system [44, 45]. The geometric area of the electrode, which can alternatively be computed based on the specific geometric area of the catalyst, the specific area of the catalyst that is electrochemically active, or the mass of the catalyst, is typically used to determine the current density.

### 2.3.2 Tafel Slope and Exchange Current Density

Tafel slope, which may be produced by replotting the matching LSV curve, is the slope of the linear region of a Tafel plot (overpotential vs  $\log |\text{current density}|$ ). Notably, Tafel slope can give insight on the catalyst surface HER reaction mechanism. For the Volmer step, Heyrovsky step, and Tafel step in HER, the predicted Tafel slope is 120, 40, and 30  $\text{mV dec}^{-1}$ , respectively [34, 46]. For instance, the Volmer-Tafel method is used to carry out the reaction, and the Tafel step is the rate-determining step (RDS) for the reaction, as shown by the HER on the surface of commercial Pt in 0.5 M  $\text{H}_2\text{SO}_4$ , which is near to 30  $\text{mV dec}^{-1}$  [47]. When evaluating the RDS of HER using the Tafel slope, it is typical to assume that  $\text{H}^*$  has an extreme coverage ( $\theta \approx 0$  or  $\approx 1$ ). The Tafel slope, however, depends on coverage in reality. An erroneous depiction of the reaction will result from an overly simplistic interpretation of the Tafel slope [48]. The current density at the equilibrium potential, where the cathodic current and the anodic current are equal, is known as the exchange current density of a reaction [35]. It can be determined by looking at the point where the projected linear portion of Tafel plots intersects with the X-axis. In essence, exchange current density reflects the inherent activity of charge transfer between electrode and electrolyte, and promoting the exchange current density is equivalent to catalysing a reaction [49]. The surface of catalysts with increased catalytic activity often has a higher exchange current density. As an illustration, the current densities of HER on the surfaces of Pt, Ti, and Hg in 0.5 M  $\text{H}_2\text{SO}_4$  are approximately 1,  $10^{-5}$ , and  $10^{-9}$   $\text{mA cm}^{-2}$ , respectively [50].

### 2.3.3 Turnover Frequency

According to Equation (9) [51, 52], the turnover frequency (TOF) is the quantity of product molecules produced per active site per unit of time.  $\text{H}_2$  should be gathered to determine the number of  $\text{H}_2$  molecules, according the definition. According to Faraday's laws of electrolysis (Equation (10), where  $\mathbf{n}$  is the amount of substance (mol),  $\mathbf{I}$  is current (A),  $\mathbf{z}$  is the number of electrons transferred per molecule, and  $\mathbf{F}$  is the Faraday constant ( $96485 \text{ C mol}^{-1}$ ), the theoretical number of  $\text{H}_2$  can be calculated from the charge flowing through the circuit under the assumption that the Faradic efficiency is 100 percent. Then, using Equation (9) and Equation (10) together, a TOF vs overpotential curve can be obtained as Equation (11). Therefore, determining the number of active sites is crucial for calculating TOF. This can be

done using a variety of techniques, such as the copper underpotential deposition method [14], counting the molecules on the exposed surface [53–55], or quantifying from cyclic voltammetry (CV) tests [56–58]. Evidently, how the number of active sites is defined and assessed determines whether a realistic TOF or TOF-overpotential curve may be obtained. It is noted that as TOF increases with rising overpotentials, the overpotential value should always be stated when reporting the TOF values.

$$TOF = \frac{\text{molecule number of product}}{\text{number of active sites}} \times \frac{1}{\text{unit time}} \quad (9)$$

$$n = \frac{I_t}{zF} \quad (10)$$

$$TOF = \frac{I \times N_A}{zF \times \text{number of active sites}} \quad (11)$$

### 2.3.4 Stability

Regarding practical use, stability or durability is a crucial descriptor of a catalyst because it shows the catalyst's capacity to sustain its initial activity over an extended period of time. By observing the variation in the applied overpotential at a certain current density or the change in cathodic current density at an applied overpotential over time, the stability may be assessed. Continuous CV cycling can also be used to assess it. Since LSV curves are typically recorded before and after the stability test, if the catalyst loses its activity quickly, the overpotential will be clearly increased. It should be noted that the current methods are concentrated on assessing stability during active settings, and there are no reliable methods for assessing stability under inactive conditions.



## 2.4 Introduction to Oxygen Reduction Reaction (ORR)

The element that is most prevalent in the crust of the Earth is oxygen ( $O_2$ ). In energy-converting systems like fuel cells and life processes like biological respiration, the oxygen reduction reaction (ORR) is also the most significant reaction. The direct 4-electron reduction pathway from  $O_2$  to  $H_2O$  and the 2-electron reduction pathway from  $O_2$  to hydrogen peroxide ( $H_2O_2$ ) are the two main methods by which ORR in aqueous solutions happens. It is also possible for the 1-electron reduction pathway from  $O_2$  to superoxide ( $O_2^{\cdot-}$ ) to take place in non-aqueous aprotic solvents and/or alkaline solutions.

ORR is the reaction taking place at the cathode in proton exchange membrane (PEM) fuel cells, especially direct methanol fuel cells (DMFCs). The ORR kinetics is typically very sluggish. A cathode ORR catalyst is required to accelerate the ORR kinetics to a useful level in a fuel cell. Platinum (Pt)-based compounds are the most useful catalysts at this point in technology. The development of substitute catalysts, particularly catalysts made of non-noble metals, has been the focus of intensive research over the past few decades because these Pt-based catalysts are too expensive to be used in the production of commercially viable fuel cells [59]. *These electrocatalysts include transition metal macrocyclic compounds, transition metal chalcogenides, and transition metal carbides, as well as noble metals and alloys, carbon materials, quinone, and its derivatives.*

## 2.5 Electrochemical $O_2$ reduction reactions

Table 1 displays a number of typical ORR processes along with the standard conditions' related thermodynamic electrode potentials. The composition of the electrode material, catalyst, and electrolyte are the main determinants of the electrochemical  $O_2$  reduction reaction's process, which is highly complex and contains numerous intermediates.

Depending on the applications, each of the reduction pathways in Table 1—such as the 1-, 2-, and 4-electron reduction pathways—has a special relevance. The 4-electron direct pathway is strongly favoured in fuel cell processes. In the industrial setting, the electron reduction process is used to produce  $H_2O_2$ . The investigation of the ORR mechanism must take into account the 1 electron reduction pathway.

**Table 2.1:** Thermodynamic electrode potentials of electrochemical O<sub>2</sub> reductions [60, 61]

ELECTROLYTE	ORR REACTIONS	THERMODYNAMIC ELECTRODE POTENTIAL AT STANDARD CONDITIONS, V
Acidic aqueous solution	$O_2 + 4H^+ + 4e^- \rightarrow H_2O$	1.229
	$O_2 + 2H^+ + 2e^- \rightarrow H_2O_2$	0.70
	$H_2O_2 + 2H^+ + 2e^- \rightarrow 2H_2O$	1.76
Alkaline aqueous solution	$O_2 + H_2O + 4e^- \rightarrow 4OH^-$	0.401
	$O_2 + H_2O + 2e^- \rightarrow HO_2^- + OH^-$	-0.065
	$HO_2^- + H_2O + 2e^- \rightarrow 3OH^-$	0.867
Non-aqueous aprotic solvents	$O_2 + e^- \rightarrow O_2^-$	a
	$O_2^- + e^- \rightarrow O_2^{2-}$	b

*a, b: Because the values of the thermodynamic potentials for the 1-electron reduction reaction to generate a superoxide and its subsequent reduction to O<sub>2</sub><sup>2-</sup> are highly dependent on the solvent utilised, they are not mentioned in **Table 2.1**.*

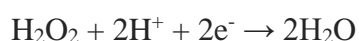
## 2.6 Mechanism of ORR

The hydrogen oxidation reaction (HOR) and the oxygen reduction reaction (ORR) are the two key reactions that enable a fuel cell to generate current [66–68]. The HOR occurs on the anode and normally has a minimal overpotential, but the ORR occurs at the cathode and has a substantial kinetic inhibition given the strong (di) oxygen double bond resulting in a large energy input to activate the reaction [66, 71]. As a result, the ORR determines the rate at which output energy is produced from the initial H<sub>2</sub> fuel source. Given this, it is conceivable

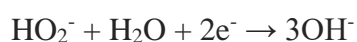
to significantly boost fuel cell efficiency by lowering the overpotential at which ORR occurs at the cathode [69, 70]. As a result, the process will be "more energetically favourable." However, the reaction process is reliant on the pH of the electrode material and/or electrolyte utilised [72]. Ideally, this reaction mixes O<sub>2</sub> (usually atmospheric, in the case of PEM fuel cells) with hydrogen (H<sub>2</sub>) to form H<sub>2</sub>O. The ORR has shown to be problematic in fuel cells because it causes electrode fouling and membrane deterioration when the used electrode decreases O<sub>2</sub> via a 2 electron pathway (see below), which produces H<sub>2</sub>O<sub>2</sub> in an undesirable way [73].

The primary factor limiting the longevity of this PEM fuel cell is H<sub>2</sub>O<sub>2</sub>-induced electrode fouling, which may reduce voltage output by up to 50% due to cathode corrosion (slow ORR kinetics) [74]. PEM fuel cell deterioration is also a major component in this fuel cell's short lifespan. Although both direct [75] and indirect [73] attack mechanisms has been put forth in the literature, the precise mechanism of H<sub>2</sub>O<sub>2</sub> poisoning of the cathode remains unknown. The following are the ORR processes in alkaline and acidic media [76, 77].

- *Acidic media:*



- *Alkaline media:*



It is crucial to use an effective electrocatalyst in order to favour a direct and more efficient 4-electron pathway, which solely yields water as a product and prevents the creation of H<sub>2</sub>O<sub>2</sub>.

## 2.7 Techniques used in Electrocatalytic O<sub>2</sub> reduction

Steady-state polarisation, cyclic voltammetry, rotating disc electrode (RDE), and rotating ring disc electrode (RRDE) are the methods utilised for ORR catalysis research most commonly.

### 2.7.1 Steady state polarization

Polarization means that the potential of the electrode surface shifts away from its equilibrium value, leading to an electrochemical reaction. In general, for an elementary electrochemical reaction,  $\text{O} + \text{e}^- \rightarrow \text{R}$ , the polarization follows the **Butler-Volmer** equation [61],

$$i = i^0 \left( e^{\frac{\beta F \eta}{KT}} - e^{(1-\beta)F\eta/KT} \right)$$

Where  $i^0$  is the exchange current density,  $\eta$  is the overpotential for the reduction of reactant O, and  $\beta$  is the symmetry factor. In the reaction, only part of the overpotential activates the forward reaction, and the symmetry factor represents the fraction of the overpotential affecting the forward reaction. All other parameters have their usual significance.

Most of the electrochemical reactions, however, are not elementary, especially for multiple electron transfer reactions. Even a 1-electron transfer reaction may involve several other steps. The whole reaction consists of multiple elementary reactions, including electron transfer steps and chemical steps. Each elementary reaction has a reaction rate. Each elementary step involving electron transfer gives a **Butler-Volmer** equation, and each chemical step gives a reaction rate equation. The whole reaction rate or electrochemical current is determined by the slowest step. Other steps also contribute to the whole reaction rate, depending on their reaction rates. Deduction of the whole reaction rate is complicated. In some cases, a chemical step is the **rate determining step (rds)**. To simplify, for an electrochemical reaction involving multiple electron transfer, the rate determining step is considered a pseudo-elementary step with an electron transfer number of  $n$ . For ORR,  $n$  might be 1 or 2, depending on the catalysts used and the potential range. This pseudo-elementary step gives a current overpotential relationship, as shown in Equation,

$$i = i^0 \left( e^{\frac{\alpha n F \eta}{KT}} - e^{(1-\alpha)nF\eta/KT} \right)$$

Where  $n$  is the electron transfer number in the pseudo-elementary rate determining step, and  $\alpha$  is the transfer coefficient representing the fraction of overpotential that activates the forward direction of the pseudo-elementary rate determining step.

### 2.7.2 Cyclic voltammetry

Cyclic voltammetry is the most useful technique in electrochemistry. It can quickly provide qualitative information about catalysts and electrochemical reactions, such as the electrochemical response of catalysts and the catalytic activity of the catalysts with respect to some electrochemical reactions. Here, we simply look at the application of the technique in ORR catalyzed by surface adsorbed catalysts.

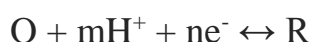
From the slope of *CV curve*, the electron number can be calculated according to the following equation [61, 62],

$$I_p = (n^2 F^2 A \nu \Gamma) / 4RT$$

Where  $n$  is the electron transfer number involved in the electrochemical reaction,  $A$  is the electrode area,  $\nu$  is the potential scan rate, and  $\Gamma$  is the surface concentration of the absorbed species. From the *slope* of  $I_p$  vs.  $\nu$ , the surface concentration can be calculated.

The redox peak potential change that occurs with pH change sheds light on the electrochemical reaction mechanism of the surface adsorbed species. For a reaction involving either a proton or  $\text{OH}^-$

Example:



the change in the formal potential (the average of the anodic potential and cathodic potential) vs. pH follows the equation:

$$E^f = E^0 - 2.303(mRT/nF)pH$$

Where  $E^f$  is the formal potential,  $E^0$  is the Nernst potential, and the other terms have their usual significance [61, 63, 64].

The *onset potential and peak current* demonstrate the catalytic activity of a catalyst.

### 2.7.3 Rotating disk electrode (RDE)

Equations used for RDEs are as follows [61],

$$\frac{1}{I} = \frac{1}{I_K} + \frac{1}{I_{lev}}$$

(the Koutecky-Levich equation) where  $I$  is the disk current,  $I_K$  is the kinetic current density, and  $I_{lev}$  is the Levich current density.  $I_K$  can be expressed,

$$I_K = nFAK_{O_2}C_{O_2}\Gamma_{catalyst}$$

Where  $n$  is the overall electron transfer number,  $A$  is the electrode area,  $C_{O_2}$  is the concentration of dissolved  $O_2$ , and  $\Gamma_{catalyst}$  is the surface concentration of the catalyst, or the catalyst loading.  $I_{lev}$  can be expressed as Equation,

$$I_{lev} = 0.201nFAC_{O_2}(D_{O_2})^{2/3}\nu^{-1/6}\omega^{1/2}$$

Where  $D_{O_2}$  is the diffusion coefficient of  $O_2$ ,  $\nu$  is the kinematic viscosity of the electrolyte solution, and  $\omega$  is the rotation rate represented by rpm.

For RDE data analysis, three non-electrochemical kinetic parameters, such as the diffusion coefficient of  $O_2$ , the kinematic viscosity of the electrolyte solution, and the solubility of  $O_2$  must be known accurately. These parameters are all temperature dependent. Their values are also slightly dependent on the electrolyte used.

### 2.7.4 Rotating ring-disk electrode (RRDE)

In the RRDE method, the  $O_2$  reduction reaction occurring on the disk electrode produces intermediates, which can be detected on the ring and are used to deduce the ORR mechanism. An example is using RRDE to study the  $O_2$  reduction reaction catalyzed by Pt/C catalysts with different particle sizes. On the disk, 2-electron and 4-electron ORR can occur and on the ring electrode,  $H_2O_2$  is further oxidized to  $H_2O$ .

The 2-electron reduction current is given by ( $I_{2e}$ ) is given by,

$$I_{2e} = I_R/N$$

Where  $I_{2e}$  is the 2-electron on the disk electrode and  $N$  is the collecting coefficient number.

The ORR current ( $I_D$ ) on disk electrode can be expressed as,

$$I_D = I_{2e} + I_{4e}$$

where  $I_{4e}$  is the 4-electron ORR current. The following equation is used to obtain the average electron number ( $n_e$ ) involved in ORR,

$$\frac{I_D}{n_e} = \frac{I_{4e}}{4} + \frac{I_{2e}}{2}$$

By rearranging above equation we get the following equation, which is used to calculate  $n_e$ :

$$n_e = 4I_D/(I_D + I_R/N)$$

The numbers of electrons calculated are close to 4 for all catalysis investigation, indicating a weak platinum particle-particle size effect on  $H_2O_2$  production. Larger particle size shows a higher proportion of  $H_2O_2$ .

## 2.8 Kinetics of oxygen reduction reaction

It is desirable to have the  $O_2$  reduction reaction occurring at potentials as close as possible to the reversible electrode potential (thermodynamic electrode potential) with a satisfactory reaction rate. The current-overpotential is given in Equation,

$$I_c = i^0 \left( e^{\frac{\alpha n F \eta}{RT}} - e^{-(1-\alpha) n F \eta / RT} \right)$$

Where  $I_c$  is the oxygen reduction reaction current density,  $i^0$  is the exchange current density,  $n$  is the number of electrons transfer in the rate determining step,  $\alpha$  is the transfer coefficient,  $\eta$  is the overpotential of ORR,  $F$  is the Faraday constant,  $R$  is the gas constant, and  $T$  is the temperature in Kelvin. To obtain high current at low overpotential,  $i^0$  should be large or  $RT/\alpha n F$  should be small.

### 2.8.1 Tafel slope

If the overpotential is large, the backward reaction is negligible and above Equation can be simplified as,

$$i_c = i^0 e^{\alpha n F \eta / RT}$$

The plot of  $\eta$  vs  $\log(I_c)$  gives a linear relationship and the slope is called *Tafel slope*. The higher the *tafel slope* the faster the overpotential increases with the current density. Thus, for an electrochemical reaction to obtain a high current at low overpotential, the reaction should exhibit a low Tafel slope or a large  $\alpha n$ . For ORR, usually two Tafel slopes are obtained, 60mV/dec and 120mV/dec, respectively, depending on the electrode materials used and on the potential range. The electron transfer co-efficient is a key factor determining tafel slope. For ORR, the transfer co-efficient is dependent on temperature.

### 2.8.2 Exchange current density

Exchange current density is an important kinetic parameter representing the electrochemical reaction rate at equilibrium. For an electrochemical reaction,



both forward and backward reactions can occur. The reaction's net current density is zero when it is in equilibrium. The forward reaction's current density is the same as the backward reaction's [61]. Exchange current density is the name given to this current density. The rate of the electrochemical reaction is determined by the magnitude of the exchange current density. An electrochemical reaction's exchange current density is influenced by both the reaction itself and the electrode surface on which it takes place.



## References:

1. S. Chu, A. Majumdar, *Nature* **2012**, 488, 294.
2. P. Wang, X. Zhang, J. Zhang, S. Wan, S. Guo, G. Lu, J. Yao, X. Huang, *Nat. Commun* 2017, 8, 14580.
3. J. Lim, D. Park, S. S. Jeon, C.-W. Roh, J. Choi, D. Yoon, M. Park, H. Jung, H. Lee, *Adv. Funct. Mater.* 2018, 28, 1704796.
4. J. Ying, G. Jiang, Z. P. Cano, L. Han, X.-Y. Yang, Z. Chen, *Nano Energy* 2017, 40, 88.
5. L. Zhang, L. Han, H. Liu, X. Liu, J. Luo, *Angew. Chem., Int. Ed.* 2017, 56, 13694.
6. Y. Zhang, Q. Zhou, J. Zhu, Q. Yan, S. X. Dou, W. Sun, *Adv. Funct. Mater.* **2017**, 27, 1702317.
7. H. Fan, H. Yu, Y. Zhang, Y. Zheng, Y. Luo, Z. Dai, B. Li, Y. Zong, Q. Yan, *Angew. Chem.* **2017**, 129, 12740.
8. J. X. Feng, L. X. Ding, S. H. Ye, X. J. He, H. Xu, Y. X. Tong, G. R. Li, *Adv. Mater.* **2015**, 27, 7051.
9. H. Cheng, C.-Y. Su, Z.-Y. Tan, S.-Z. Tai, Z.-Q. Liu, *J. Power Sources* **2017**, 357, 1.
10. G. F. Chen, T. Y. Ma, Z. Q. Liu, N. Li, Y. Z. Su, K. Davey, S. Z. Qiao, *Adv. Funct. Mater.* **2016**, 26, 3314.
11. H. Cheng, Y.-Z. Su, P.-Y. Kuang, G.-F. Chen, Z.-Q. Liu, *J. Mater. Chem. A* **2015**, 3, 19314.
12. D. Yan, Y. Li, J. Huo, R. Chen, L. Dai, S. Wang, *Adv. Mater.* **2017**, 29, 1606459.
13. A.-L. Wang, H. Xu, G.-R. Li, *ACS Energy Lett.* **2016**, 1, 445.
14. D. Voiry, H. Yamaguchi, J. Li, R. Silva, D. C. Alves, T. Fujita, M. Chen, T. Asefa, V. B. Shenoy, G. Eda, M. Chhowalla, *Nat. Mater* **2013**, 12, 850.
15. Y. Kim, D. H. Jackson, D. Lee, M. Choi, T. W. Kim, S. Y. Jeong, H. J. Chae, H. W. Kim, N. Park, H. Chang, *Adv. Funct. Mater.* **2017**, 27, 1701825.
16. C. Xu, S. Peng, C. Tan, H. Ang, H. Tan, H. Zhang, Q. Yan, *J. Mater. Chem. A* **2014**, 2, 5597.
17. C. Ouyang, X. Wang, S. Wang, *Chem. Commun.* **2015**, 51, 14160.
18. L. Tao, X. Duan, C. Wang, X. Duan, S. Wang, *Chem. Commun.* **2015**, 51, 7470.
19. J.-X. Feng, J.-Q. Wu, Y.-X. Tong, G.-R. Li, *J. Am. Chem. Soc.* **2018**, 140, 610.

20. D. Y. Chung, S. W. Jun, G. Yoon, H. Kim, J. M. Yoo, K. S. Lee, T. Kim, H. Shin, A. K. Sinha, S. G. Kwon, K. Kang, T. Hyeon, Y. E. Sung, *J. Am. Chem. Soc.* **2017**, *139*, 6669.
21. J. Zhang, T. Wang, P. Liu, S. Liu, R. Dong, X. Zhuang, M. Chen, X. Feng, *Energy Environ. Sci.* **2016**, *9*, 2789.
22. Z. Zhang, B. Lu, J. Hao, W. Yang, J. Tang, *Chem. Commun.* **2014**, *50*, 11554.
23. A.-L. Wang, J. Lin, H. Xu, Y.-X. Tong, G.-R. Li, *J. Mater. Chem. A* **2016**, *4*, 16992.
24. C. Wan, Y. N. Regmi, B. M. Leonard, *Angew. Chem.* **2014**, *126*, 6525.
25. H. Ang, H. T. Tan, Z. M. Luo, Y. Zhang, Y. Y. Guo, G. Guo, H. Zhang, Q. Yan, *Small* **2015**, *11*, 6278.
26. H. Ang, H. Wang, B. Li, Y. Zong, X. Wang, Q. Yan, *Small* **2016**, *12*, 2859.
27. W. F. Chen, K. Sasaki, C. Ma, A. I. Frenkel, N. Marinkovic, J. T. Muckerman, Y. Zhu, R. R. Adzic, *Angew. Chem., Int. Ed.* **2012**, *51*, 6131.
28. H. Yan, C. Tian, L. Wang, A. Wu, M. Meng, L. Zhao, H. Fu, *Angew. Chem., Int. Ed.* **2015**, *54*, 6325.
29. H. Lin, Z. Shi, S. He, X. Yu, S. Wang, Q. Gao, Y. Tang, *Chem. Sci.* **2016**, *7*, 3399.
30. D. Wang, Q. Li, C. Han, Z. Xing, X. Yang, *ACS Cent. Sci.* **2017**, *4*, 112.
31. K. Rui, G. Zhao, Y. Chen, Y. Lin, Q. Zhou, J. Chen, J. Zhu, W. Sun, W. Huang, S. X. Dou, *Adv. Funct. Mater.* **2018**, *28*, 1801554.
32. S. Dou, J. Wu, L. Tao, A. Shen, J. Huo, S. Wang, *Nanotechnology* **2015**, *27*, 045402.
33. Y. Chen, Q. Zhou, G. Zhao, Z. Yu, X. Wang, S. X. Dou, W. Sun, *Adv. Funct. Mater.* **2018**, *28*, 1705583.
34. B. Conway, B. Tilak, *Electrochim. Acta* **2002**, *47*, 3571.
35. A. J. Bard, L. R. Faulkner, J. Leddy, C. G. Zoski, *Electrochemical Methods: Fundamentals and Applications*, Wiley, New York **1980**.
36. N. Danilovic, R. Subbaraman, D. Strmcnik, V. R. Stamenkovic, N. M. Markovic, *J. Serb. Chem. Soc.* **2013**, *78*, 2007.
37. H. Lehmann, X. Fuentes-Arderiu, L. Bertello, *Pure Appl. Chem.* **1996**, *68*, 957.
38. P. Quaino, F. Juarez, E. Santos, W. Schmickler, *Beilstein J. Nanotechnol.* **2014**, *5*, 846.
39. R. Parsons, *Trans. Faraday Soc.* **1958**, *54*, 1053.
40. N. Danilovic, R. Subbaraman, D. Strmcnik, K. C. Chang, A. P. Paulikas, V. R. Stamenkovic, N. M. Markovic, *Angew. Chem., Int. Ed. Engl.* **2012**, *51*, 12495.
41. T. Schmidt, P. Ross, N. Markovic, *J. Electroanal. Chem.* **2002**, *524*, 252

42. K. Xu, H. Ding, M. Zhang, M. Chen, Z. Hao, L. Zhang, C. Wu, Y. Xie, *Adv. Mater.* **2017**, 29, 1606980.
43. K. K. Ghuman, S. Yadav, C. V. Singh, *J. Phys. Chem. C* **2015**, 119, 6518.
44. J. Luo, J.-H. Im, M. T. Mayer, M. Schreier, M. K. Nazeeruddin, N.-G. Park, S. D. Tilley, H. J. Fan, M. Gratzel, *Science* **2014**, 345, 1593.
45. J. D. Benck, T. R. Hellstern, J. Kibsgaard, P. Chakthranont, T. F. Jaramillo, *ACS Catal.* **2014**, 4, 3957.
46. A. R. Kucernak, C. Zalitis, *J. Phys. Chem. C* **2016**, 120, 10721.
47. Y. Li, H. Wang, L. Xie, Y. Liang, G. Hong, H. Dai, *J. Am. Chem. Soc.* **2011**, 133, 7296.
48. T. Shinagawa, A. T. Garcia-Esparza, K. Takanabe, *Sci. Rep.* **2015**, 5, 13801.
49. C. H. Hamann, A. Hamnett, W. Vielstich, Weinheim, *Electrochemistry*, 2nd ed., Wiley-VCH, Weinheim **2007**.
50. C. Cao, *Principles of Electrochemistry of Corrosion*, Chem. Ind. Press, Peking, China **2008**.
51. J. M. Thomas, W. J. Thomas, *Principles and Practice of Heterogeneous Catalysis*, John Wiley & Sons, Weinheim **2014**.
52. C. Costentin, S. Drouet, M. Robert, J. M. Saveant, *J. Am. Chem. Soc.* **2012**, 134, 11235.
53. H. Li, C. Tsai, A. L. Koh, L. Cai, A. W. Contryman, A. H. Fragapane, J. Zhao, H. S. Han, H. C. Manoharan, F. Abild-Pedersen, *Nat. Mater.* **2016**, 15, 48
54. S. Shin, Z. Jin, D. H. Kwon, R. Bose, Y. S. Min, *Langmuir* **2015**, 31, 1196.
55. J. Kibsgaard, T. F. Jaramillo, F. Besenbacher, *Nat. Chem.* **2014**, 6, 248.
56. Y. Yan, X. Ge, Z. Liu, J. Y. Wang, J. M. Lee, X. Wang, *Nanoscale* **2013**, 5, 7768.
57. D. Mukherjee, P. M. Austeria, S. Sampath, *ACS Energy Lett.* **2016**, 1, 367.
58. J. Zhang, L. Zhao, A. Liu, X. Li, H. Wu, C. Lu, *Electrochim. Acta* **2015**, 182, 652.
59. Zhang L, Zhang J, Wilkinson DP, Wang H. Progress in preparation of non-noble electrocatalysts for PEM fuel cell reactions. *J Power Sources* 2006;156.2:171-82.
60. Yeager E. Dioxygen electrocatalysis: mechanism in relation to catalyst structure. *J Mol Catal* 1986;38:5-25.
61. Bard AJ, Faulkner LR. *Electrochemical methods: fundamentals and applications*. New York: Wiley, 1980.

62. Baker R, Wilkinson DP, Zhang J. Electrocatalytic activity and stability of substituted iron phthalocyanines towards oxygen reduction evaluated at different temperatures. *Electrochim Acta*. Forthcoming 2008.
63. Lever ABP. The phthalocyanines-molecules of enduring value: a two-dimensional analysis of redox potentials. *J Porphyrins Phthalocyanines* 1999;3:488-99.
64. Zhang L, Song C, Zhang J, Wang H, Wilkinson DP. Temperature and pH dependent oxygen reduction catalyzed by iron fluoro-porphyrin adsorbed on a graphite electrode, *J Electrochem Soc* 2005;152:A2421-6.
65. Antoine O, Durand R. RRDE study of oxygen reduction on Pt nanoparticles inside Nafion: H<sub>2</sub>O<sub>2</sub> production in PEMFC cathode conditions. *J Appl Electrochem* 2000;30:839-844.
66. T. J. Schmidt, U. A. Paulus, H. A. Gasteiger and R. J. Behm, *J. Electroanal. Chem.*, 2001, 508, 41-47.
67. D. Banham, S. Ye, K. Pei, J. Ozaki, T. Kishimoto and Y. Imashiro, *J. Power Sources*, 2015, 285, 334-348.
68. M.-R. Gao, J.-X. Liang, Y.-R. Zheng, Y.-F. Xu, J. Jiang, Q. Gao, J. Li and S.-H. Yu, *Nat. Commun.*, 2015, 6, 5982.
69. Y. Liu, X. Yue, K. Li, J. Qiao, D. P. Wilkinson and J. Zhang, *Coord. Chem. Rev.*, 2016, 315, 153-177.
70. M.-R. Gao, Y.-F. Xu, J. Jiang, Y.-R. Zheng and S.-H. Yu, *J. Am. Chem. Soc.*, 2012, 134, 2930-2933.
71. A. A. Gewirth and M. S. Thorum, *Inorg. Chem.*, 2010, 49, 3557-3566.
72. M. Gara and R. C. Compton, *New J. Chem.*, 2011, 35, 2647-2652.
73. L. Gubler, S. M. Dockheer and W. H. Koppenol, *J. Electrochem. Soc.*, 2011, 158, B755-B769.
74. K. Uosaki, G. Elumalai, H. Noguchi, T. Masuda, A. Lyalin, A. Nakayama and T. Taketsugu, *J. Am. Chem. Soc.*, 2014, 136, 6542-6545.
75. F. Jaouen, E. Proietti, M. Lefevre, R. Chenitz, J.-P. Dodelet, G. Wu, H. T. Chung, C.M. Johnston and P. Zelenay, *Energy Environ. Sci.*, 2011, 4, 114-130.
76. M. Gara and R. G. Compton, *New J. Chem.*, 2011, 35, 2647-2652.
77. E. P. Randviir and C. E. Banks, *Electroanalysis*, 2014, 26, 6-83.

# **CHAPTER 3**

## **REVIEW OF PAST WORK**

### 3.1 General Idea

Due to its distinct structure and intriguing features, MoS<sub>2</sub> has become one of the newest types of ultrathin two-dimensional (2D) transition-metal dichalcogenide (TMD) nanomaterials, which are generating a lot of scientific attention. An overview of current developments in MoS<sub>2</sub> nanosheets is provided in the first section of this Review, with a focus on their methods of synthesis and functionalization. In order to provide an overview of this novel material and address the prospects and problems in this exciting research field, we present a summary of the most recent works on MoS<sub>2</sub>-based materials. Additionally, we talked on the synthesis, characterization, and development of solution-processed MoS<sub>2</sub> nanosheets. MoS<sub>2</sub> nanosheets prepared for solution will be categorised and highlighted. Then, a thorough explanation of the methods used to separate and sort the various MoS<sub>2</sub> nanosheet layers is given.

The second section provides a summary of current developments on various forms of doping on MoS<sub>2</sub> material. There have also been multiple reports of "substitutional doping" of MoS<sub>2</sub>, in which the S anion and the Mo cation have both had their atoms replaced by suitable "donor" or "acceptor" dopant atoms to produce, respectively, n-type and p-type MoS<sub>2</sub>. The conventional methods for n- and p-doping MoS<sub>2</sub> have included gate electrostatic doping using highly capacitive dielectrics or liquid/solid electrolytes, surface charge transfer doping (via adsorption or encapsulation of electron-donating or electron-accepting species), and doping via electrostatic dipole interactions at the MoS<sub>2</sub>/dielectric interface. With an emphasis on the connection between the intrinsic electronic structure of MoS<sub>2</sub> and its electrocatalytic activity, we conclude this study by systematically reviewing the recent advancements in controlling electronic structures for electrochemical hydrogen production.

### 3.2 Synthesis and Characterization of MoS<sub>2</sub> Nanosheets

Liquid phase exfoliation methods (top-down method) and wet chemical synthesis methods (bottom-up method) are two categories into which solution-based MoS<sub>2</sub> nanosheet fabrication processes can be divided. The primary goal of liquid-phase exfoliation, which is referred to as a dispersion/exfoliation technique, is to lessen the interaction between neighboring layers of MoS<sub>2</sub>. Dispersion chemicals, such as reaction reagents, solvents, or surfactants, are required to accomplish this purpose and have a significant impact on the exfoliation yield and quality

of MoS<sub>2</sub> nanosheets [1-3]. The interlayer contacts of MoS<sub>2</sub> are weakened due to the affinity between host materials and dispersion chemicals, and subsequent sonication results in the isolation of sheets. Contrarily, the wet chemical technique is a typical bottom-up method that creates MoS<sub>2</sub> nanosheets by using metal-salt reactions as precursors [4, 5].

### 3.2.1 Ion-Intercalation/Exfoliation Methods

To increase the exfoliation effectiveness of multilayer materials, inorganic ions are useful intercalators. Ion intercalation is thought to take place in highly anisotropic layered structures with weak interlayer contacts, according to investigations on graphene. Only Lewis bases and alkali-metal ions with short radii can penetrate the interlayer space of bulk MoS<sub>2</sub> due to its narrow interlayer space, which is around 6.5 Å [6]. MoS<sub>2</sub> nanosheets have been exfoliated using Li-ion intercalation, which is often one of the most well-liked and effective techniques for doing so. This process typically involves three steps: sonication of the compounds, immersion of the Li-intercalated compounds in water, and intercalation of Li<sup>+</sup> ions into the interlayer region of bulk MoS<sub>2</sub>. It is interesting that MoS<sub>2</sub>'s structure may change from the hexagonal (2H) phase to the octahedral (1T) phase as a result of Li-ion intercalation. The 2H-MoS<sub>2</sub> is semi-conductive, but the 1T-MoS<sub>2</sub> is metallic [7]. Recently, Loh et al. used a two-step expansion and intercalation procedure to create high-quality single-layer MoS<sub>2</sub> nanosheets [8]. Bulk MoS<sub>2</sub> was subjected to a hydrothermal reaction with hydrazine (N<sub>2</sub>H<sub>4</sub>) in order to perform the initial expansion phase. It was discovered that after the dissolution of intercalated N<sub>2</sub>H<sub>4</sub> molecules, the volume of MoS<sub>2</sub> crystals increased by more than 100 times. After that, metal naphthalenide (which contains Li, Na, and K) was intercalated into the expanded MoS<sub>2</sub> crystals in order to cause the exfoliation. After purification, it was possible to produce single-layer MoS<sub>2</sub> nanosheets with a high yield (90 percent) and up to 400 μm<sup>2</sup> in size. The technique is risky since the intercalated chemicals could self-heat, self-ignite, or self-explode in air, despite the exfoliated MoS<sub>2</sub> nanosheets' great efficiency and strong dispersity.

Li-treated MoS<sub>2</sub> nanosheets' immediate recovery of their semiconducting characteristics in solution was demonstrated by Dravid et al. [9]. A biphasic process using oleylamine as the cationic amphiphile reagent was used to first transfer the exfoliated MoS<sub>2</sub> nanosheets from water to organic solvents like o-dichlorobenzene (ODCB). MoS<sub>2</sub> nanosheets were subsequently thermally annealed in inert, high-boiling-point organic solvents like octadecene (boiling point of 315 °C) and o-dichlorobenzene (ODCB) (with boiling point of 180 °C) to

complete the recovery of semiconducting characteristics. It's significant that the modified MoS<sub>2</sub> nanosheets can still be transported and put together to form freestanding films and patterns.

Using non-toxic CuCl<sub>2</sub> and NaCl, Zheng et al. generated single- and few-layer MoS<sub>2</sub> nanosheets [10]. The resulting MoS<sub>2</sub> nanosheets were significant because they maintained their single crystallinity, which is essential for electro-optical applications.

In order to exfoliate MoS<sub>2</sub> in NMP, Choi et al. reported employing MOH (M=Li, Na, and K) as intercalators. In order to encourage the integration of Li<sup>+</sup> (or Na<sup>+</sup>, K<sup>+</sup>, and OH<sup>-</sup>) and OH<sup>-</sup> ions into the interlayer region of MoS<sub>2</sub>, NMP must have a sufficiently high dielectric strength for MoS<sub>2</sub>. This increases the dispersity of MoS<sub>2</sub> nanosheets. Although exfoliation efficiency was increased, the majority of exfoliated MoS<sub>2</sub> nanosheets had a thickness of 1 to 9 nm, or 1 to 9 layers.

### **3.2.2 Surfactant/Polymer-Assisted Exfoliation Methods**

Another workable method for isolating MoS<sub>2</sub> nanosheets is liquid-phase exfoliation, supported by organic chemicals [11, 12]. MoS<sub>2</sub> exfoliation can be considerably aided by small chemical compounds, surfactants, or polymers, particularly those with high adsorption energies on the basal plane of MoS<sub>2</sub> nanosheets.

Coleman et al demonstration's of the creation of MoS<sub>2</sub> nanosheets using 1.5 mg mL<sup>-1</sup> sodium cholate of water serves as a good illustration [12]. As an ionic surfactant, sodium cholate was employed to help exfoliate and stabilise MoS<sub>2</sub> nanosheets, resulting in sodium cholate-coated MoS<sub>2</sub> nanosheets. A measurement of the surface potential revealed that it was -40 mV and that it was resistant to pH changes. Additionally, the dispersion is stable in aqueous solution and can be easily hybridised with carbon nanotubes (CNTs) and graphene.

Han et al. very recently reported using bovine serum albumin (BSA) to exfoliate MoS<sub>2</sub> nanosheets in water [13]. In addition to serving as an effective stabilising agent to prevent the aggregation of MoS<sub>2</sub> nanosheets, BSA is used as an exfoliating agent. BSA can also adsorb on MoS<sub>2</sub> layers in a manner akin to the PVP-assisted exfoliation procedure. The developed composites have a high pesticide binding capability and good biocompatibility.



### 3.2.3 Solvent-Assisted Exfoliation Methods

One of the simplest techniques for exfoliating layered materials is the solvent-assisted exfoliation approach, which involves soaking stacked bulk materials in organic solvents before sonicating [14]. The process for exfoliating graphite into graphene has been thoroughly developed [15]. It has been established that the exfoliation yield is significantly influenced by the dispersion solvents. When the surface tension of the solvent equals that of the layered materials, the energy cost of exfoliation when a solid surface is submerged in a liquid medium becomes low. Importantly, the right solvent ensures that nanosheets are dispersed without re-stacking or agglomeration.

Recent research by Lu et al. [16] has shown that mild circumstances could allow MoS<sub>2</sub> to spontaneously exfoliate when H<sub>2</sub>O<sub>2</sub> and NMP are combined. Over 60 weight percent of MoS<sub>2</sub> nanosheets are produced. It's interesting to note that H<sub>2</sub>O<sub>2</sub> can simultaneously dissolve MoS<sub>2</sub> nanosheets and cause the spontaneous exfoliation of MoS<sub>2</sub> in NMP. The shape of the MoS<sub>2</sub> samples produced changed from porous nanosheets to nanodots, which were created in a high concentration of H<sub>2</sub>O<sub>2</sub>, by precisely adjusting the H<sub>2</sub>O<sub>2</sub> concentration. Although adding H<sub>2</sub>O<sub>2</sub> to NMP can increase the yield of MoS<sub>2</sub> nanosheets that are exfoliated, this approach is challenging to employ because H<sub>2</sub>O<sub>2</sub> can unexpectedly oxidise MoS<sub>2</sub> and create defects.

### 3.2.4 Sonication Methods

MoS<sub>2</sub> nanosheets can also be made using external force to increase exfoliation efficiency. MoS<sub>2</sub> layers were typically separated from the bulk materials by mechanical grinding, which produced shear stress and increased the exfoliation yield of MoS<sub>2</sub> nanosheets.

For instance, Wong et al. [17] used a combination of grinding and sonication procedures to create high-concentration aqueous solutions of MoS<sub>2</sub> nanosheets. In a nutshell, NMP was used to first grind bulk MoS<sub>2</sub> powder. Centrifugation was used to separate MoS<sub>2</sub> from NMP, and after that, they were sonicated in an ethanol/water solution (v:v=45:55). Similar methods for exfoliating MoS<sub>2</sub> by grinding-assisted sonication have been used with the NMP solution [18] and a solution of sodium dodecyl sulphate (SDS) and water [19].

Recent research by Wei et al. has shown that the "quenching cracks" caused by liquid N<sub>2</sub> can significantly improve the exfoliation efficiency of MoS<sub>2</sub> nanosheets because immediate cooling can dissolve the van der Waals interaction between adjacent layers of MoS<sub>2</sub> [20].

However, this procedure needs to be used with caution because liquid N<sub>2</sub> needs to be handled carefully.

MoS<sub>2</sub> nanosheets can also be exfoliated electrochemically utilising a two electrode cell as an alternative method. As an illustration, Lee et al. described the electrochemical exfoliation of MoS<sub>2</sub> utilising Na<sub>2</sub>SO<sub>4</sub> solution as the electrolyte, Pt wire as the counter electrode, and a bulk MoS<sub>2</sub> crystal as the working electrode [21]. The two-electrode setup was given a direct current (DC) bias for electrochemical exfoliation. MoS<sub>2</sub> nanosheet yield was between 5 and 9 percent, and the concentration was between 0.007 and 0.014 mgmL<sup>-1</sup>. The lateral size of exfoliated MoS<sub>2</sub> nanosheets was significant, measuring 5–50 nm. However, rather than being evenly dispersed single-layer nanosheets, the majority of the produced nanosheets were multi-layers. Additionally, a slight amount of oxidation of the exfoliated MoS<sub>2</sub> nanosheets occurs during the electrochemical exfoliation.

### 3.2.5 Wet Chemical Synthesis Methods

MoS<sub>2</sub> nanosheets of the necessary size and thickness have been created using bottom-up wet chemical synthesis procedures. Using metal salts as precursors, hydrothermal and hot-injection methods are two common techniques for producing MoS<sub>2</sub> nanosheets. The simplicity and broad applicability of the hydrothermal approach make it appealing [22–24]. Typically, the hydrothermal process is carried out in a sealed autoclave at a high vapour pressure and temperature.

Rao et al. produced MoS<sub>2</sub> nanosheets as a typical example by hydrothermally processing MoO<sub>3</sub> and KSCN (as the sulphur source) in water at 453 K. Layer separations of 0.65–0.7 nm and few-layer thicknesses of MoS<sub>2</sub> nanosheets were achieved.

In a recent experiment, Xie et al. showed how to create hydrothermally defect-rich MoS<sub>2</sub> nanosheets. Thiourea was added to the process to stabilise the extremely thin MoS<sub>2</sub> nanosheets as well as decrease Mo (VI) to Mo (IV) [25]. Take into consideration that the hydrothermal process takes place at high pressure and temperature, and the MoS<sub>2</sub> nanosheets that are produced typically combine to form structures like nanoflowers [26] and nanotubes.

By decomposing single source precursors, specifically ammonium tetrathiomolybdate, at a high temperature (360°C) in the presence of oleylamine, Altavilla et al. reported the synthesis of free-standing MoS<sub>2</sub> nanosheets [27]. In a nutshell, the precursor—ammonium

tetrathiomolybdate—was mixed in oleylamine under N<sub>2</sub> flow for 15 minutes at 100°C. The mixture was then heated to 360°C. Importantly, when the reaction period increases from 30 to 90 minutes, the thickness of the MoS<sub>2</sub> nanosheets produced may be controlled from one layer to a few layers. Take into consideration that the oleylamine coating on the MoS<sub>2</sub> nanosheets maintained their suspension and stopped them from aggregating and oxidising.

### 3.3 Sorting and Separation Strategies

One of the unique characteristics of the solution-processed MoS<sub>2</sub> nanosheet in comparison to those made by mechanical and CVD processes is how readily it can be sorted and separated. MoS<sub>2</sub> nanosheets that have been produced in solution typically have a wide lateral size variation and a range of thicknesses. As is common knowledge, the size and thickness of MoS<sub>2</sub> nanosheets have a significant impact on their physical and electrical properties. For practical applications, it is crucial to manufacture MoS<sub>2</sub> nanosheets that are homogeneous in size and thickness. MoS<sub>2</sub> nanosheet sorting techniques have so far mostly focused on density-gradient ultracentrifugation and sedimentation-based separation. One of the most popular techniques for separating 2D nanomaterials is sedimentation-based separation, which has been utilised to separate MoS<sub>2</sub> flakes of varied sizes and thicknesses. It is based on the various rates at which flakes settle out in response to centrifugal forces. Large, relatively heavy flakes can typically be precipitated by centrifugation, but small, relatively light flakes tend to remain at the top of the dispersion.

*The following is a description of sedimentation-based separation:*

A centrifuge tube is filled with a MoS<sub>2</sub> suspension and spun in a centrifuge. The exfoliated single-layer MoS<sub>2</sub> nanosheets could precipitate significantly slower than the big size, heavy weight MoS<sub>2</sub> flakes, which is similar to prior sorting results for graphene. As a result, after centrifugation, the various sizes of MoS<sub>2</sub> are separated, with the exfoliated nanosheets remaining close to the top and the largest MoS<sub>2</sub> flakes at the bottom of the centrifuge tube. As a result, this technique is quite effective at removing huge, non-exfoliated MoS<sub>2</sub> flakes. Importantly, the characteristics of the dispersion solvent have a major role in this separation process. Because of their various viscosities, MoS<sub>2</sub> nanosheets in NMP, for example, are typically bigger in size than those in water/surfactant dispersions. At room temperature, NMP's viscosity (1.7 MPas) is greater than water's (around 1 MPas). When large flakes are

scattered in a high-viscosity medium, there is a significant amount of frictional force, which lowers the sedimentation coefficient and makes precipitation difficult [28]. This technique has been the most widely used approach for separating MoS<sub>2</sub> nanosheets so far.

Another technique for separating mixtures with various buoyant densities is density-gradient ultracentrifugation [29, 30]. Typically, liquids and samples are combined in a centrifuge tube to create a density profile with a variable geographic distribution. The samples are divided into several zones with various individual densities after being spun at a high speed. It's significant to note that the density-gradient ultracentrifugation can be carried out without a stationary phase and in both aqueous and organic solvents. However, due to the high intrinsic buoyant density of MoS<sub>2</sub>, this technique is rarely employed to sort MoS<sub>2</sub> nanosheets.

### **3.4 Heteroatom Doping in MoS<sub>2</sub>**

Similar to dimensional control, heteroatomic doping of electrocatalysts with various atomic radii and valence electrons is a crucial technique to modify their electronic structure. In order to decrease the hydrogen adsorption free energy ( $\Delta G_{H^*}$ ) in the electrocatalytic reaction and increase the electron transfer rate and conductivity, heteroatomic doping might alter the electronic structure of the original lattice [31–33]. Additionally, partial doping can disclose a significant number of flaws and boost the number of catalytically reactive sites, meeting the goal of boosting catalytic reaction rate [34]. Both nonmetal atom and metal atom doping were used for MoS<sub>2</sub>.

#### **3.4.1 Metal-Atom Doping**

The original lattice tends to distort and cause local electron redistribution as a result of the substituted atoms' differing atomic radii and valence electrons, which is thought to be an efficient way to control conductivity and boost electrocatalytic activity.

For instance, using a novel intralayer doping technique, Xie et al. create the semi-metallic V-doped MoS<sub>2</sub>. Since the V-doped MoS<sub>2</sub> has superior in-plane conductivity, a larger carrier concentration, and a shorter electron transfer path than pure MoS<sub>2</sub>, it exhibits better catalytic activity.

Co-doped MoS<sub>2</sub> was discussed by Bao et al. notably, the quantity of Co doping may cause an excessive reduction in the number of electrons on the S atom, and the contact between the H and S atom grew greater, leading to poor surface stability in MoS<sub>2</sub>, which was also unfavourable to HER activity [51].

The covalent Co-doped MoS<sub>2</sub> with improved HER performances was also reported by Zhao et al. Covalent Co-doping into MoS<sub>2</sub> successfully reduced the band gap from around 1.70 eV to about 0 eV, which was advantageous for high conductivity, according to the related calculated results [36].

Co-incorporated MoS<sub>2</sub> nanosheets with enhanced HER kinetics were also developed by Wei's group [37]. Additionally, Chen's group discovered that doped Ni was responsible for MoS<sub>2</sub>'s HER performance. In their research, they found that Ni-doped MoS<sub>2</sub> had significant NiS bond interactions that controlled the local electrical structures [38].

Additionally, Liu's research shows that the addition of Pt might alter filled p states and the electron density around the S atom, enhancing hydrogen generation performance, because its ionisation energy is higher than that of Mo's [39]. According to recent studies, Ru, Zn, and other dopants might also successfully modify the electronic structure of MoS<sub>2</sub>, expose enough active sites, lower the reaction's energy barrier, and subsequently enhance the activity of the materials.

### **3.4.2 Non-Metal-Atom Doping**

To increase the electrocatalytic activity, nonmetal atoms were additionally doped into MoS<sub>2</sub> to modify its intrinsic conductivity and electronic structure. A changed energy band structure for O-doped MoS<sub>2</sub>, for instance, was reported by Xie et al. Within the band gap of MoS<sub>2</sub>, O doping produced a new energy level. More carriers and greater intrinsic conductivity were produced by the decreased band gap. The charge density distribution further demonstrated that oxygen inclusion had a major impact on the electronic structure by demonstrating more intuitively that oxygen enhances the charge density of the valence band (VB) and conduction band (CB). In a different investigation, P doping in the MoS<sub>2</sub> lattice was shown to control the electronic structures and produce the ideal free energy for hydrogen adsorption. In their research, P-doped MoS<sub>2</sub> has a considerably lower Gibbs free energy (0.04 eV) than virgin MoS<sub>2</sub> (2.2 eV). Thus, P-doped MoS<sub>2</sub> might promote intrinsic electrical conductivity and raise MoS<sub>2</sub>'s HER activity [41].

When N was added to MoS<sub>2</sub>, the Xiao group discovered that it could activate the edge sites and boost the conductivity of the basal planes toward HER [42]. Furthermore, using a simple self-templating method, Gao et al. have generated ultrasmall N-doped MoS<sub>2</sub> nanocrystals. The S- edge's HER performance as well as the conductivity of the basal plane might both be enhanced by N-doped MoS<sub>2</sub>. Additionally, a significant number of flaws in the MoS<sub>2</sub> structure might be created by the N dopants [43].

The electrical structure of the nearby region can unquestionably be tuned efficiently by element doping, which further optimises the adsorption of reactants or intermediates and influences the reaction activity and stability of the MoS<sub>2</sub>. A general understanding of the quantity of doping and how the coordination environment evolves during the doping process is still lacking, despite significant attempts to examine the impact of doping on the electronic structure of MoS<sub>2</sub>.

### 3.4.3 Zn doping

Zn atoms either intercalate between MoS<sub>2</sub> layers or replace Mo in MoS<sub>2</sub> structures to dope them. Since Zn<sup>2+</sup> has less valence electron than Mo<sup>4+</sup>, substitutional doping of Zn creates acceptor levels above the valence band, lowers the Fermi level, and produces the p-type effect, as shown by negative shifts in the Mo 3d and S 2p peaks in the XPS spectra [44, 45].

Zn was utilised by Wu et al. [46] in a solid-phase reduction procedure to replace the Mo atoms, transform Mo<sup>4+</sup> into Mo<sup>(4-x)+</sup>, and produce S vacancies. S vacancy concentration was adjusted from 7.8 to 20.3 at percent by adjusting Zn amount. Due to their high formation energy, which is greatly lowered by the presence of Zn dopants in their sample, DFT simulations have shown that such a high concentration of sulphur vacancies is unusual in pure MoS<sub>2</sub>. Edges and sulphur vacancies are preferred locations for Zn ion intercalation, according to DFT studies [47]. Intercalation of Zn ions may cause a phase change from 2H to 1T structure, much like alkaline ions do [48]. Since 1T-MoS<sub>2</sub> has a lower energy barrier against Zn intercalation, this phase transition is favoured for Zn intercalation [49]. Because MoS<sub>2</sub> is frequently employed as a cathode material in Zn-ion batteries, there have been several experimental researches on Zn intercalation. However, none of those studies examined the impacts from the standpoint of a single atom doping; rather, they all looked at the effects volumetrically. Zinc ions have a hard time intercalating/flowing out into/from the MoS<sub>2</sub> structure due to the relatively short interlayer spacing of MoS<sub>2</sub> in compared to Zn<sup>2+</sup>

ionic size. Instead, larger MoS<sub>2</sub> structures/composites offer more interstitial sites and have better interactions with Zn ions, which prevent Zn-ion batteries and capacitors from breathing and changing volume [50–52].

Promising HER catalytic performance of Zn-doped [53–56] and Zn intercalated [57] MoS<sub>2</sub> nanosheets with similar or improved long-term stability compared to pristine MoS<sub>2</sub> has been achieved due to increased electron density, higher electrical conductivity, reduced adsorption energy of hydrogen on sulphur atoms near the Zn dopants, as well as a large number of sulphur vacancies. Additionally, it has been discovered that Cd and Hg can adsorb on the surface of MoS<sub>2</sub> nanosheets, which has been employed to remove these undesirable metal ions from aqueous solutions [58-60].

## References:

1. V. Nicolosi, M. Chhowalla, M. G. Kanatzidis, M. S. Strano, J. N. Coleman, *Science* 2013, 340, 1226419; f) M. Chhowalla, H. S. Shin, G. Eda, L.-J. Li, K. P. Loh, H. Zhang, *Nat. Chem.* 2013, 5, 263–275.
2. Z. Zeng, Z. Yin, X. Huang, H. Li, Q. He, G. Lu, F. Boey, H. Zhang, *Angew. Chem. Int. Ed.* 2011, 50, 11093–11097; *Angew. Chem.* 2011, 123, 11289–11293.
3. J. N. Coleman, M. Lotya, A. O'Neill, S. D. Bergin, P. J. King, U. Khan, K. Young, A. Gaucher, S. De, R. J. Smith, I. V. Shvets, S. K. Arora, G. Stanton, H. Y. Kim, K. Lee, G. T. Kim, G. S. Duesberg, T. Hallam, J. J. Boland, J. J. Wang, J. F. Donegan, J. C. Grunlan, G. Moriarty, A. Shmeliov, R. J. Nicholls, J. M. Perkins, E. M. Grieveson, K. Theuvsen, D. W. McComb, P. D. Nellist, V. Nicolosi, *Science* 2011, 331, 568 – 571.
4. H. Matte, A. Gomathi, A. K. Manna, D. J. Late, R. Datta, S. K. Pati, C. N. R. Rao, *Angew. Chem. Int. Ed.* 2010, 49, 4059–4062; *Angew. Chem.* 2010, 122, 4153–4156.
5. P.-p. Wang, H. Sun, Y. Ji, W. Li, X. Wang, *Adv. Mater.* 2014, 26, 964–969; b) C. Altavilla, M. Sarno, P. Ciambelli, *Chem. Mater.* 2011, 23, 3879–3885.
6. E. Benavente, M. A. Santa Ana, F. Mendizbal, G. Gonzalez, *Coord. Chem. Rev.* 2002, 224, 87–109.
7. Eda, T. Fujita, H. Yamaguchi, D. Voiry, M. Chen, M. Chhowalla, *ACS Nano* 2012, 6, 7311–7317.
8. J. Zheng, H. Zhang, S. Dong, Y. Liu, C. Tai Nai, H. Suk Shin, H. Young Jeong, B. Liu, K. Ping Loh, *Nat. Commun.* 2014, 5, 2995.
9. S. S. Chou, Y.-K. Huang, J. Kim, B. Kaehr, B. M. Foley, P. Lu, C. Dykstra, P. E. Hopkins, C. J. Brinker, J. Huang, V. P. Dravid, *J. Am. Chem. Soc.* 2015, 137, 1742–1745.
10. L. Niu, K. Li, H. Zhen, Y.-S. Chui, W. Zhang, F. Yan, Z. Zheng, *Small* 2014, 10, 4651–4657.
11. J. Liu, Z. Zeng, X. Cao, G. Lu, L.-H. Wang, Q.-L. Fan, W. Huang, H. Zhang, *Small* 2012, 8, 3517–3522.
12. R. J. Smith, P. J. King, M. Lotya, C. Wirtz, U. Khan, S. De, A. O'Neill, G. S. Duesberg, J. C. Grunlan, G. Moriarty, J. Chen, J. Wang, A. I. Minett, V. Nicolosi, J. N. Coleman, *Adv. Mater.* 2011, 23, 3944–3948.



13. G. Guan, S. Zhang, S. Liu, Y. Cai, M. Low, C. P. Teng, I. Y. Phang, Y. Cheng, K. L. Duei, B. M. Srinivasan, Y. Zheng, Y.-W. Zhang, M.-Y. Han, *J. Am. Chem. Soc.* 2015, 137, 6152–6155.
14. A. Ciesielski, P. Samori, *Chem. Soc. Rev.* 2014, 43, 381–398.
15. Y. Hernandez, V. Nicolosi, M. Lotya, F. M. Blighe, Z. Sun, S. De, I. T. McGovern, B. Holland, M. Byrne, Y. K. Gun'Ko, J. J. Boland, P. Niraj, G. Duesberg, S. Krishnamurthy, R. Goodhue, J. Hutchison, V. Scardaci, A. C. Ferrari, J. N. Coleman, *Nat. Nanotechnol.* 2008, 3, 563–568.
16. R. J. Smith, P. J. King, M. Lotya, C. Wirtz, U. Khan, S. De, A. O'Neill, G. S. Duesberg, J. C. Grunlan, G. Moriarty, J. Chen, J. Wang, A. I. Minett, V. Nicolosi, J. N. Coleman, *Adv. Mater.* 2011, 23, 3944–3948.
17. Y. G. Yao, L. Tolentino, Z. Z. Yang, X. J. Song, W. Zhang, Y. S. Chen, C. P. Wong, *Adv. Funct. Mater.* 2013, 23, 3577–3583.
18. J.-Y. Wu, M.-N. Lin, L.-D. Wang, T. Zhang, *J. Nanomater.* 2014, 852735.
19. Y. Yao, Z. Lin, Z. Li, X. Song, K.-S. Moon, C.-p. Wong, *J. Mater. Chem.* 2012, 22, 13494–13499.
20. D. Van Thanh, C. C. Pan, C. W. Chu, K. H. Wei, *RSC Adv.* 2014, 4, 15586–15589.
21. N. Liu, P. Kim, J. H. Kim, J. H. Ye, S. Kim, C. J. Lee, *ACS Nano* 2014, 8, 6902–6910.
22. C. N. R. Rao, H. Matte, U. Maitra, *Angew. Chem. Int. Ed.* 2013, 52, 13162–13185; *Angew. Chem.* 2013, 125, 13400–13424.
23. P.-p. Wang, H. Sun, Y. Ji, W. Li, X. Wang, *Adv. Mater.* 2014, 26, 964–969.
24. B. L. Cushing, V. L. Kolesnichenko, C. J. O'Connor, *Chem. Rev.* 2004, 104, 3893–3946.
25. J. F. Xie, H. Zhang, S. Li, R. X. Wang, X. Sun, M. Zhou, J. F. Zhou, X. W. Lou, Y. Xie, *Adv. Mater.* 2013, 25, 5807–5813.
26. Y. Lu, X. Yao, J. Yin, G. Peng, P. Cui, X. Xu, *RSC Adv.* 2015, 5, 7938–7943.
27. C. Altavilla, M. Sarno, P. Ciambelli, *Chem. Mater.* 2011, 23, 3879–3885.
28. F. Bonaccorso, A. Lombardo, T. Hasan, Z. Sun, L. Colombo, A. C. Ferrari, *Mater. Today* 2012, 15, 564–589.
29. A. A. Green, M. C. Hersam, *Nano Lett.* 2009, 9, 4031–4036.
30. J. Kang, J.-W. T. Seo, D. Alducin, A. Ponce, M. J. Yacaman, M. C. Hersam, *Nat. Commun.* 2014, 5, 5478.

31. Zhao, X.; Zhang, H.; Yan, Y.; Cao, J.; Li, X.; Zhou, S.; Peng, Z.; Zeng, J. Engineering the electrical conductivity of lamellar silverdoped cobalt(II) selenide nanobelts for enhanced oxygen evolution. *Angew. Chem., Int. Ed.* 2017, 56, 328–332.
32. Balendhran, S.; Deng, J.; Ou, J. Z.; Walia, S.; Scott, J.; Tang, J.; Wang, K. L.; Field, M. R.; Russo, S.; Zhuiykov, S.; Strano, M. S.; Medhekar, N.; Sriram, S.; Bhaskaran, M.; Kalantar-Zadeh, K. Enhanced charge carrier mobility in two-dimensional high dielectric molybdenum oxide. *Adv. Mater.* 2013, 25, 109–114.
33. Du, X.; Huang, J.; Zhang, J.; Yan, Y.; Wu, C.; Hu, Y.; Yan, C.; Lei, T.; Chen, W.; Fan, C.; Xiong, J. Modulating electronic structures of inorganic nanomaterials for efficient electrocatalytic water splitting. *Angew. Chem., Int. Ed.* 2019, 58, 4484–4502.
34. Xie, J.; Yang, X.; Xie, Y. Defect engineering in two-dimensional electrocatalysts for hydrogen evolution. *Nanoscale* 2020, 12, 4283–4294.
35. Deng, J.; Li, H.; Wang, S.; Ding, D.; Chen, M.; Liu, C.; Tian, Z.; Novoselov, K. S.; Ma, C.; Deng, D.; Bao, X. Multiscale structural and electronic control of molybdenum disulfide foam for highly efficient hydrogen production. *Nat. Commun.* 2017, 8, 14430.
36. Xiong, Q.; Wang, Y.; Liu, P. F.; Zheng, L. R.; Wang, G.; Yang, H. G.; Wong, P. K.; Zhang, H.; Zhao, H. Cobalt covalent doping in MoS<sub>2</sub> to induce bifunctionality of overall water splitting. *Adv. Mater.* 2018, 30, 1801450–1801457.
37. Duan, H.; Wang, C.; Li, G.; Tan, H.; Hu, W.; Cai, L.; Liu, W.; Li, N.; Ji, Q.; Wang, Y.; Lu, Y.; Yan, W.; Hu, F.; Zhang, W.; Sun, Z.; Qi, Z.; Song, L.; Wei, S. Single-atom-layer catalysis in a MoS<sub>2</sub> monolayer activated by long-range ferromagnetism for the hydrogen evolution reaction: Beyond single-atom catalysis. *Angew. Chem., Int. Ed.* 2021, 60, 7251–7258.
38. Luo, R.; Luo, M.; Wang, Z.; Liu, P.; Song, S.; Wang, X.; Chen, M. The atomic origin of nickel-doping-induced catalytic enhancement in MoS<sub>2</sub> for electrochemical hydrogen production. *Nanoscale* 2019, 11, 7123–7128.
39. Li, Y.; Gu, Q.; Johannessen, B.; Zheng, Z.; Li, C.; Luo, Y.; Zhang, Z.; Zhang, Q.; Fan, H.; Luo, W.; Liu, B.; Dou, S.; Liu, H. Synergistic Pt doping and phase conversion engineering in twodimensional MoS<sub>2</sub> for efficient hydrogen evolution. *Nano Energy* 2021, 84, 105898–105906.
40. Xie, J.; Zhang, J.; Li, S.; Grote, F.; Zhang, X.; Zhang, H.; Wang, R.; Lei, Y.; Pan, B.; Xie, Y. Controllable disorder engineering in oxygen-incorporated MoS<sub>2</sub> ultrathin

- nanosheets for efficient hydrogen evolution. *J. Am. Chem. Soc.* 2013, 135, 17881–17889.
41. Liu, P.; Zhu, J.; Zhang, J.; Xi, P.; Tao, K.; Gao, D.; Xue, D. P dopants triggered new basal plane active sites and enlarged interlayer spacing in MoS<sub>2</sub> nanosheets toward electrocatalytic hydrogen evolution. *ACS Energy Lett.* 2017, 2, 745–752.
  42. Xiao, W.; Liu, P.; Zhang, J.; Song, W.; Feng, Y. P.; Gao, D.; Ding, J. Dual-functional N dopants in edges and basal plane of MoS<sub>2</sub> nanosheets toward efficient and durable hydrogen evolution. *Adv. Energy Mater.* 2017, 7, 1602086–1602096.
  43. Wang, H.; Xiao, X.; Liu, S.; Chiang, C. L.; Kuai, X.; Peng, C. K.; Lin, Y. C.; Meng, X.; Zhao, J.; Choi, J.; Lin, Y. G.; Lee, J. M.; Gao, L. Structural and electronic optimization of MoS<sub>2</sub> edges for hydrogen evolution. *J. Am. Chem. Soc.* 2019, 141, 18578–18584.
  44. Y. Nie, X. Zhang, Q. Zhang, Z. Liang, Q. Ma, X. Su, A novel high efficient electrochemiluminescence sensor based on reductive Cu(I) particles catalyzed Zn-doped MoS<sub>2</sub> QDs for HPV 16 DNA determination, *Biosens. Bioelectron.* 160 (2020)112217.
  45. E.Z. Xu, H.M. Liu, K. Park, Z. Li, Y. Losovyj, M. Starr, M. Werbianskyj, H.A. Fertig, S.X. Zhang, P-Type transition-metal doping of large-area MoS<sub>2</sub> thin films grown by chemical vapor deposition, *Nanoscale.* 9 (2017) 3576–3584.
  46. H. Li, C. Tsai, A.L. Koh, L. Cai, A.W. Contryman, A.H. Fragapane, J. Zhao, H.S. Han, H.C. Manoharan, F. Abild-Pedersen, J.K. Nørskov, X. Zheng, Activating and optimizing MoS<sub>2</sub> basal planes for hydrogen evolution through the formation of strained sulphur vacancies, *Nat. Mater.* 15 (2016) 48–53.
  47. W. Xu, C. Sun, K. Zhao, X. Cheng, S. Rawal, Y. Xu, Y. Wang, Defect engineering activating (Boosting) zinc storage capacity of MoS<sub>2</sub>, *Energy Storage Mater.* 16 (2019) 527–534.
  48. H. Liang, Z. Cao, F. Ming, W. Zhang, D.H. Anjum, Y. Cui, L. Cavallo, H.N. Alshareef, Aqueous Zinc-Ion Storage in MoS<sub>2</sub> by Tuning the Intercalation Energy, *Nano Lett.* 19 (2019) 3199–3206.
  49. J. Liu, P. Xu, J. Liang, H. Liu, W. Peng, Y. Li, F. Zhang, X. Fan, Boosting aqueous zinc-ion storage in MoS<sub>2</sub> via controllable phase, *Chem. Eng. J.* 389 (2020) 124405.

50. W.S.V. Lee, T. Xiong, X. Wang, J. Xue, Unraveling MoS<sub>2</sub> and Transition Metal Dichalcogenides as Functional Zinc-Ion Battery Cathode: A Perspective, *Small Methods*. 5 (2021) 2000815.
51. H. Li, Q. Yang, F. Mo, G. Liang, Z. Liu, Z. Tang, L. Ma, J. Liu, Z. Shi, C. Zhi, MoS<sub>2</sub> nanosheets with expanded interlayer spacing for rechargeable aqueous Zn-ion batteries, *Energy Storage Mater.* 19 (2019) 94–101.
52. M. Huang, Y. Mai, L. Zhao, X. Liang, Z. Fang, X. Jie, Tuning the kinetics of zinc ion in MoS<sub>2</sub> by polyaniline intercalation, *Electrochim. Acta*. 388 (2021) 138624.
53. P. Liu, J. Zhu, J. Zhang, K. Tao, D. Gao, P. Xi, Active basal plane catalytic activity and conductivity in Zn doped MoS<sub>2</sub> nanosheets for efficient hydrogen evolution, *Electrochim. Acta*. 260 (2018) 24–30.
54. Y. Shi, Y. Zhou, D.R. Yang, W.X. Xu, C. Wang, F. Bin Wang, J.J. Xu, X.H. Xia, H.Y. Chen, Energy Level Engineering of MoS<sub>2</sub> by Transition-Metal Doping for Accelerating Hydrogen Evolution Reaction, *J. Am. Chem. Soc.* 139 (2017) 15479–15485.
55. J. Xu, Z. Zhao, W. Wei, G. Chang, Z. Xie, W. Guo, D. Liu, D. Qu, H. Tang, J. Li, Tuning the intrinsic activity and electrochemical surface area of MoS<sub>2</sub> via tiny Zn doping: toward an efficient HER catalyst, *Chem. – A Eur. J.* 64 (2021) 15992-15999.
56. H. Qian, N. Huang, J. Zheng, Z. An, X. Yin, Y. Liu, W. Yang, Y. Chen, A ternary hybrid of Zn-doped MoS<sub>2</sub>-RGO for highly effective electrocatalytic hydrogen evolution, *J. Colloid Interface Sci.* 599 (2021) 100–108.
57. D.Ö. Özgür, G. Özkan, O. Atakol, H. Çelikkan, Facile Ion-Exchange Method for Zn Intercalated MoS<sub>2</sub> As an Efficient and Stable Catalyst toward Hydrogen Evaluation Reaction, *ACS Appl. Energy Mater.* 4 (2021) 2398–2407.
58. Q. Wang, L. Yang, F. Jia, Y. Li, S. Song, Removal of Cd (II) from water by using nanoscale molybdenum disulphide sheets as adsorbents, *J. Mol. Liq.* 263 (2018) 526–533.
59. C. Liu, S. Zeng, B. Yang, F. Jia, S. Song, Simultaneous removal of Hg<sup>2+</sup>, Pb<sup>2+</sup> and Cd<sup>2+</sup> from aqueous solutions on multifunctional MoS<sub>2</sub>, *J. Mol. Liq.* 296 (2019) 111987.
60. Z. Wang, J. Zhang, T. Wen, X. Liu, Y. Wang, H. Yang, J. Sun, J. Feng, S. Dong, J. Sun, *Sci. Total Environ.* 699 (2020) 134341.

# **CHAPTER 4**

## **INSTRUMENTS AND**

### **APPARATUS**

Major synthesis-related equipment and accessories are addressed in this chapter, along with the operation and working theory of several characterization techniques.

## 4.1 Crystal Structure Analyses

### 4.1.1 X-RAY Diffractometer

German physicist Wilhelm Roentgen discovered X-rays in 1895, giving them their name because of their then-unknown nature. These rays, which were invisible and moved in straight lines, had the same effects as regular light on the photographic plate. These rays exhibit greater penetrating strength than light as well. The precise nature of X-rays and the diffraction phenomena of X-rays by crystal atomic planes were adequately discovered in 1912. This finding illuminated the fact that X-rays are waves and opened up a fresh line of inquiry into the composition of matter. As follows are the categories of solid matter:

- **Amorphous:** The atoms are arranged in a random way similar to the disorder we find in a liquid. Glasses are amorphous materials.
- **Crystalline:** The atoms are arranged in a regular pattern, and one smallest volume element that by repetition in three dimensions describe the crystal. This smallest volume element is called a unit cell. The dimensions of the unit cell are described by three axes: a, b, c and the angles between them alpha ( $\alpha$ ), beta ( $\beta$ ), gamma ( $\gamma$ ). About 95% of all solids can be described as crystalline. X-rays are electromagnetic radiation of almost same nature as light but having shorter wavelength of 0.5 to 2.5 Å regions. X-rays occupy the region between gamma and ultraviolet rays in the entire spectrum.

X-rays are electromagnetic radiation of almost same nature as light but having shorter wavelength of 0.5 to 2.5 Å regions. X-rays occupy the region between gamma and ultraviolet rays in the entire spectrum.

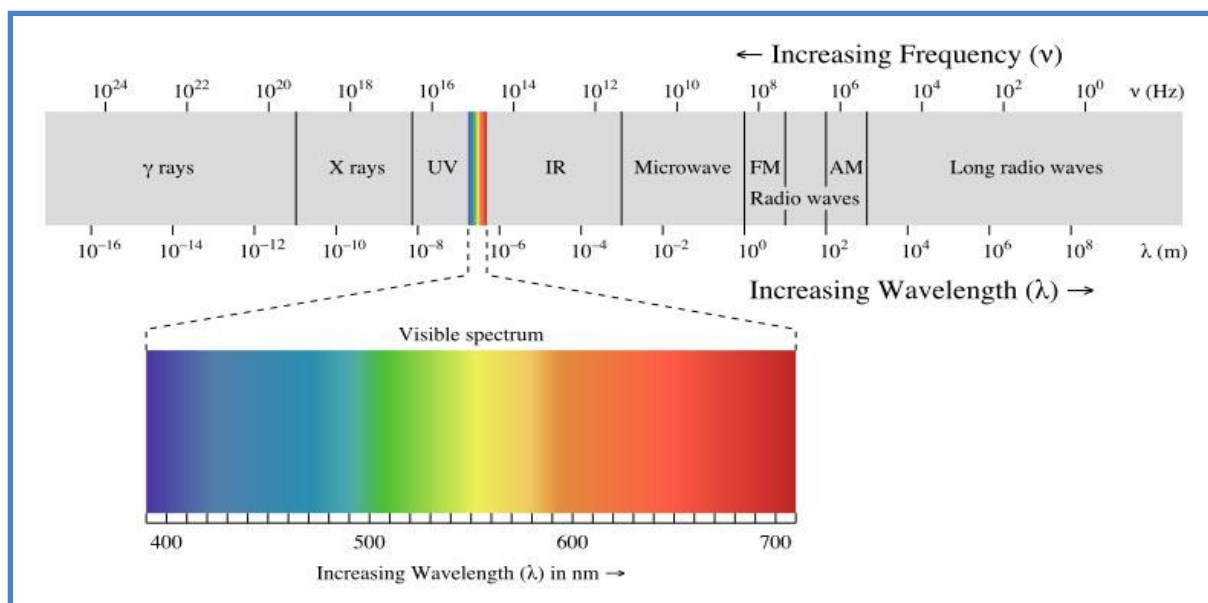


**Fig 4.1:** Illustration of electromagnetic spectrum

Diffraction is a scattering phenomenon in which a large number of atoms participate and act as scattering center. X-rays scattered by the atoms which are periodically arranged in the lattice, have definite phase relationship in between them. In some scattering direction, destructive interference takes place but in few directions, constructive interference occurs and forms the diffracted beam. *"A diffracted beam may be defined as a beam composed of a large number of scattered rays mutually reinforcing one another."*

- **Working Principle**

In XRD, a collimated beam of X-rays is incident on a specimen and is diffracted by the crystalline phases in the specimen. Using Bragg equation for first order diffraction, lattice spacing may be found from the diffraction angles. **Bragg's law** is the basic law which governs the X-ray diffraction technique of structural analysis. In **Bragg's law**, the interaction between X-rays and the electrons of the atoms is described as a process of reflection of X-rays by the atomic planes. When monochromatic X-rays incident on the atoms in the crystal lattice, atomic planes allow a part of X-rays to pass through and reflect the other part, there exist a path difference in between the reflected rays from plane 1 and plane 2. These rays will reinforce each other, only when this path difference is equal to an integral multiple of the wavelength.

The **Bragg's law** can be written as:  $2d\sin\theta = n\lambda$

Where **n** is an integer and  $\lambda$  is the wavelength of the X-rays used,  $\theta$  is Bragg angle and **d** is the interplanar spacing.

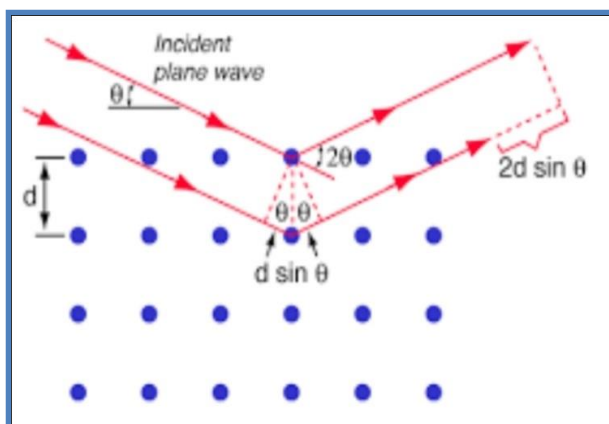


**Fig 4.2:** Illustration of Bragg's law

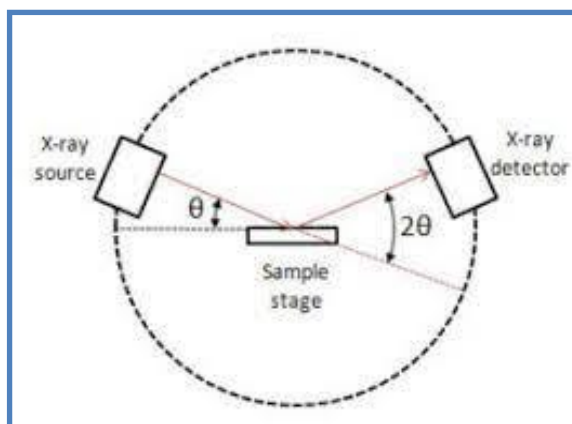


**Fig 4.3:** Schematic of X-ray Diffractometer

- **Applications:**

- Measurement of interplanar spacing between two atomic planes.
- Determination of orientation of single crystal.
- Determination of crystal structure for an unknown material.
- Measurement of particle size, phase and internal stress etc.

A RigakuUltima III X-ray Diffractometer was used for recording the diffraction pattern of the samples in  $\theta$ - $2\theta$  configuration with Cu K $\alpha$  radiation ( $\lambda=1.5404 \text{ \AA}$ ) operated at 40KV voltage and 30mA current. A photographic image of X-ray diffractometer is shown in **Fig 4.4**



**Fig 4.4:** Experimental set up of X-Ray Diffractometer



## 4.2 Optical Property Analysis

### 4.2.1 Ultraviolet Visible Spectrophotometer

UV spectroscopy is type of absorption spectroscopy in which light of ultraviolet region (200-400 nm) is absorbed by the molecule. Absorption of the ultraviolet radiations results in the excitation of the electrons from the ground state to higher energy state. The energy of the ultraviolet radiation that are absorbed is equal to the energy difference between the ground state and higher energy states ( $\Delta E = h\nu$ ).

There are two laws that govern the absorption of light by a medium, known as **Lambert's law** and **Beer's law**. Lambert's law predicts the absorbance is directly proportional to the thickness/path length of the medium. Beer's law explains the effect of concentration of colored components in solution on light transmission or absorption. By combining of these two laws, we get **Lambert-Beer's law** which is as follows:

$$\log (I_0/I_t) = A = \alpha cd$$

Where,  $A$  denotes absorbance,  $\alpha$  denotes molar absorptivity,  $c$  is concentration and  $d$  is path length. From the **Lambert-Beer's law** it is clear that greater the number of molecules capable of absorbing light of a given wavelength, the greater the extent of light absorption. That is the basic principle of UV spectroscopy.

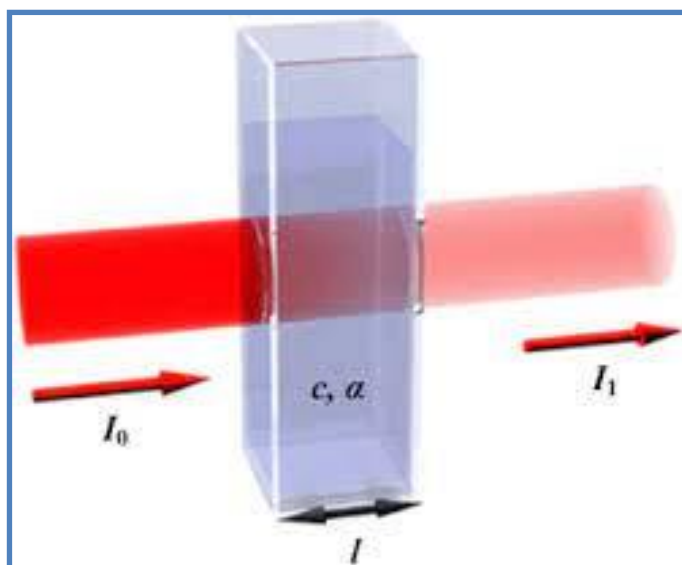


Fig 4.5: Lambert-Beer's law

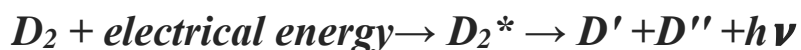
- **Configuration of instrument**

A spectrophotometer is an instrument which measures the transmittance or absorbance of a sample as a function of the wavelength of electromagnetic radiation. The main components of a spectrophotometer are:

1. Source
2. Monochromator
3. Sample container
4. Detectors

### **1. Source**

The ideal light source would yield a constant intensity over all wavelengths with low noise and long-term stability. Unfortunately, however, such a source does not exist. Two sources are commonly used in UV-visible spectrophotometers. The electrical excitation of deuterium or hydrogen at low pressure produces a continuous UV spectrum. The mechanism for this involves formation of an excited molecular species, which breaks up to give two atomic species and an ultraviolet photon. This can be shown as;



Deuterium lamps emit radiation in the range 160-375 nm. Quartz windows must be used in these lamps, and quartz cuvettes must be used, because glass absorbs radiation of wavelengths less than 350 nm. The tungsten filament lamp is commonly employed as a source of visible light. This type of lamp is used in the wavelength range of 350-2500 nm.

### **2. Monochromator**

All Monochromator contain certain components like *entrance slit, collimating mirrors, dispersing device (usually a prism or a grating), focusing mirrors and exit slit*. Polychromatic radiation (radiation of more than one wavelength) enters the Monochromator through the entrance slit. The beam is collimated, and then strikes the dispersing element at an angle. The Beam is split into its component wavelengths by the grating or prism. By moving the dispersing element or the exit slit, radiation of only a particular wavelength leaves the Monochromator through the exit slit.

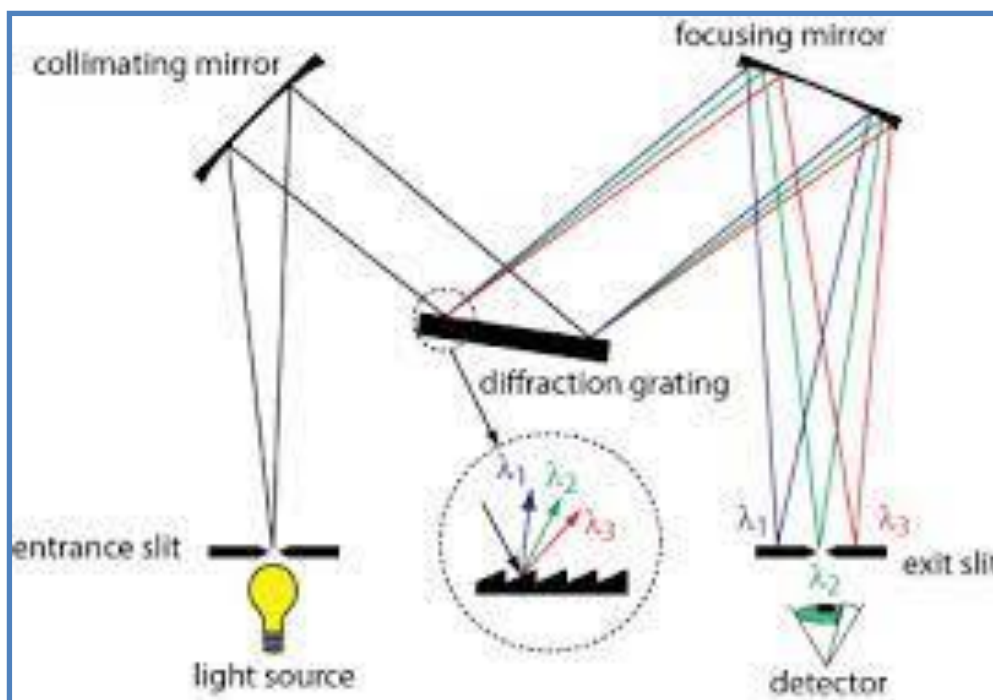


**Fig 4.6:** Construction of Monochromator

### 3. Sample container

The containers (**cuvettes**) for the sample and reference solution must be transparent to the radiation which will pass through them. Quartz or fused silica cuvettes are required for spectroscopy in the UV region. These cells are also transparent in the visible region.

### 4. Detector

A detector converts a light signal into an electrical signal. The photomultiplier tube is commonly used detector in UV-Vis spectroscopy. It consists of **photoemissive cathode** (a cathode which emits electrons when struck by photons of radiation), several **dynodes** (which emit several electrons for each electron striking them) and an **anode**. Another type of detector is linear photodiode array which is an example of a **multichannel photon detector**. These detectors are capable of measuring all elements of a beam of dispersed radiation simultaneously. Photodiode arrays are complex devices but, because they are solid state, have high reliability.

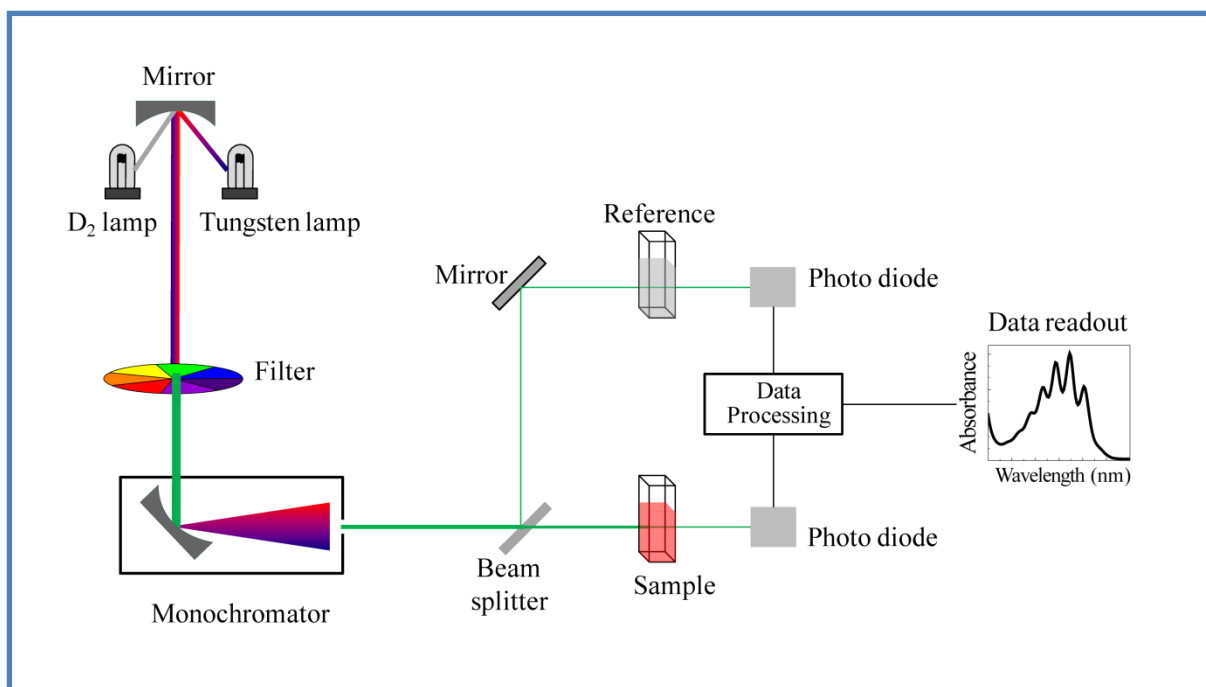


**Fig 4.7:** Configuration of Uv-Visible spectrophotometer



**Fig 4.8:** Experimental set up of UV-VIS-NIS (SHIMADZU UV-3600) Spectrophotometer

### 4.2.2 Raman Analysis

Raman scattering was first observed by Dr. C.V. Raman in 1928 and was used to investigate the vibrational states of many molecules.

- **Raman system**

A typical Raman system consists of the following basic components:

- 1) Excitation source, usually a laser
- 2) Optics for sample illumination
- 3) Double or triple Monochromator
- 4) Signal processing system

A sample is mounted on the sample chamber and laser light is focused on it with the help of a lens. The scattered light is collected using another lens and is focused at the entrance slit of the Monochromator. The Monochromator effectively rejects stray light and serves as a dispersing element for incoming radiation. The light leaving the exits slit of the Monochromator is collected and focused on the surface of a detector. The optical signal is converted to an electrical signal within the detector and further manipulated using detector electronics. Such a signal is stored in computer memory for each predetermined frequency interval. In a conventional Raman system using a photomultiplier tube (PMT) detector, light intensity at various frequencies is measured by scanning the Monochromator. A plot of signal intensity against wavenumber constitutes it Raman spectrum.

- **Principle**

When is sample is irradiated with an intense monochromatic light source (usually a laser), most of the radiation is scattered by the sample and the same wavelength as that of the incoming laser radiation in a process known as Rayleigh scattering. However, a small proportion of the incoming light approximately one photon out of a million is scattered at a wavelength that is shifted from the original laser wavelength. Laser light excites the sample, this light is a scatters in all directions. Some of this scattered light directed to the detector, which records the Raman spectrum. This spectrum shows light at the original laser (Rayleigh) frequency and the Raman spectral features unique to the sample.

The same transitions between molecular vibrational states (M) and (M\*) in the infrared absorption can also result in Raman scattering. A key difference between the Raman and infrared processes is that, in the former process, the photons involved are not absorbed or emitted but rather shifted in frequency by an amount corresponding to the energy of the particular vibrational transition. In the Stokes process, which is the parallel of absorption, the scattered photons are shifted to lower frequencies as the molecules abstract energy from the exciting photons; in the anti-Stokes process, which is parallel to emission, the scattered photons are shifted to higher frequencies as they pick up the energy released by the molecules in the course of transitions to the ground state.

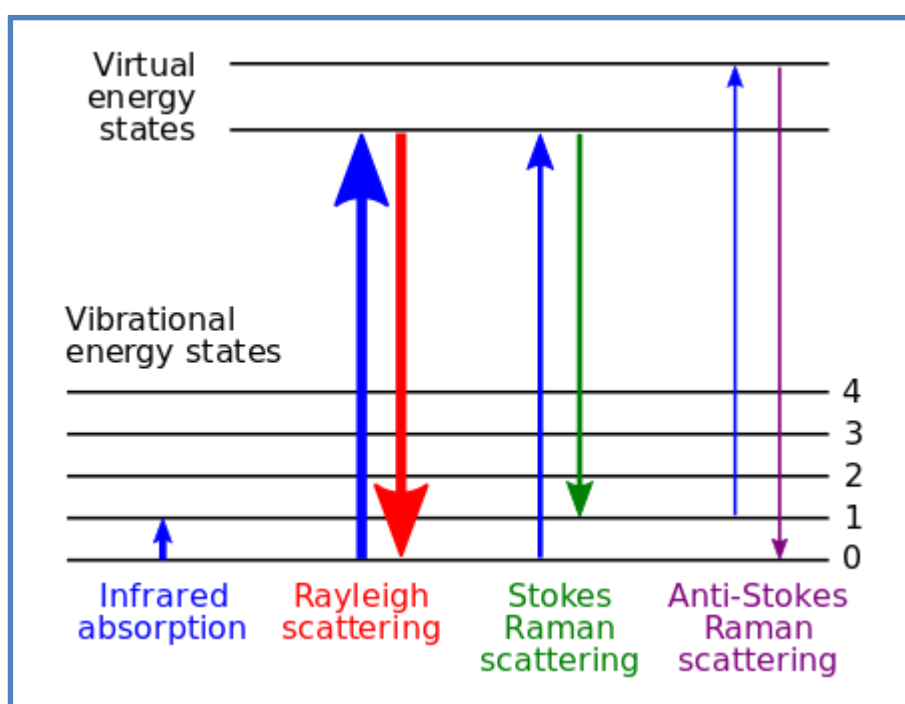


**Fig. 4.9:** Different types of scattering

Relaxation from the virtual state occurs almost instantaneously and is predominantly to the initial ground state. This process results in Rayleigh scatter, which is scattered light of the same wavelength as the excitation laser. Relaxation to the first excited vibrational level results in a Stokes-Raman shift. Stokes-Raman shift scattered light is of lower energy (longer wavelength) than that of the laser light. In addition, most systems have at least a small population of molecules that are initially in an excited vibrational state. When the Raman process initiates from the excited vibrational level, relaxation to the ground state is possible, producing scatter of higher energy (shorter wavelength) than that of the laser light. This type

of scatter is called anti-Stokes Raman scatter. Two molecules can give exactly the same Raman spectrum, and the intensity of the scattered light is proportional to the amount of material present. Thus Raman provides both qualitative and quantitative information about the sample. The Raman spectra carried out by WITEC alpha 300R-RAMAN spectroscopy.

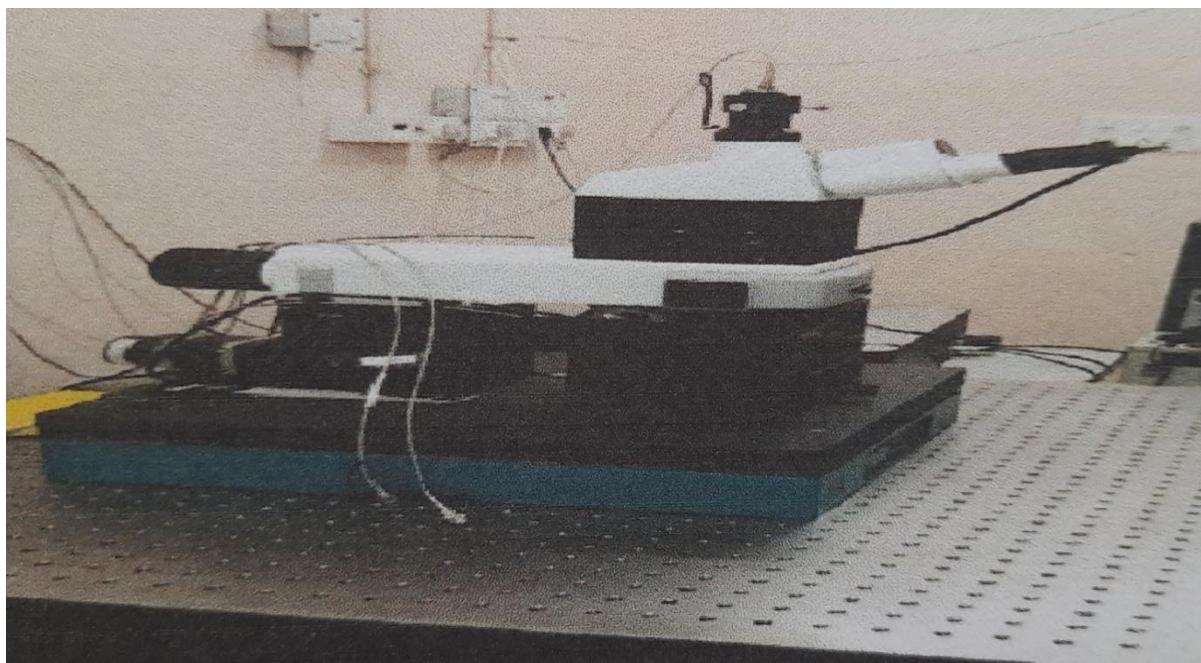


**Fig. 4.10:** Raman Analysis (WITEC) Setup

### 4.3 Morphological analysis

#### 4.3.1 Field Emission Scanning Electron Microscope (FESEM)

The word *microscope* is derived from the Greek *micros* (small) and *skopeo* (look at). From the discovery of science there has been an interest in being able to look at smaller and smaller details of the world around us. Our human eye provides the extreme limitation in microscopy. It has a resolution peye of  $\sim 0.1$  mm which is equivalent to the diameter of a human hair. This means that two small objects placed about 20 cm from the eye can be viewed as distinct when they are  $\sim 0.1$  mm apart. The limitation arises from the intrinsic magnification power of human eye and the separation of the sensing elements on the retina. And optical microscope has a resolution Gama popt and improvement of popt than that of the unaided eye can be done in a way which is limited by the wavelength of the light used to illuminate the object. For visible light, this corresponds to popt  $\sim 0.2$   $\mu\text{m}$ . That's why below  $0.2$   $\mu\text{m}$ , we cannot visualize objects through optical microscope. A FESEM is an electron microscope which uses electron beam liberated by field emission source instead of light.



Electrons will not travel far through air and electron microscopes are usually vacuum based instruments. Image formation in the SEM depends on the signals produced from the electron beam and specimen interactions. These interactions can be classified into two major categories: *elastic interactions and inelastic interactions*. Elastic scattering results from the deflection of the incident electron by the atomic nucleus or outer shell electrons of the specimen. This kind of interaction is categorized by very small amount of energy loss during the collision and by a wide angle directional change of the scattered electron. Incident electrons that are elastically scattered through an angle of more than 90 degree are called *backscattered electrons (BSE)*, and produce a useful signal for imaging the sample. Inelastic scattering occurs through a variety of interactions between the incident electrons and the electrons and atoms of the sample and results in the primary beam electron transferring considerable amount of energy to that atom. The amount of energy loss depends on whether the specimen electrons are excited singly or collectively and on the binding energy of the electron to the atom. The most widely used signal produced by the interaction of the primary electron beam with the specimen is the *secondary electron emission* signal. When the primary beam strikes the sample surface causing the ionization of specimen atoms, loosely bound electrons may be emitted and these are referred to as secondary electrons. As they have low energy, typically an average of around 3-5 eV, they can only escape from a region within a few nanometers of the material surface. These can be used to give information about the surface topography, morphology of the sample with good resolution. In addition to these signals, a number of other signals are produced when an electron beam strikes a sample, including the emission of *continuous X-rays, characteristic X-rays, Auger electrons and cathodeluminescence*.

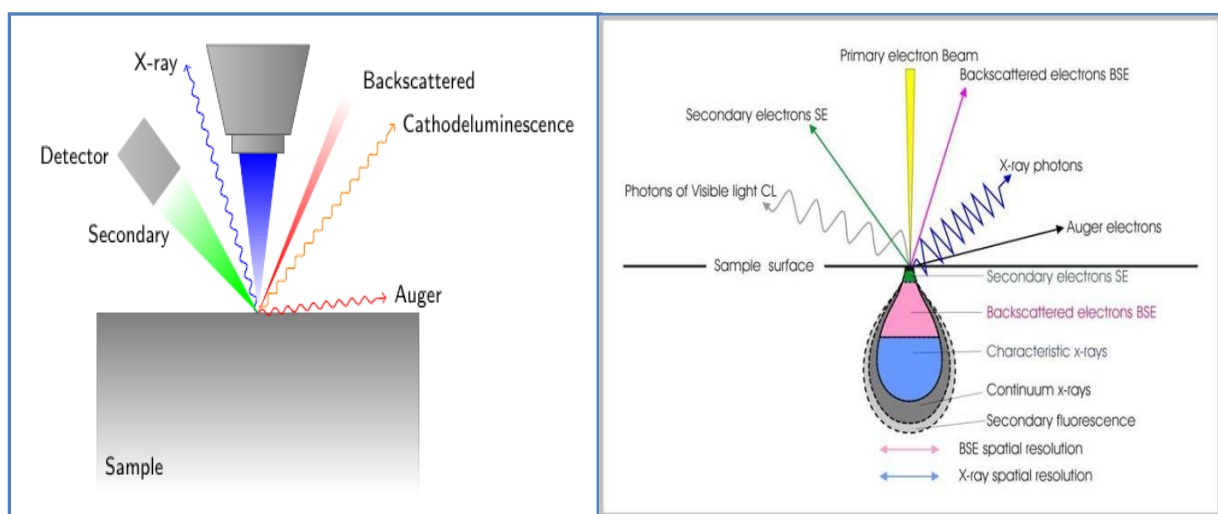


**Fig. 4.11:** Interaction of electron beam with matter



- **Configuration of FESEM**

**Fig. 4.11** shows the total components of field emission scanning electron microscope in details. It consists of electron gun to generate electron beam, electromagnetic lenses and aperture to focus the electron beam, detector, and vacuum system.

- **Electron Gun**

The electron gun produces a stable electron beam with high current, small spot size, adjustable energy and small energy dispersion. The first generation SEM systems generally used thermionic emission sources like tungsten "hairpin" ( $\Phi = 4.5\text{eV}$ ) or lanthanum hexaboride ( $\text{LaB}_6$ ) ( $\Phi = 2.4\text{eV}$ ) cathodes, but for the modern SEMs, the trend is to use field emission sources, which provide enhanced current and lower energy dispersion. Emitter lifetime is another important issue for selection of electron sources. The most widely used electron gun is composed of three parts: a V-shaped hairpin tungsten filament (the cathode), a Wehnelt cylinder and an anode, as shown in **Fig. 4.12**.

Thermionic sources required a high temperature to overcome the work function of the metal so that the electrons can escape from the cathode. Though they are inexpensive and the requirement of vacuum is relatively low but there are certain disadvantages, such as short lifetime, low brightness, and large energy spread which restrict their applications. For modern electron microscopes, field emission guns (FEG) are a good alternative for thermionic electron guns. In the FEG, a single crystal tungsten wire with very sharp tip is used as the electron source. In this system, a strong electric field forms on the finely oriented tip and the electrons are drawn toward the anodes forms concentrated electron beam.

- **Electron Lenses**

Electron beam can be focused by electrostatic or magnetic field. But electron beam controlled by magnetic field has smaller aberration, so only magnetic field is employed in SEM system. Coils of wire, known as "electromagnets" are used to produce magnetic field and the trajectories of the electrons can be adjusted by the current applied on these coils.

- **Condenser lens**

The electron beam will diverge after passing through the anode plate from the emission source. By using the condenser lens, the electron beam is converged and collimated into a relatively parallel stream. A magnetic lens generally consists of two rotationally symmetric iron pole pieces in which there is a copper winding which provides magnetic field. There is a hole in the centre of pole pieces that allows the electron beam to pass through. A lens-gap separates the two pole pieces, at which the magnetic field focuses the electron beam. The position of the focal point can be controlled by adjusting the condenser lens current.

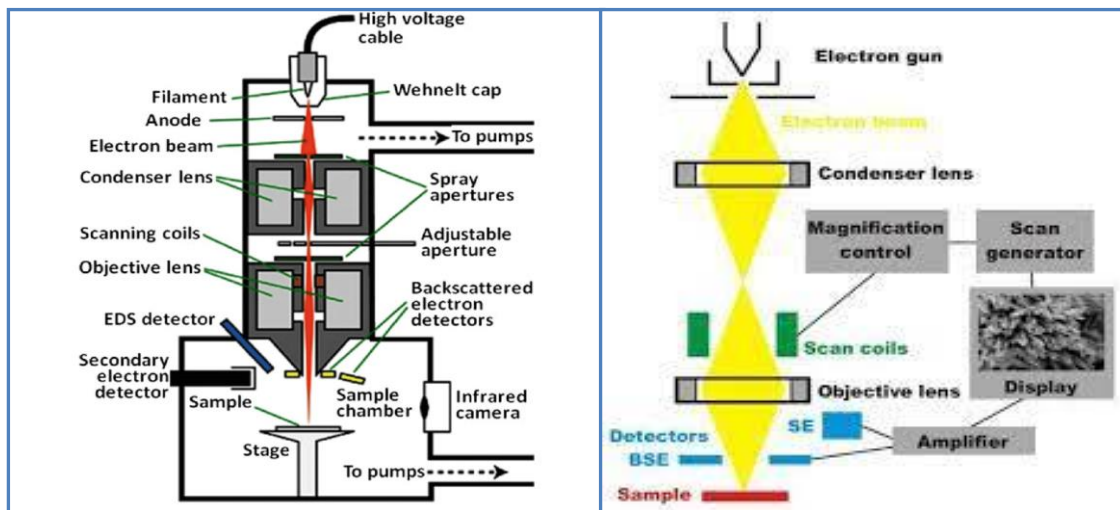


**Fig. 4.12:** Configuration of FESEM and its different components

- **Scan coils**

The scan coils deflect the electron beam over the object according to zigzag pattern. The formation of the image on the monitor occurs in synchrony with this scan movement. The scan velocity determines the refreshing rate on the screen and the amount of noise in the image. Scan coils often consist of upper and lower coils, which prevent the formation of a circular shadow at low magnification.

- **Objective lens**

The objective or "probeforming" lens is located at the base of electron column just above sample. The Beam is again divergent after passing through the apertures below the condenser lens and must be convergent again. The objective lens focuses the electron beam onto the sample and controls final size and position.

- **Sample preparation**

As we mentioned earlier that FESEM is vacuum based instrument, so sample must be vacuum tolerant. In addition to that, strong radiation by electrons can damage or destroy a sample through heating or other effects. Even in quite good vacuum ( $10^{-8}$  mbar), samples can become coated with gold/platinum in the microscope to retain the true surface details. Some samples, those are insulating in nature, are charged up under the electron beam and repel the incoming electron beam. This degrades the resolution and usually required some prevention technique such as coating the sample with the sample with a conducting layer.



**Fig. 4.13:** FESEM (Hitachi S-4800) set up

## **4.4 Surface Analysis**

### **4.4.1 X-Ray Photoelectron Spectroscopy**

X-Ray Photoelectron Spectroscopy is one of the most powerful surface analytical techniques capable to provide accurate qualitative elemental analysis (for all elements except hydrogen and helium), quantitative composition and determination of chemical state such as binding and oxidation can also be done. The information should be originated within ~10 nm from the outer surface.

- **Principles of XPS**

XPS is based on the photoelectric effect which is discovered by Hertz in 1887. In this case, electron emission from the surface is resulted due to the interaction of an x-ray photon of sufficient energy with the solid surface. The applied x-ray of 1-15 KeV energy is capable to induce electrons not only from the outer shells but also from the core levels of all elements of periodic table. The governing equation of this phenomenon is as follows:

$$h\nu = E_b + E_{kin} + W_f$$

Where,  $E_b$  is binding energy,  $E_{kin}$  is kinetic energy of photoelectron,  $W_f$  is work function of the instrument.

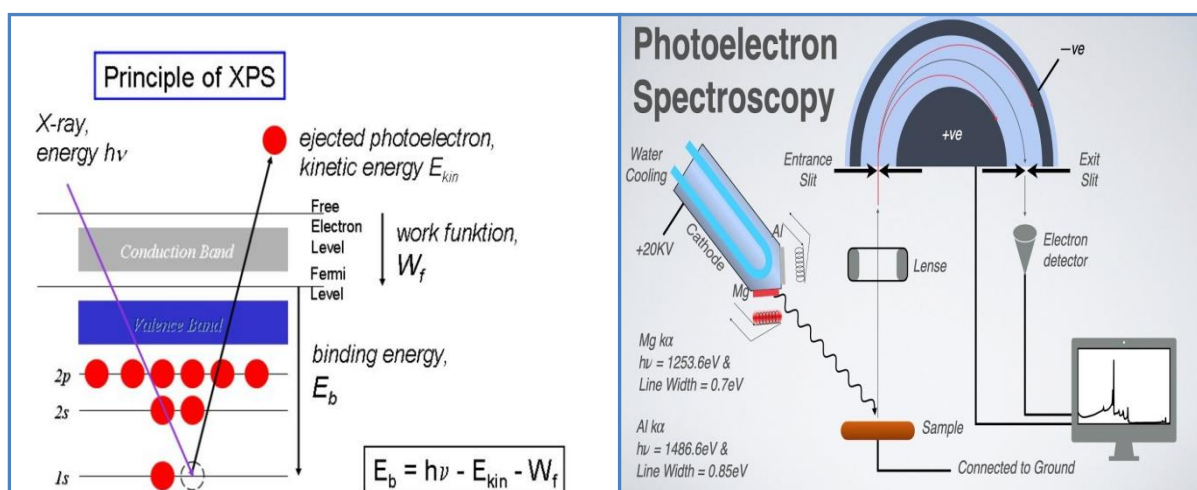


**Fig. 4.14:** Basic principles and constructions of XPS

- **Configuration of XPS instrument**

The experimental set up contains mainly the following parts: (i) an X-ray source for XPS, (ii) an electron energy analyzer, combined with a detection system, (iii) a sample stage, all contained within a vacuum chamber. As for most techniques, the system is operated and controlled by a computer, usually provided a software allowing mathematical treatment as shown in **Fig. 4.14**.

- **X-ray source**

Since XPS is concerned with the analysis of core electrons from a solid surface, sources used in XPS must be able to produce photons of a sufficient energy to access a suitable number of core electron levels. Photons of this energy lie within the X-ray region of the electromagnetic spectrum. As a result, these are otherwise referred to as X-rays. X-ray tube produce X-rays by directing a sufficiently energetic electron beam at some metallic solid. This metallic object is referred to as the X-ray anode, with the electron source being the cathode. Although any solid can in principle be used as an X-ray anode, Al has become that most commonly used in XPS due to the relatively high energy and intensity of Al-K $\alpha$  X-rays, the minimal energy spread of Al-K $\alpha$  X-rays and the fact that Al is an effective heat conductor.

- **Electron energy analyzer**

Since information in XPS is derived from the  $E_{\text{kin}}$  of the electron emissions, effective analysis requires energy filter that exhibits both a high-energy resolution and a high transmission. The former allows for the separation of closely spaced peaks, thereby optimizing speciation identification capabilities, while the latter allows for sensitivity to be maximized. The two primary energy filter configuration used in XPS named *Cylindrical Mirror Analyzer (CMA)*, *Concentric Hemispherical Analyzer (CHA)*.

- **Detector**

In XPS, it is not only important to measure the energy of the electron emissions but also the number of electrons produced. XPS spectra is plotted in units of energy versus intensity, with the energy defined by the energy analyzer used and the intensity defined by the number of electrons recorded by the detector. To obtain the best possible sensitivity, the detector must be capable of recording individual electrons, that is, operating in pulse counting mode. This signal is recorded in units of current (A), which are then represented in units of counts per second.

- **Sample stage**

The mounting of the samples on the sample holder should be done in such a way that electrical conduction is guaranteed. This is achieved by using metallic clips or bolt-down assemblies. Alternatively a metal loaded tape may also be used. In the case of powders, the particles can be pressed into an indium foil or carbon tape.

- **Vacuum requirement**

As XPS is a surface sensitive method, impurities can play a major role in the observed spectra. The criterion is that a good vacuum is needed to maintain the integrity of the surface. In general,  $10^{-5}$ Torr is sufficient to allow the Photoelectron to reach the detector without suffering collisions with other gas molecules. On the other hand,  $10^{-9}$ Torr or lower is required to keep an active surface clean for more than several minutes. So,  $10^{-8}$  -  $10^{-9}$ Torr provides a reasonable pressure range for XPS measurement. Sample analysis was performed on the SPECS with hemispherical energy analyzer (HAS 3500). Photoelectrons were excited using the monochromatic Mg K $\alpha$  X-ray (1253.6eV) or Al K $\alpha$  X-ray (1486.6eV) was used as the excitation source operated at 10 kV and with an anode current 17 mA.

The photograph of the X-ray Photoelectron Spectroscopy is shown in the **Fig.4.15**.



**Fig. 4.15:** Experimental set up of XPS

## **4.5 Electrochemical property analysis**

### **4.5.1 Cyclic Voltammetry**

Cyclic voltammetry is the most widely used technique for acquiring qualitative information about electrochemical reactions. It offers a rapid location of redox potentials of the electroactive species.



- **Principle**

Electron Transfer and Energy levels, the key to driving an electrode reaction is the application of a voltage. If we consider the units of volts  $V = \text{Joule/Coulomb}$ , we can see that a volt is simply the energy required to move charge. Application of a voltage to an electrode therefore supplies electrical energy. Since electrons possess charge, an applied voltage can alter the "energy" of the electrons within a metal electrode. The behavior of electrons in a metal can be partly understood by considering the Fermi level. Metals are comprised of closely packed atoms which have strong overlap between one another. A piece of metal therefore does not possess individual well defined electron energy levels that would be found in a single atom of the same material. Instead of continuum of levels are created with the available electrons filling the states from the bottom upwards. The Fermi level corresponds to the energy at which the top "electrons" sit.



**Fig. 4.16:** Autolab PGSTAT (M204) potentiostat/galvanostat Setup

# **CHAPTER 5**

## **Layer separation of 2H-MoS<sub>2</sub> without metal intercalation**



## 5.1 Introduction

In recent years, two-dimensional (2D) nanomaterial research has become a key area of nanoscience [1-4]. Other 2D materials being explored right now, besides graphene [5], include layered transition metal oxides ( $\text{MnO}_2$  and  $\text{TiTaO}_5$ ), transition metal dichalcogenides (TMDs), such as  $\text{MoS}_2$  and  $\text{WSe}_2$ , and a number of other fascinating structures, such as GaS, germanane, and  $\text{Bi}_2\text{Te}_3$  [6]. There are numerous variations of these materials, including metals, semiconductors, insulators, and superconductors [7]. Intriguing features like thickness-dependent bandgaps and catalytic activity are also present in them. They are useful for both fundamental research and practical applications in a range of domains, including optoelectronics, electrochemistry, and medicine, as a result of these qualities.

The majority of 2D materials are generated through the exfoliation of stacked crystals, despite the fact that they can be made directly [8]. This has long been achievable thanks to mechanical exfoliation, which yields samples of incredibly high quality but with very low throughput [9–11]. When larger production rates are required, chemical techniques [12–15], often based on ion intercalation, have been used to exfoliate multilayer crystals in liquids. Despite the fact that these methods generate a large number of monolayers, they are time-consuming and require harsh chemical processes that must be carried out in an inert environment.

Recently, liquid phase exfoliation (LPE), a considerably simpler method, has been published [16-27]. In this method, multilayer crystals are sonicated or sheared [27] in a variety of solvents, surfactant, or polymer solution solutions. Exfoliation of the layered crystal results in the formation of many 2D nanosheets, which are stabilised by liquid interaction. The resulting dispersions are easily converted into films, coatings, or composites, resulting in systems that are ideal for use in a number of industries, such as batteries [28, 29], photodetectors [30], and reinforced materials [31]. This technique has been used to make exfoliated dispersions of graphene, BN, TMDs like  $\text{MoS}_2$  and  $\text{WS}_2$ , transition metal dichalcogenides like  $\text{MnO}_2$  and  $\text{MoO}_3$ , as well as more odd structures like  $\text{Ti}_3\text{C}_2\text{F}_2$  nanosheets [34] and functionalized-layered double hydroxides [35]. In fact, we expect that this strategy will function for any layered molecule whose van der Waals interactions are mostly responsible for the bonding between the layers.

Despite being a versatile and useful strategy, LPE has numerous noticeable flaws. It is challenging to characterise optically dispersed nanosheets because of the scattering background, which is highly influenced by the size of the dispersed nanosheets. Because of this, it is difficult to simply measure concentration because it is uncertain how to estimate an inherent extinction coefficient.

Here, in this work, we have used probe sonication method to separate different layers of 2H-MoS<sub>2</sub> nanosheets. We have also used Tannic acid during the process because it plays two crucial roles here:

First, it acts as a surfactant. As we know, when two layers are present, they undergo restacking, that is the common features of 2D-materials. So, here, in presence of Tannic acid, the restacking probability is highly reduced. It cannot allow restacking and hence acts as surfactant.

Second, it can enhance the activity of the edge sulfur atoms. The edge sulfur atom of MoS<sub>2</sub> can easily abstract from H<sup>+</sup> ion. During the probe sonication i.e. in the presence of high ultrasonication method or high vibration, some layers, they are separated with each other and the edge sulfur atom which can react with H<sup>+</sup> ion to form H<sub>2</sub>S. Hence, we can activate the edge sulfur atom in the present layer dependent MoS<sub>2</sub> that can be employed in different electrochemistry or different catalytic applications.

Here, we discuss these concerns. We demonstrate size-selection techniques that yield fractions with optical extinction spectra that systematically vary with the size and thickness of nanosheets. By combining spectroscopic analysis with statistical microscopic research, we establish quantitative relationships between spectral properties and nanosheet sizes. An extinction spectrum can be used to calculate the concentration, length, and thickness of the nanosheet by quantifying these effects. The ability to modify size and thickness, for example, facilitates the development of dispersions rich in monolayers. Critically, we find that this idea holds true for several 2D materials.

## **5.2 Experimental section**

### **5.2.1 Sample preparation**

#### **5.2.1.1 Exfoliation/synthesis of 2H-MoS<sub>2</sub> nanosheet**

The 2H-MoS<sub>2</sub> nanosheets utilised throughout this work was synthesized via a surfactant based liquid exfoliation, sonication and centrifugation methodology. The Schematic is shown in the **figure 5.1**.

- Liquid exfoliation was performed by adding bulk-MoS<sub>2</sub> powder (concentration 1 mg/ml) in the solution of 50-50 i.e., 1:1 ml Isopropyl alcohol (IPA) and water (H<sub>2</sub>O) respectively contained within a 100 ml beaker.
- Next, Tannic acid (concentration 0.1/ml) is added into this solution.
- This dispersion was then sonicated using probe sonicator (PKS 750 FM) (max power rating 15000 watts) for 3 hours and 55% amplitude. Then, the mixture is allowed to settle.
- The three layers have been observed. The top layer (the yellow part) is basically the unreacted tannic acid, the middle layer (the green part) is the 2H-nanosheet and the bottom part (the black part) is the unreacted MoS<sub>2</sub> bulk particle due to agglomeration.
- The corresponding supernatant i.e., the yellow part was discarded.
- Again, the re-agitated sediment i.e., the green and black part underwent sonication using probe sonicator (PKS-750FM, max. power rating-15000 watt) for a further 1 hour and 55% amplitude.
- Upon completion of the sonication treatment, the solution was separated into another centrifuge tube and was centrifuged at 2000 rpm for 10 min.
- Finally, the light green part is extracted which is the required 2H-MoS<sub>2</sub> nanosheet.

#### **5.2.1.2 Preparation of layer separation of 2H-MoS<sub>2</sub> nanosheet**

- Another centrifuge tube is taken which contains Water and IPA mixture at the bottom, then in the middle part, the obtained 2H-MoS<sub>2</sub> nanosheet is taken and at the top part the IPA is there (due to the weight difference between the water and IPA).

- Next, this solution was centrifuged at 2000 rpm for 10 min.
- After the centrifugation, different layers are obtained which can be designated as S1, S2, S3, S4, S5, S6, S7 and S8 respectively.

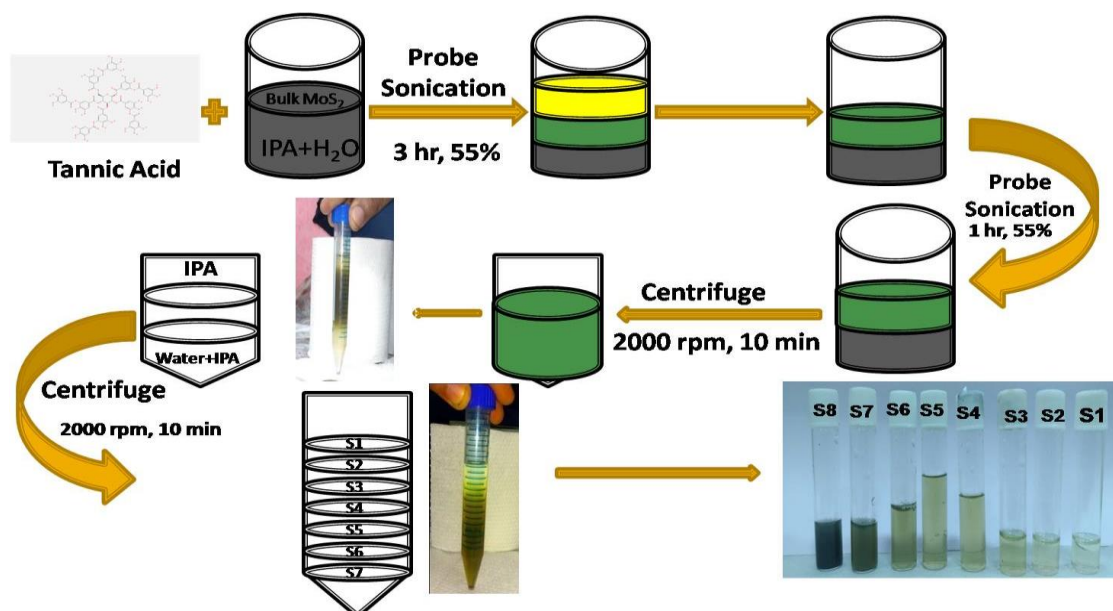


**Fig.5.1:** Schematic of preparation of layer separation of 2H-MoS<sub>2</sub> nanosheet

### 5.2.2 Characterizations

- The phase purity and crystal structure of the different layers of as synthesized MoS<sub>2</sub> nanosheet material was characterized by X-Ray diffraction (XRD, D8 Advance ECO, Cu-K $\alpha$  radiation, ( $\lambda=1.54\text{\AA}$ )).
- The chemical structures of different layers of MoS<sub>2</sub> nanosheet were analysed by Raman spectroscopy by confocal raman spectrometer (alpha 300, Witec, Germany, Laser Source of wave-length 532 nm).
- The surface analysis of various layers of MoS<sub>2</sub> nanosheets were done by using X-Ray Photoelectron Spectroscopy.
- The morphology analysis of the prepared samples was done by High Resolution Transmission Electron Microscopy (HRTEM, JEOL-200kV).
- The optical property analysis of different layers of MoS<sub>2</sub> nanosheet materials are done by UV-VIS-NIS (SHIMADZU UV-3600) Spectrophotometer.

## 5.3 Results and discussion

### 5.3.1 Selection of size of MoS<sub>2</sub> nanosheets

We employed a straightforward probe sonication and centrifugation method based on band sedimentation (**Fig. 5.2**) to manufacture dispersions of MoS<sub>2</sub> nanosheets with different thickness and lateral size distributions from the same stock sample. A race layer of higher density was placed on top of a stock dispersion of the surfactant-exfoliated [29] nanomaterial, which was then centrifuged for a brief period of time (usually 10 to 40 minutes). The material spreads throughout the vial as a result of the centrifugation, increasing the mass of the nanosheets from top to bottom [36]. Following fractionation, samples of a particular size can be collected. Similar methods for sorting carbon nanotubes [37, 38], graphene oxide nanosheets [39], and nanoparticles [40] by their lateral dimensions have been previously discussed in literature. While a density gradient media is typically used to obtain the greater race layer density, we combine water and deuterated water to reduce the additive content and prevent any potential interactions between the gradient medium and MoS<sub>2</sub>.

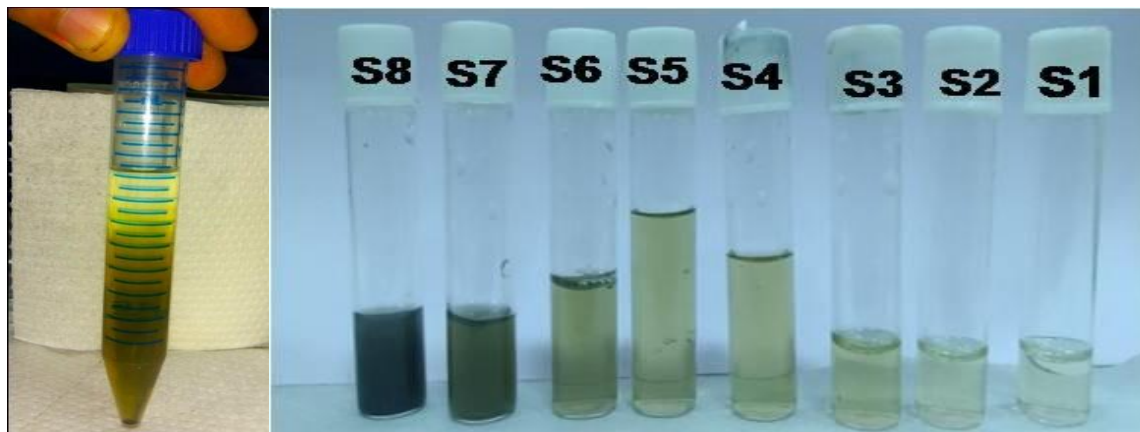


**Fig. 5.2:** The picture shows the image after probe sonication in which band sedimentation centrifugation involves layering a race layer on top of a nanomaterial stock dispersion. The material disperses throughout the vial as a result of centrifugation, which also divides the nanosheets into different sizes and sedimentation velocities. Fractions are removed from top to bottom, as illustrated.

The top fraction of the vial comprises the smallest, slowest-sedimenting species (S1) after probe sonication and band sedimentation centrifugation separated fractions that are roughly 6 mm deep. The extinction spectra of each percent are measured. To distinguish the extinction from the real absorbance, let's name it "Ext," where  $T=10^{-\text{Ext}}$  (T is the optical transmittance). The normalised extinction spectra of a representative group of fractions [7] show the excitonic transitions typical of MoS<sub>2</sub>. We find that the changes in the extinction spectra do, however, show very clear and evident modifications that obviously reflect the different size distributions of the MoS<sub>2</sub> nanosheets in the dispersion, proving that the changes in the extinction spectra reflects the separation process.

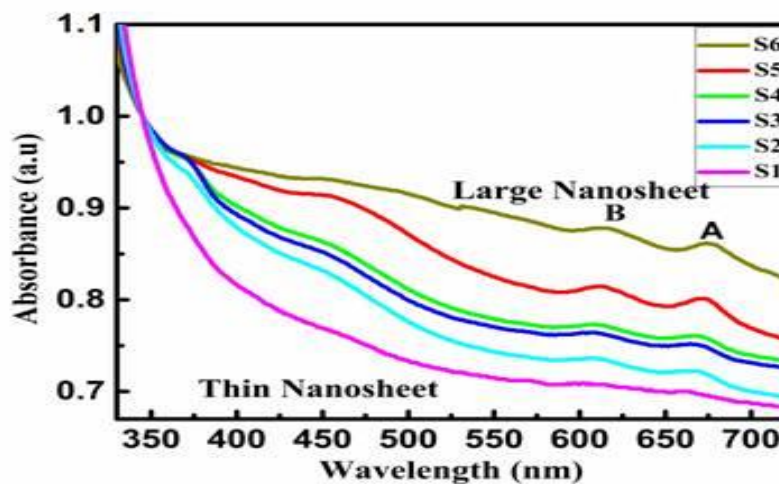


**Fig. 5.3:** Fractional extinction spectra with respect to the local minimum at 345 nm. The A- and B-excitons are marked in their respective locations.

**Fig. 5.3** displays very obvious spectrum shifts between fractions. This ratio changes significantly between S1 and S6, increasing by four times. Since no such observation was made when studying the extinction spectra of films of restacked chemically exfoliated MoS<sub>2</sub> with various nanosheet thicknesses [14], it is obvious that the spectral fluctuations displayed in this are due to changes in nanosheet lateral size. This implies that the extinction spectra hold the quantitative information about the lateral dimensions of the nanosheets. According to the fact that the extinction spectra for MoS<sub>2</sub> dispersions include a contribution from a size-dependent scattering background [18], the position of the A-exciton,  $\lambda_A$ , changed from fraction to percent in addition to the obvious spectrum modifications.

The location of the resulting peak is shown in **Fig. 5.4(a)**, which illustrates a distinct pattern vs sample number. Accordingly,  $\lambda_A$  rises when N, the average number of layers per nanosheet rises because the peak for thicker nanosheets (i.e., at larger fractions) is redshifted.

This behaviour has been observed in a number of TMDs because of confinement effects [41, 42]. This shows that in addition to information about lateral size, the extinction spectra also provide quantitative results on the thickness of the nanosheets.

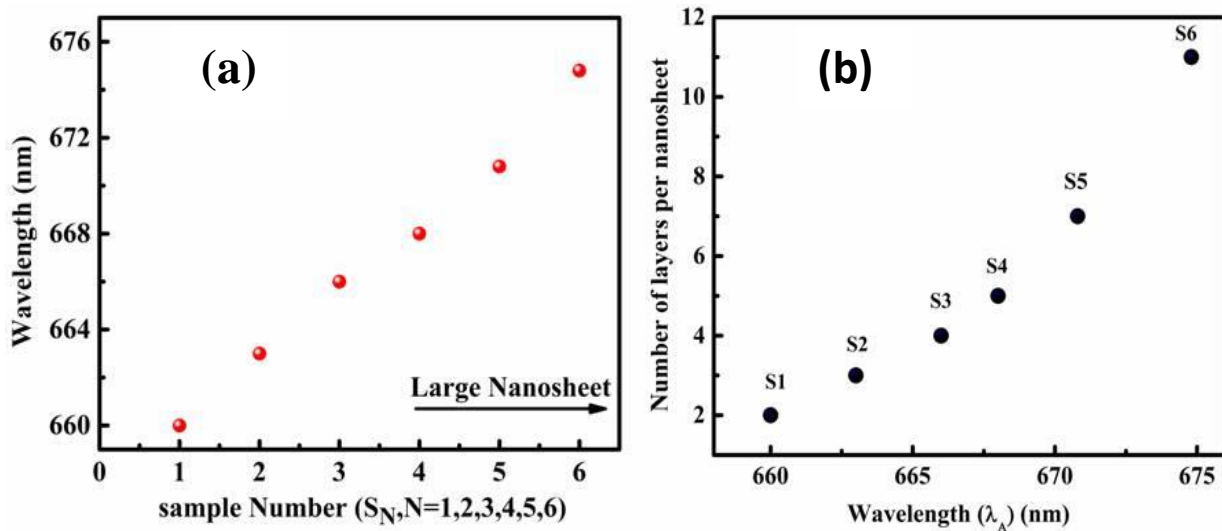


**Fig. 5.4(a, b):** (a) Wavelength (peak position) of the  $\lambda_A$  (A-exciton), as a function of sample number ( $S_N$ ). We suggest that  $Ext_B/Ext_{345}$  and  $\lambda_A$  can be used as metrics for length flake thickness, respectively, (b) Plot showing the average number of layers determined by thickness analysis against the wavelength connected to the A-exciton as determined by both the extinction and the absorbance spectra.

### 5.3.2 Metric for length based on the impacts of nanosheet edges

Using our model we can comprehend the size-dependent modifications to shape the absorption spectra. We can see the spectral structure by using the ratio of absorption intensities. The quantitative relationship between  $L$  and  $Ext_B/Ext_{345}$  can be expressed as follows, assuming that  $\lambda_1$  and  $\lambda_2$  are two separate wavelengths.

$$L(\mu m) = \frac{\frac{3.5Ext_B}{Ext_{345}} - 0.14}{11.5 - Ext_B/Ext_{345}} \quad (1)$$

We calculate the error in  $L$  to be less than 10% by measuring the root-mean-square relative difference between the data and fit. This is significant because it makes it possible to utilise  $Ext_B/Ext_{345}$  to determine the flake length of MoS<sub>2</sub> floating in liquids just by observing the

extinction spectrum. It works well for nanosheets between 90 nm and 300 nm, which is almost exactly the size range of nanosheets that are frequently made by Liquid phase exfoliation techniques. According to the data in **Fig. 5.4(b)**,  $N$  and  $\lambda_A$  have an exponential relationship. When the extinction spectrum's value of  $A$  is used to fit the data, the result is

$$N = 2.3 \times 10^{36} e^{-54,888/\lambda_A} \quad (2)$$

with  $\lambda_A$  is taken in nanometer. Using the extinction spectrum of the  $\text{MoS}_2$  dispersion as a starting point, this expression can be utilised to determine the mean number of monolayers per nanosheet. But as scattering gets increasingly significant for  $N$  approaches 10, we observe that the extinction and absorbance measurements start to diverge. Due to the fact that LPE commonly produces dispersions with  $N$  less than 10, equation (1)'s accuracy is limited to  $N < 10$ , however this is not a severe drawback. Furthermore, it is not required to determine the precise thickness in this domain because the characteristics of  $\text{MoS}_2$  start to resemble those of bulk materials as  $N$  approaches 10 [43].

### 5.3.3 Optical spectra and the impact of nanosheet length

We analysed a number of samples using transmission electron microscopy (TEM) to see if the extinction spectrum provides relevant information regarding nanosheet length. **Fig. 5.5 (a–c)** shows representative TEM images of dispersions that are predicted to contain both large and small nanosheets. These pictures clearly illustrate the anticipated size variations.

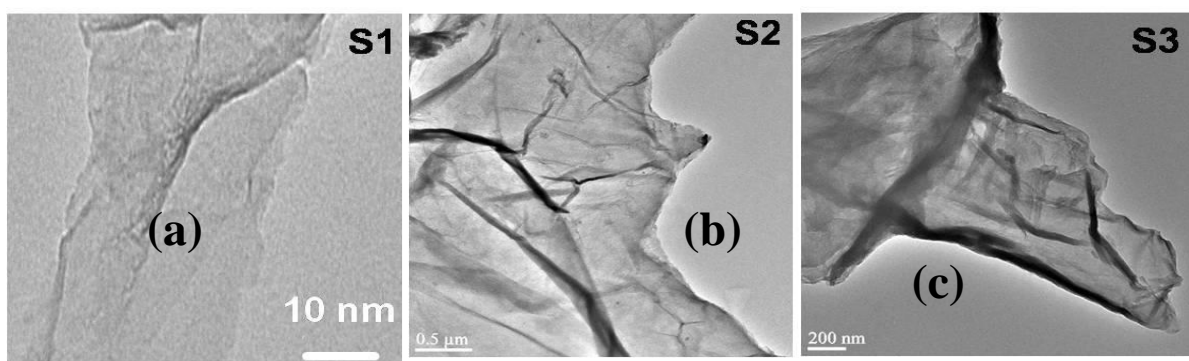


**Fig. 5.5 (a, b, c):** Representative TEM images of slowly sedimenting  $\text{MoS}_2$  nanosheets (a) S1, scale bar, 10 nm, (b) S2, scale bar, 0.5  $\mu\text{m}$ , (c) S3, scale bar, 200 nm).



### 5.3.4 Surface Analysis

A variety of films made from nanosheets of various diameters were subjected to X-ray photoelectron spectroscopy (XPS) in order to prove the existence of a distinct edge area. The Mo core-level spectra showed no consistent alterations. However, as long as we examine freshly generated samples, we notice an additional component that cannot be distinguished with known morphologies, for example 1 T MoS<sub>2</sub> (Fig. 5.6), in addition to the anticipated 2H component of the S 2p core-level spectra.

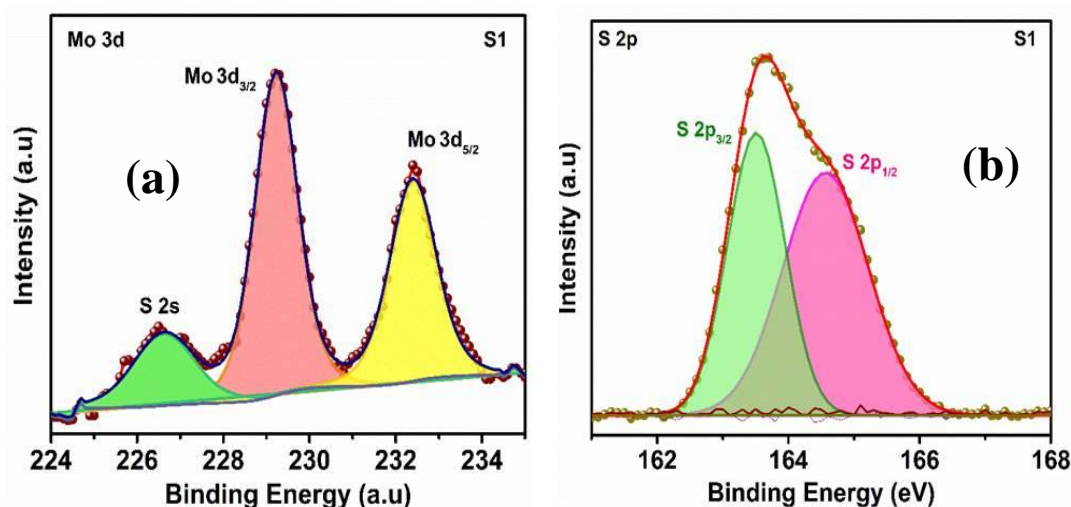


**Fig. 5.6(a, b):** Fitted XPS spectra of core level region of filtered MoS<sub>2</sub> dispersions of S1: (a) Mo 3d (b) S 2p

### 5.3.5 Crystal Structure Analysis

The strongest peak for the 2H-MoS<sub>2</sub> nanosheets and its layers (S1, S2, and S3) in the (002) crystal plane becomes weak and wide in comparison to bulk 2H-MoS<sub>2</sub>, demonstrating the decreased thickness and size of bulk 2H-MoS<sub>2</sub> after being subjected to LPE operations. A slight shift to lower 2 $\theta$  values on the characteristic peak also shows an interlayer expansion along the c-axis (perpendicular to the plane). This can be explained if solvent molecules function during LPE as "wedges" intercalating between nanosheet layers. In fact, phosphorene exfoliation in liquid phase has shown a comparable behaviour via molecular dynamics simulations [44-46]. This process and the intercalation of metal cations in 2D layered materials are somewhat comparable [47].

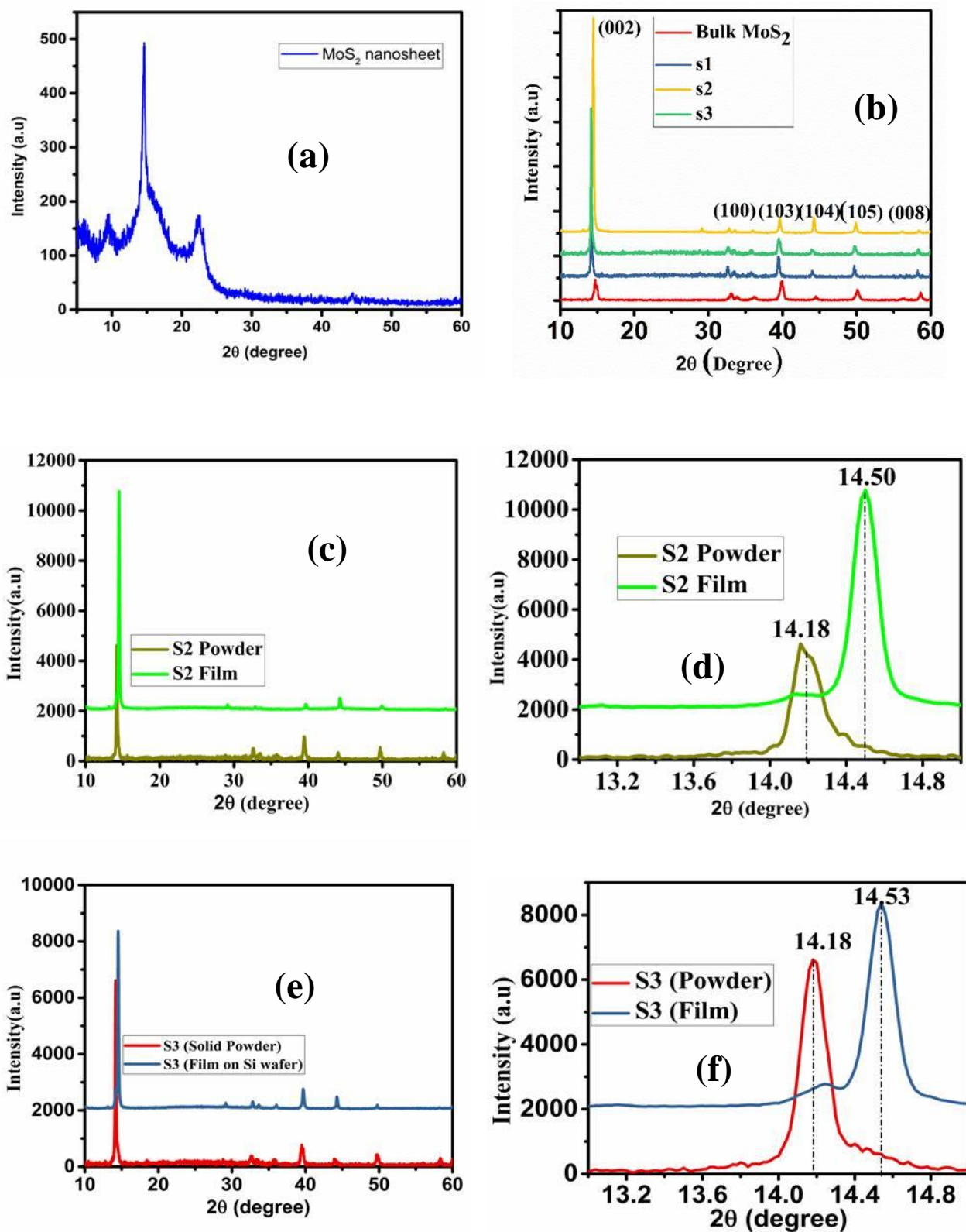


**Fig. 5.7 (a, b, c, d, e, f):** XRD patterns: (a) 2H-MoS<sub>2</sub> nanosheets, (b) Bulk MoS<sub>2</sub> and layers of 2H-MoS<sub>2</sub> nanosheets (S1, S2 and S3), (c, d) S2 (powder and film), (e, f) S3 (powder and film).

### 5.3.6 Raman and FT-IR analysis

Raman spectroscopy was further utilised to characterise the layers of 2H-MoS<sub>2</sub> nanosheets (e.g. S1, S2, and S3) as a useful nondestructive and flexible tool to assess surface structure and to look at the electrical and vibrational properties of 2D materials [48]. The bulk 2H-MoS<sub>2</sub> Raman spectra, as shown in **Fig. 5.8(a)**, only reveal the E<sub>2g</sub><sup>1</sup> and A<sub>1g</sub><sup>1</sup> Raman active modes, which are located at 380 cm<sup>-1</sup> and 405 cm<sup>-1</sup>, respectively. The thickness of the 2H-MoS<sub>2</sub> nanosheets has a significant impact on the frequency shifts of the two modes, which commonly differ from one another. The intercalation of solvent molecules between the nanosheet layers is thought to be the cause of the observed changes in the lattice vibration of 2H-MoS<sub>2</sub> in both the E<sub>2g</sub><sup>1</sup> and A<sub>1g</sub><sup>1</sup> modes as the thickness decreases [49, 50].

FT-IR spectra of the layers of MoS<sub>2</sub> nanosheets (e.g. S1, S2, S3, and S4) were conducted in the range of 4000 to 500 cm<sup>-1</sup> in order to ascertain the chemical interaction and functional groups that are present in the electroactive material. In **Fig. 5.8 (b)**, these spectra are displayed. The intensity of the MoS<sub>2</sub> nanosheets' peaks sharply declines. The observed findings provided significant support for the required chemical interactions, the existence of chemical functional groups, and the change in structural phase.

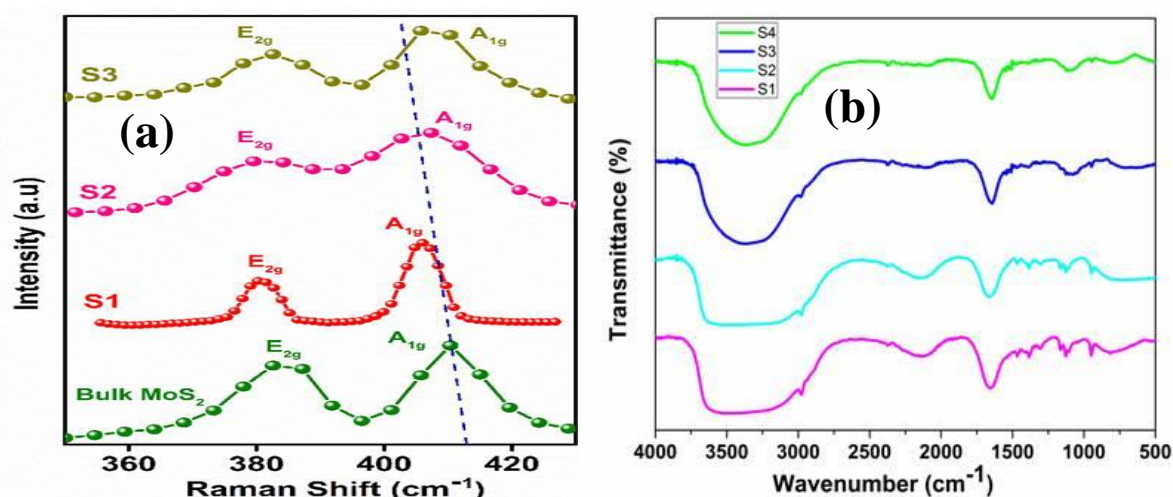


**Fig. 5.8 (a, b):** (a) Raman spectra of bulk MoS<sub>2</sub> and the layers of 2H-MoS<sub>2</sub> nanosheets (S1, S2 and S3), (b) FT-IR spectra of the layers of MoS<sub>2</sub> nanosheets (S1, S2, S3 and S4)

### 5.3.7 Optical Analysis

The fundamental absorption, which corresponds to electron excitation from valence band to conduction band, was used to compute the optical band gap of sample A. The following formula can be used to present their relationship:

$$(\alpha h\nu)^{1/n} = A(h\nu - E_g)$$

Where,

$E_g$  = Band gap of the sample

A = constant

n = Type of transition (n=1/2 for direct bad gap, n=2 for indirect band gap)

Here we plotted  $(\alpha h\nu)^{1/n}$  vs  $h\nu$  taking the direct band gap by taking n=1/2. Extrapolating the linear portion of the graph to  $h\nu$  axis, the indirect band gap was obtained from the intercept, **Fig. 5.9 (a, b, c)**, which were found to be around 1.681 eV and 2.78 eV for sample S1. For sample S2, the indirect band gap was 1.655 eV and for sample S3, the indirect band gap was found to be 1.62 eV and 1.73 eV. It was confirmed from our studies that the as prepared MoS<sub>2</sub> samples exhibits wide band gap.

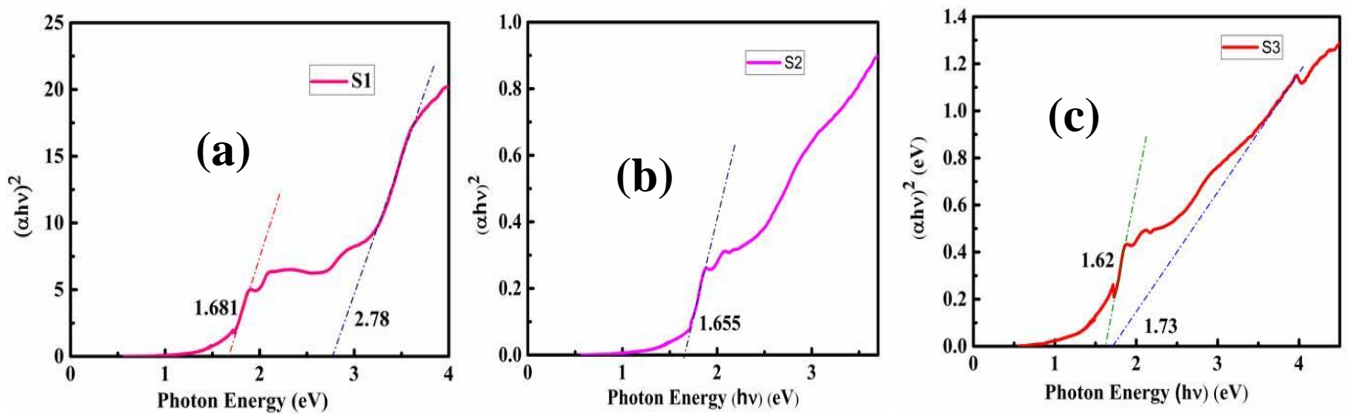


**Fig. 5.9 (a, b, c):** UV-vis absorption spectra; (a) band gap of S1 (b) band gaps of S2 (c) band gap of S3.

## 5.4 Conclusion

Using a traditional tabletop centrifuge, we have successfully created a straightforward and adaptable centrifugation method based on probe sonication method to quickly separate liquid-suspended TMDs according to their mass. Tannic acid was also utilised since it serves two important purposes in this process: It functions as a surfactant at first. We already know that the common characteristic of 2D materials is that when two layers are present, they undergo restacking. Because of using tannic acid, there is a far lower chance of stacking again in this situation. It serves as a surfactant because it prevents restacking. Second, it can enhance the activity of the edge sulfur atoms. The edge sulfur atom of MoS<sub>2</sub> can easily abstract from H<sup>+</sup> ion. During the probe sonication i.e. in the presence of high ultrasonication method or high vibration, some layers, they are separated with each other and the edge sulfur atom which can react with H<sup>+</sup> ion to form H<sub>2</sub>S and H<sub>2</sub>S gas is removed from the system. Hence, we can activate the edge sulfur atom in the present layer dependent MoS<sub>2</sub>.

A number of fractions, or samples with distinctly varied extinction spectra, were produced by this process. This technique may be applied to a variety of nanosheet types like WS<sub>2</sub>, WSe<sub>2</sub> and MoSe<sub>2</sub> that can be employed in different electrochemistry or different catalytic applications since these processes are universal to all 2D materials.

## References:

1. Chhowalla, M. et al. The chemistry of two-dimensional layered transition metal dichalcogenide nanosheets. *Nat. Chem.* 5, 263–275 (2013).
2. Nicolosi, V., Chhowalla, M., Kanatzidis, M. G., Strano, M. S. & Coleman, J. N. Liquid exfoliation of layered materials. *Science* 340, 6139 (2013).
3. Novoselov, K. S. et al. A roadmap for graphene. *Nature* 490, 192–200 (2012).
4. Wang, Q. H., Kalantar-Zadeh, K., Kis, A., Coleman, J. N. & Strano, M. S. Electronics and optoelectronics of two-dimensional transition metal dichalcogenides. *Nat. Nanotechnol.* 7, 699–712 (2012).
5. Geim, A. K. Graphene: status and prospects. *Science* 324, 1530–1534 (2009).
6. Huang, X., Zeng, Z. Y. & Zhang, H. Metal dichalcogenide nanosheets: preparation, properties and applications. *Chem. Soc. Rev.* 42, 1934–1946 (2013).
7. Wilson, J. A. & Yoffe, A. D. Transition metal dichalcogenides discussion and interpretation of observed optical, electrical and structural properties. *Adv. Phys.* 18, 193–335 (1969).
8. Zhan, Y. J., Liu, Z., Najmaei, S., Ajayan, P. M. & Lou, J. Large-area vapor-phase growth and characterization of MoS<sub>2</sub> atomic layers on a SiO<sub>2</sub> substrate. *Small* 8, 966–971 (2012).
9. Frindt, R. F. single crystals of MoS<sub>2</sub> several molecular layers thick. *J. Appl. Phys.* 37, 1928–1929 (1966).
10. Novoselov, K. S. et al. Two-dimensional atomic crystals. *Proc. Natl. Acad. Sci. USA* 102, 10451–10453 (2005).
11. Radisavljevic, B., Radenovic, A., Brivio, J., Giacometti, V. & Kis, A. Single-layer MoS<sub>2</sub> transistors. *Nat. Nanotechnol.* 6, 147–150 (2011).
12. Murphy, D. W. & Hull, G. W. Monodispersed tantalum disulfide and adsorption complexes with cations. *J. Chem. Phys.* 62, 973–978 (1975).
13. Joensen, P., Frindt, R. F. & Morrison, S. R. Single-Layer MoS<sub>2</sub>. *Mater. Res. Bull.* 21, 457–461 (1986).
14. Eda, G. et al. Photoluminescence from chemically exfoliated MoS<sub>2</sub>. *Nano Lett.* 11, 5111–5116 (2011).
15. Zeng, Z. Y. et al. Single-Layer semiconducting nanosheets: high-yield preparation and device fabrication. *Angew. Chem. Int. Ed.* 50, 11093–11097 (2011).

16. Blake, P. et al. Graphene-based liquid crystal device. *Nano Lett.* 8, 1704–1708 (2008).
17. Bourlinos, A. B., Georgakilas, V., Zboril, R., Steriotis, T. A. & Stubos, A. K. Liquid-phase exfoliation of graphite towards solubilized graphenes. *Small* 5, 1841–1845 (2009).
18. Coleman, J. N. et al. Two-dimensional nanosheets produced by liquid exfoliation of layered materials. *Science* 331, 568–571 (2011).
19. Cunningham, G. et al. Solvent exfoliation of transition metal dichalcogenides: dispersability of exfoliated nanosheets varies only weakly between compounds. *ACS Nano* 6, 3468–3480 (2012).
20. Hernandez, Y. et al. High-yield production of graphene by liquid-phase exfoliation of graphite. *Nat. Nanotechnol.* 3, 563–568 (2008).
21. Khan, U. et al. Polymer reinforcement using liquid-exfoliated boron nitride nanosheets. *Nanoscale* 5, 581–587 (2013).
22. Khan, U., O'Neill, A., Lotya, M., De, S. & Coleman, J. N. High-concentration solvent exfoliation of graphene. *Small* 6, 864–871 (2010).
23. Lin, Y., Williams, T. V. & Connell, J. W. Soluble, exfoliated hexagonal boron nitride nanosheets. *J. Phys. Chem. Lett.* 1, 277–283 (2010).
24. O'Neill, A., Khan, U. & Coleman, J. N. Preparation of high concentration dispersions of exfoliated MoS<sub>2</sub> with increased flake size. *Chem. Mater.* 24, 2414–2421 (2012).
25. Zhi, C. Y., Bando, Y., Tang, C. C., Kuwahara, H. & Golberg, D. Large-scale fabrication of boron nitride nanosheets and their utilization in polymeric composites with improved thermal and mechanical properties. *Adv. Mater.* 21, 2889–2893 (2009).
26. Zhou, K. G., Mao, N. N., Wang, H. X., Peng, Y. & Zhang, H. L. A mixed-solvent strategy for efficient exfoliation of inorganic graphene analogues. *Angew. Chem. Int. Ed.* 50, 10839–10842 (2011).
27. Paton, K. R. et al. Scalable production of large quantities of defect-free few-layer graphene by shear exfoliation in liquids. *Nat. Mater.* 13, 624–630 (2014).
28. Wang, J. Z. et al. Development of MoS<sub>2</sub>-CNT composite thin film from layered MoS<sub>2</sub> for lithium batteries. *Adv. Energy Mater.* 3, 798–805 (2013).
29. Smith, R. J. et al. Large-scale exfoliation of inorganic layered compounds in aqueous surfactant solutions. *Adv. Mater.* 23, 3944–3948 (2011).

30. Cunningham, G. et al. Photoconductivity of solution-processed MoS<sub>2</sub> films. *J. Mater. Chem. C* 1, 6899–6904 (2013).
31. May, P., Khan, U. & Coleman, J. N. Reinforcement of metal with liquidexfoliated inorganic nano-platelets. *Appl. Phys. Lett.* 103, 163106 (2013).
32. May, P., Khan, U., Hughes, J. M. & Coleman, J. N. Role of solubility parameters in understanding the steric stabilization of exfoliated two-dimensional nanosheets by adsorbed polymers. *J. Phys. Chem. C* 116, 11393–11400 (2012).
33. Hanlon, D. et al. Liquid exfoliation of molybdenum trioxide. *Chem. Mater.* 26, 1751–1763 (2013).
34. Naguib, M. et al. Two-dimensional transition metal carbides. *ACS Nano* 6, 1322–1331 (2012).
35. Xu, Y., Kominami, K., Ishikawa, Y. & Feng, Q. Layered hydroxide nickel benzoates: hydrothermal synthesis, structure characterization, and exfoliation reaction. *J. Colloid. Interface. Sci.* 386, 107–113 (2012).
36. Svedberg, T., Pederson, K. O. & Bauer, J. H. *The Ultracentrifuge* (Oxford University Press, 1940).
37. Fagan, J. A., Becker, M. L., Chun, J. & Hobbie, E. K. Length fractionation of carbon nanotubes using centrifugation. *Adv. Mater.* 20, 1609–1613 (2008).
38. Fagan, J. A. et al. Centrifugal length separation of carbon nanotubes. *Langmuir* 24, 13880–13889 (2008).
39. Sun, X., Luo, D., Liu, J. & Evans, D. G. Monodisperse chemically modified graphene obtained by density gradient ultracentrifugal rate separation. *ACS Nano* 4, 3381–3389 (2010).
40. Bonaccorso, F., Zerbetto, M., Ferrari, A. C. & Amendola, V. Sorting nanoparticles by centrifugal fields in clean media. *J. Phys. Chem. C* 117, 13217–13229 (2013).
41. Mak, K. F., Lee, C., Hone, J., Shan, J. & Heinz, T. F. Atomically thin MoS<sub>2</sub>: a new direct-gap semiconductor. *Phys. Rev. Lett.* 105, 136805 (2010).
42. Zhao, W. J. et al. Evolution of electronic structure in atomically thin sheets of WS<sub>2</sub> and WSe<sub>2</sub>. *ACS Nano* 7, 791–797 (2013).
43. Lee, C. et al. Anomalous lattice vibrations of single- and few-layer MoS<sub>2</sub>. *ACS Nano* 4, 2695–2700 (2010).
44. V. Sresht, A.A. Padua, D. Blankschtein, Liquid-phase exfoliation of phosphorene: design rules from molecular dynamics simulations, *ACS Nano* 9 (2015) 8255–8268.



45. R.H. Friend, A.D. Yoffe, Electronic properties of intercalation complexes of the transition metal dichalcogenides, *Adv. Phys.* 36 (1987) 1–94.
46. G. Zhou, P. Rajak, S. Susarla, P.M. Ajayan, R.K. Kalia, A. Nakano, P. Vashishta, Molecular simulation of MoS<sub>2</sub> exfoliation, *Sci. Rep.* 8 (2018) 16761.
47. T.Y. Li, Y.H. Liu, B. Chitara, J.E. Goldberger, Li Intercalation into 1D TiS<sub>2</sub>(en) chains, *J. Am. Chem. Soc.* 136 (2014) 2986–2989.
48. B. Chakraborty, H.S.S.R. Matte, A.K. Sood, C.N.R. Rao, Layer-dependent resonant Raman scattering of a few layer MoS<sub>2</sub>, *J. Raman Spectrosc.* 44 (2013) 92–96.
49. A.G. Bagnall, W.Y. Liang, E.A. Marseglia, B. Welber, Raman studies of MoS<sub>2</sub> at high pressure, *Physica B+C* 99 (1980) 343–346.
50. X. Li, J.H. Li, K. Wang, X.H. Wang, S.P. Wang, X.Y. Chu, M.Z. Xu, X. Fang, Z.P. Wei, Y.J. Zhai, B. Zou, Pressure and temperature-dependent Raman spectra of MoS<sub>2</sub> film, *Appl. Phys. Lett.* 109 (2016).

**CHAPTER 6**

**HER and ORR Kinetics**

**of Zn doped MoS<sub>2</sub>**

## 6.1 Introduction

Fuel cells and clean renewable hydrogen energy are needed as alternatives to natural energy because they are environment friendly, have an abundant supply, and have a high energy density as the environmental and energy crises worsen as a result of unwise development [1-3]. Since then, green energy has been divided into three categories: sustainable energy, the optimisation of conventional energy sources, and fuel cells. Due to their superior combustion efficiency, superior thermal conductivity, and higher energy density, hydrogen and oxygen fuel are thought to be the most promising green energy sources [4]. In comparison to the steam reformation of fuels (such as methane and ethanol), which is seen to be the primary and efficient method, it has been shown that the production of hydrogen by electrolyzing water in acidic medium hydrogen evolution reaction (HER) is more environment friendly [5-7].

The improvement of HER electrocatalysts, however, will allow for the replacement of noble metals with inexpensive, abundant, and extremely stable electrocatalysts [8]. The creation of high efficiency catalysts with quick kinetics and low overpotential is crucial for the HER and oxygen reduction reaction (ORR) processes, as a result [9, 10].

Finding alternate sources of energy is crucial due to the depletion of natural energy [11–13]. Low temperature fuel cells, particularly polymer electrolyte membrane fuel cells (PEMFCs), stand out among the few alternatives because of their great efficiency and negligible carbon emissions [14]. Due to their considerably higher current density and lower overpotential, PEMFCs often use platinum (Pt) based electrocatalysts for more sluggish cathodic ORR kinetics. By enhancing their performance in terms of power output, efficiency, and durability, PEM fuel cells can be made more effective [15].

Due to the high cost of Pt (Platinum), its scarcity, and its poor stability under fuel cell working conditions, PEM fuel cell technology is not completely viable [16]. The ORR, which can reduce fuel cell lifetimes in many devices due to electrode fouling, is a significant flaw of PEM fuel cells [17]. The ORR happens at the cathode of PEM fuel cells, where fuel cell degradation [18] and the ORR are convertible because hydrogen peroxide ( $\text{H}_2\text{O}_2$ ) is produced when oxygen is reduced using catalysts that use the two electron pathway [19]. Since  $\text{H}_2\text{O}_2$  and other hazardous byproducts are not produced by the direct two four electron pathway, it is preferable [20]. Therefore, a thorough search for a Pt substitute without sacrificing stability

and catalytic activity is required. As a result, research is focused on developing less expensive nonprecious metal catalysts [22] and, more importantly, metal-free carbon-based materials [21].

Numerous transition metal compounds, such as sulphides [23, 24], selenides [25], phosphides [26], nitrides [27], and carbides [28], have recently come to light as promising HER electrocatalysts. Two-dimensional transition-metal dichalcogenides (2D-TMDCs) are among these substances, and they have drawn a lot of attention because of their exceptional capacity for producing clean energy through photocatalysis [29], photovoltaic activities [30], and electrochemical water splitting [31]. Particularly, transition-metal disulfides (TMDs) such as  $\text{MoS}_2$  and  $\text{WS}_2$  have been shown to act as catalysts for efficient HER and ORR because they are more resilient to the environment and chemicals for longer periods of time [32, 33]. Since then, it has been established that the electrochemical processes are dominated by the TMDCs edge sites, whilst the basal planes have been shown to be inert [34]. Aside from that, the theoretical investigation of the HER of 2D-TMDCs has shown that the unstrained materials exhibit poor HER activity because only chalcogen atoms participate in the process, whereas TM atoms are assumed to be inert [35–37]. Based on this result, substitutional doping in TMDCs or alloy engineering in ternary TMDC alloys are the best methods for modifying HER activity [38, 39].

The substitutional / atomic doping might result in the creation of extra strain in the crystal structure because of the mismatch in the atomic sizes of the host and dopant elements [40]. This method can be simply applied for the efficient generation of energy and can considerably boost HER activity [41]. It can be demonstrated that the metallic element doping in TMSs can change electronic configurations of catalysts and optimise hydrogen adsorption energy; for this reason, it is considered an effective method to obtain excellent TMS electrocatalysts. In this case, various works were dedicated to the modulation of the electronic structure by various means, such as doping and interface or defect engineering.

So, various methods have been used to enhance the HER and ORR properties of  $\text{MoS}_2$  electrocatalysts, and persistent work over the past few years has resulted in a number of successes, including doping with specific heteroatoms, phase transition, combining with conductive substrates (such as carbon nanotubes (CNTs), reduced graphene oxides, and control of the morphology or structures to add more readily available active sites [42]. Among them, the method of appropriate metal doping deserves special attention since it can

efficiently facilitate the HER activity of transition-metal dichalcogenides by concurrently boosting the active sites and conductivity. Metal-doped MoS<sub>2</sub> will be a potential system to further research how to effectively enhance the HER and ORR processes, thanks to these crucial conductivity and active site points. In particular, Zn dopant can act as both the active site and a catalyst for the catalytic activity of S atoms in the basal plane. Additionally, Zn dopant can improve pure MoS<sub>2</sub>'s conductivity, which leads to outstanding HER and ORR performance.

## **6.2 Experimental Section**

### **6.2.1 Sample preparation**

#### **6.2.1.1 Hydrothermal synthesis of Zinc doped MoS<sub>2</sub>**

- Molybdenum sulfide powder (100mg) and Zinc acetate (30mg / 40mg) were grinded for 1 hour in a mortar pestle.
- The mixed powder is then dissolved in 80 ml DI water and ultrasonicated for 30 min.
- After that the solution was transferred into a 100 ml Teflon-lined stainless-steel autoclave and sealed tightly, subsequently heated for 18 h at 180 °C.
- After the reaction was completed, the system was naturally allowed cool down to ambient temperature. The black precipitates were retrieved from the solution by filtration and washed with DI water and ethanol several times.
- Finally, the samples were dried overnight at 40 °C in an oven to obtain the powder products.

Variation in the amount of Zinc acetate during the synthesis procedure resulted in the asprepared samples named MoS<sub>2</sub>-30 (30mg) and MoS<sub>2</sub>-40 (40mg) respectively.

### 6.2.2 Characterizations

The characterizations of the as-prepared materials were done by various techniques to have a proper insight into the formation of phases, chemical bonding, morphology, and compositional analysis.

- The analysis of the phase formation of the catalysts was done by X-ray diffraction (XRD, Bruker D8 advanced) that is accompanied by Cu K $\alpha$  source ( $\lambda=1.54 \text{ \AA}$ ), from the range of  $2\theta=10$  to  $60^\circ$  and at a scan rate of  $2\text{min}^{-1}$ .
- X-ray Photoelectron Spectroscopy (XPS) using a monochromatic Al K $\alpha$  X-ray source ( $h\nu =1486.6 \text{ eV}$ ) and a hemispherical analyzer (SPECS HSA 3500) is used for the surface analysis of the prepared samples.
- The analysis of the Raman shift of the samples was done by Using Witec Raman Spectroscopy that is combined with a laser source (wavelength 532 nm).
- For the structural morphology of the materials, the Field Emission Scanning Electron Microscopy (FESEM, Hitachi S-4800) was used which was equipped with an Energy Dispersive X-ray Spectroscopy (EDS) for the analysis of the compositional ratios of the materials.

### 6.2.3 Electrochemical property measurements

Glassy carbon electrode (GCE) was used as the working electrode in a three electrode configuration system for the measurement of HER, ORR, Nyquist, and stability tests. Graphite rod and Ag/AgCl are used as counter and reference electrodes in the AUTOLAB PGSTAT302N (M-204) 1.1 Nova software, respectively. The sample ink was prepared by adding 40 $\mu\text{L}$  of DMF and 10 $\mu\text{L}$  of nafion to the 1 mg catalyst and ultrasonicated it for one hour prior to the experiment. To get a uniform black coating of the material on the electrode's active surface, the resulting paste was pipette- and drop-cast onto the working region of the glassy carbon electrode. 0.5 M H $_2$ SO $_4$  and 1 M KOH were used as the electrolyte solution for the HER and ORR experiments. For the HER and ORR measurements, the electrolyte solution was first purged for 30 minutes with high grade N $_2$  gas and O $_2$  gas (Indian Refrigeration system, 99.99% purity). The following outlines the possibility for HER to a reversible hydrogen electrode (RHE):

$$E_{(HER)} = E_{Ag/AgCl} + 0.198 V \quad 1$$

For ORR measurements the potential to a reversible hydrogen electrode (RHE) are as follows:

$$E_{RHE} = E_{Ag/AgCl} + (2.303RT/F) pH + E_{Ag/AgCl}^0 \quad 2$$

Electrochemical impedance spectroscopy (EIS) measurements are carried out at potential -0.4 V vs. RHE with an ac amplitude at a frequency range of 0.01–1000 kHz. For durability measurements, linear sweep voltammetry (LSV) is carried out at a scan rate 30 mV/s up to 1000 cycles. According to Koutecky–Levich (K-L) approach, Limiting and kinetic Current densities, electron transfer number, and rate constant has been calculated as follows [28]:

$$\frac{1}{J} = \frac{1}{J_K} + \frac{1}{J_L} \quad 3$$

$$\frac{1}{J} = \frac{1}{J_K} + \frac{1}{B\omega^{\frac{1}{2}}} \quad 4$$

$$J_K = nFKC_0 \quad 5$$

Where  $n$  denotes number of electrons transferred in ORR,  $F$  is the Faraday constant (96,485 C mol<sup>-1</sup>),  $\nu$  is the kinematic viscosity of the electrolyte (0.01 cm<sup>2</sup>/s),  $D$  is the diffusion coefficient of an oxygen molecule (1.9 × 10<sup>-5</sup> cm<sup>2</sup>/s),  $C_{O_2}$  is the bulk concentration of oxygen (1.2 × 10<sup>-6</sup> mol/cm<sup>3</sup>),  $\omega$  is the rotation and  $J_k$  is the rate kinetic current density.

## 6.3 Results and Discussion

### 6.3.1 Structural and Raman Study

**Figure 6.1(a)** shows the X-ray diffraction (XRD) patterns of bulk and Zn-doped MoS<sub>2</sub> (MoS<sub>2</sub>-30 and MoS<sub>2</sub>-40) having prominent diffraction peaks at  $2\theta$ -14.3°, 32.82°, 33.6°, 39.59°, 44°, 49.70°, and 58.5° are indexed to be (002), (100), (101), (103), (006), (105), and (110) planes of the MoS<sub>2</sub>(JCPDS card no. 06-0097). For both of the Zn-doped MoS<sub>2</sub> samples, there has been a clear broadening and shift of the peak along with a significant decrease in peak intensity. However, no further peaks have been observed following Zn doping, indicating excellent sample purity. In general, Zn is smaller than Mo, and there is a chance that Zn<sup>2+</sup> will experience both substitutional and interstitial doping. MoS<sub>2</sub>-30 and MoS<sub>2</sub>-40 have crystallite sizes in the (002) plane that are 9.87 nm and 17.09 nm, respectively.

To further investigate the structure of Zn-doped MoS<sub>2</sub> catalysts, Raman spectroscopy are employed and the results are shown in **Fig. 6.1(b)**. Bulk MoS<sub>2</sub> shows one major peak at 382 cm<sup>-1</sup> and a weak peak at 407 cm<sup>-1</sup>, which corresponds to the out of plane A<sub>1g</sub> and in plane E<sub>1g</sub><sup>1</sup> modes, respectively [43]. The Raman spectra of Zn-doped MoS<sub>2</sub> catalysts show similar characteristics to bulk MoS<sub>2</sub>, with an approximately 3 cm<sup>-1</sup> and 2.0 cm<sup>-1</sup> shift of the A<sub>1g</sub> mode MoS<sub>2</sub>- 30 and MoS<sub>2</sub>-40 respectively.

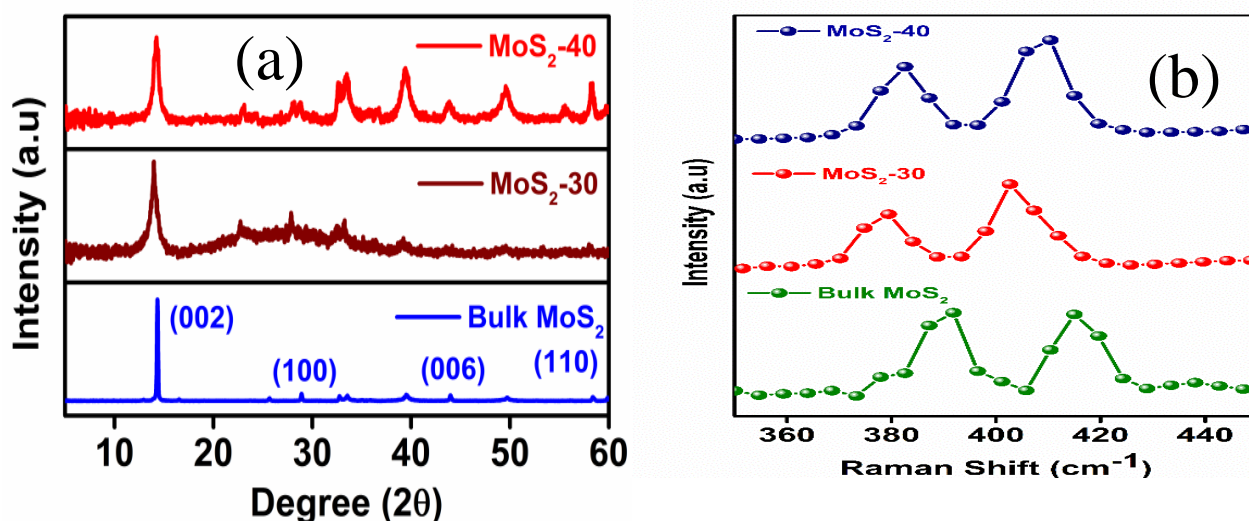


**Fig. 6.1(a, b):** (a) Powder X-ray diffraction patterns for Zn-doped MoS<sub>2</sub>. (b) Raman spectra of Bulk MoS<sub>2</sub>, MoS<sub>2</sub>-30 and MoS<sub>2</sub>-40



### 6.3.2 Morphology Study

**Fig. 6.2(a, b)** shows the FESEM images of the MoS<sub>2</sub>-30 and MoS<sub>2</sub>-40 at different magnification. A nanosheet like structure of the MoS<sub>2</sub> was observed. **Fig. 6.2(c, d)** shows the atomic percentage of individual component and elemental analysis and mapping of the Zn doped MoS<sub>2</sub> materials. The presence of Zn, Mo, and S confirmed the synthesis of the Zn doped MoS<sub>2</sub> materials.

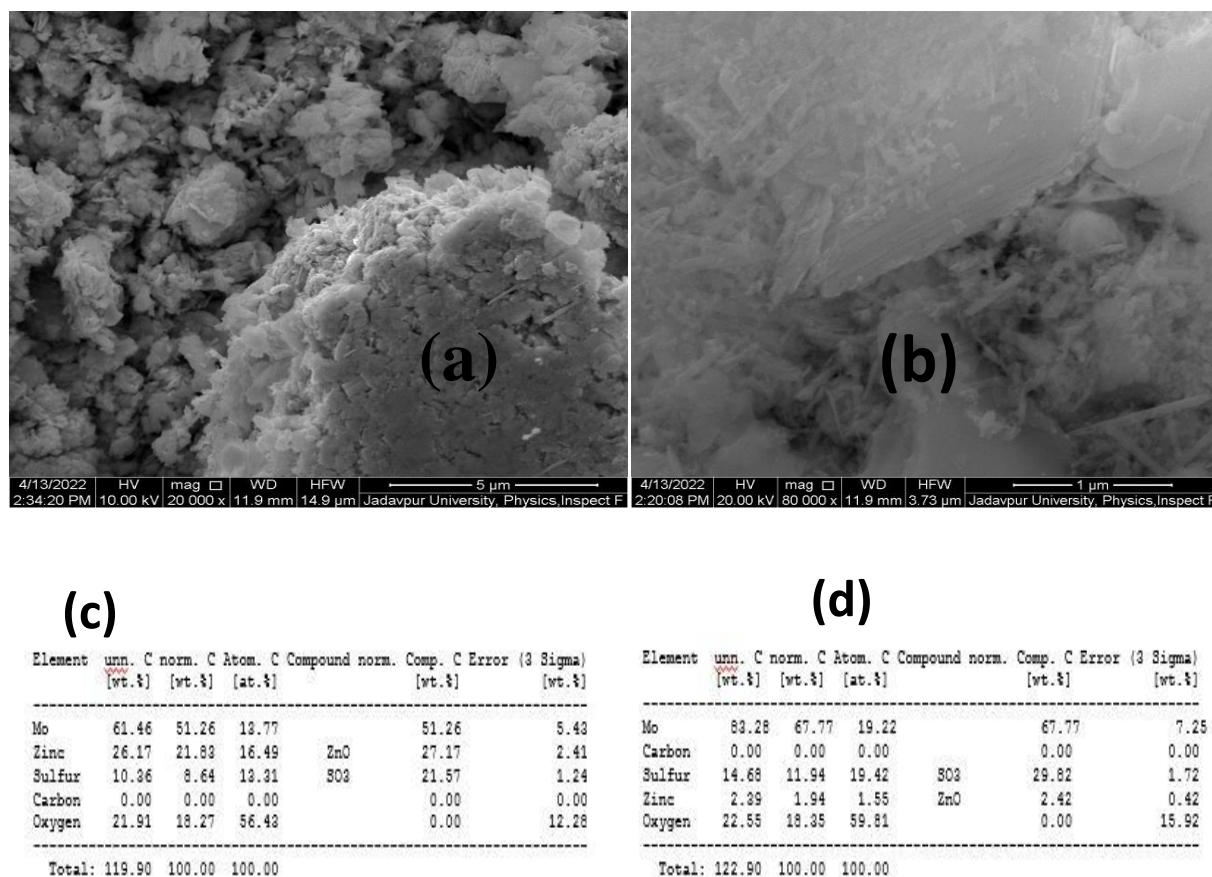


**Fig. 6.2(a, b, c, d):** FESEM image and elemental analysis of individual component (a, c) MoS<sub>2</sub>-30, (b, d) MoS<sub>2</sub>-40

### 6.3.3 Surface Study

X-ray photoelectron spectroscopy (XPS) was performed to analyze surface states and chemical valence of the sample. As shown in **Fig. 6.3(a)**, the high-resolution Mo 3d XPS spectra exhibits peaks at 233.0 and 229.8 eV, assigning to the binding energies of Mo<sup>4+</sup> 3d<sub>3/2</sub> and Mo<sup>4+</sup> 3d<sub>5/2</sub>, respectively, which belong to MoS<sub>2</sub>-30 [44]. In addition, the peak located at

236.5 eV can be ascribed to the electron binding energy of  $\text{Mo}^{6+} 3d_{3/2}$ , owing to a small portion of oxidized  $\text{Mo}^{4+}$  to  $\text{Mo}^{6+}$  in the air [44]. There exists a small peak at 226.0 eV, which can be assigned to the Mo-S bond. The high-resolution S 2p signals of  $\text{MoS}_2$  yielded a pair of remarkable peaks at 163.8 and 162.6 eV, corresponding to the divalent sulfur ions ( $\text{S}^{2+}$ ) with S 2p<sub>1/2</sub> and S 2p<sub>3/2</sub>, respectively as shown in **Fig. 6.3(b)** [45]. The XPS spectrum of Zn 2p exhibits two peaks at 1045.92 eV and 1024.06 eV corresponding to Zn 2p<sub>1/2</sub> and Zn 2p<sub>3/2</sub> state as shown in **Fig. 6.3(c)**, confirming that zinc is successfully incorporated in  $\text{MoS}_2$  nanoflakes.

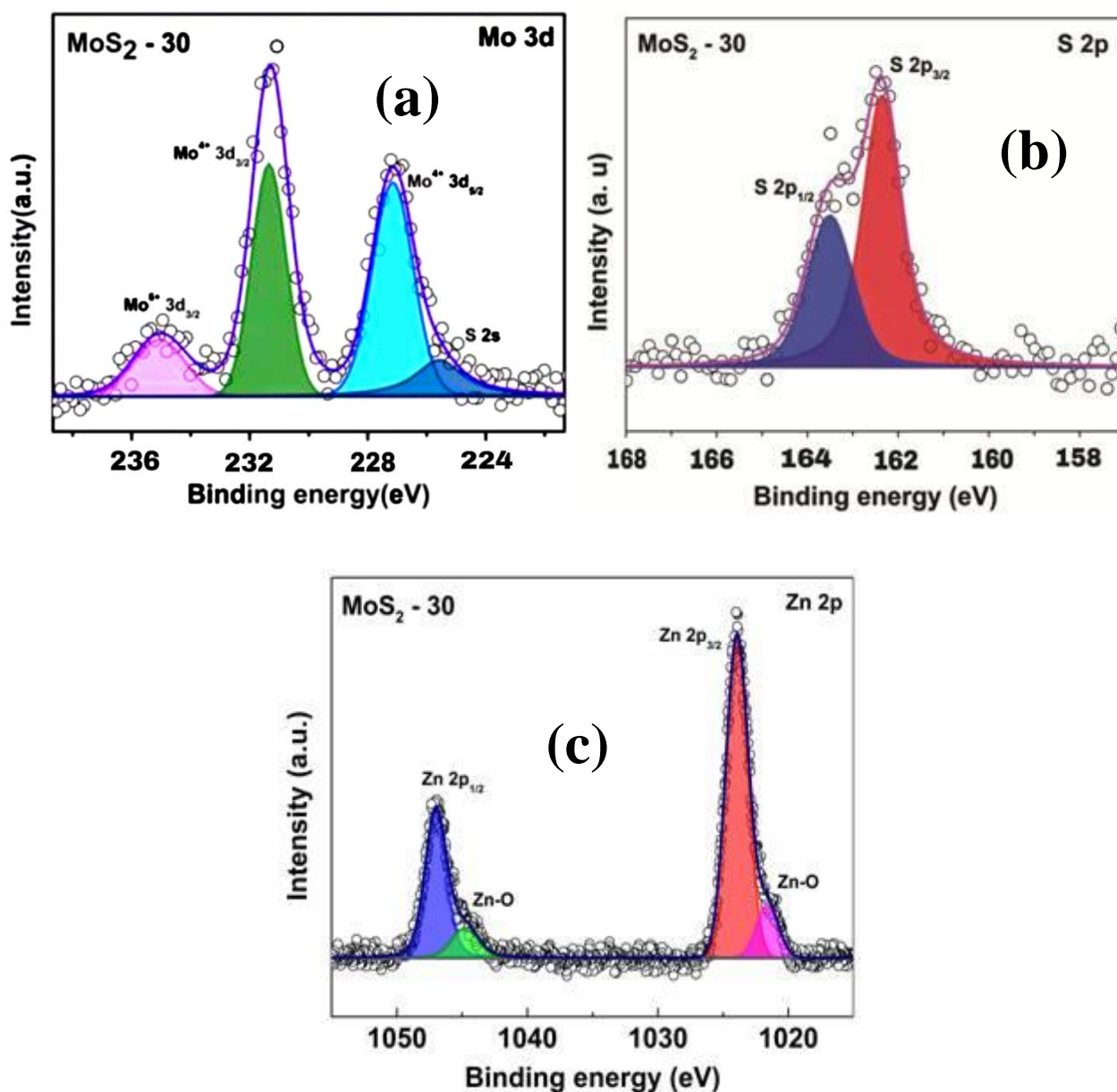


**Fig. 6.3(a, b, c):** XPS Spectra of Zn doped  $\text{MoS}_2$  ( $\text{MoS}_2$ -30): (a) Mo 3d, (b) S 2p, (c) Zn 2p

### 6.3.4 Experimental HER activity

Herein, we have measured the electrochemical HER activities for both Zn-doped MoS<sub>2</sub> catalysts by using a typical three-electrode setup in 0.5 M H<sub>2</sub>SO<sub>4</sub>. **Fig. 6.4(a)** shows the linear sweep voltammetry (LSV) curves of both catalysts having Zn doped MoS<sub>2</sub> catalysts have better HER performance than that of pure MoS<sub>2</sub> (Bulk-MoS<sub>2</sub>). With increasing the concentration of Zn<sup>2+</sup>, the HER performance is also enhanced implying doping concentration of Zn plays a crucial role in the improved HER performance. MoS<sub>2</sub>-30, MoS<sub>2</sub>-40 and Bulk-MoS<sub>2</sub> manifest the onset potential of 180 mV, 200 mV and 350 mV respectively. The rate-limiting step has been measured from Tafel slopes that follows Volmer-Tafel pathway. The Tafel slopes of Bulk MoS<sub>2</sub>, MoS<sub>2</sub>-30 and MoS<sub>2</sub>-40 are calculated to be 138 mV/dec, 70mV/dec and 76mV/dec as follows Volmer-Heyrovsky mechanism accelerated by different interface structure due to various dopant sites for catalytic behavior. The lower Tafel slope for MoS<sub>2</sub>-30 and MoS<sub>2</sub>-40 suggests facile kinetics and faster enhancement of the HER rate as shown in **Fig. 6.4(b)**.

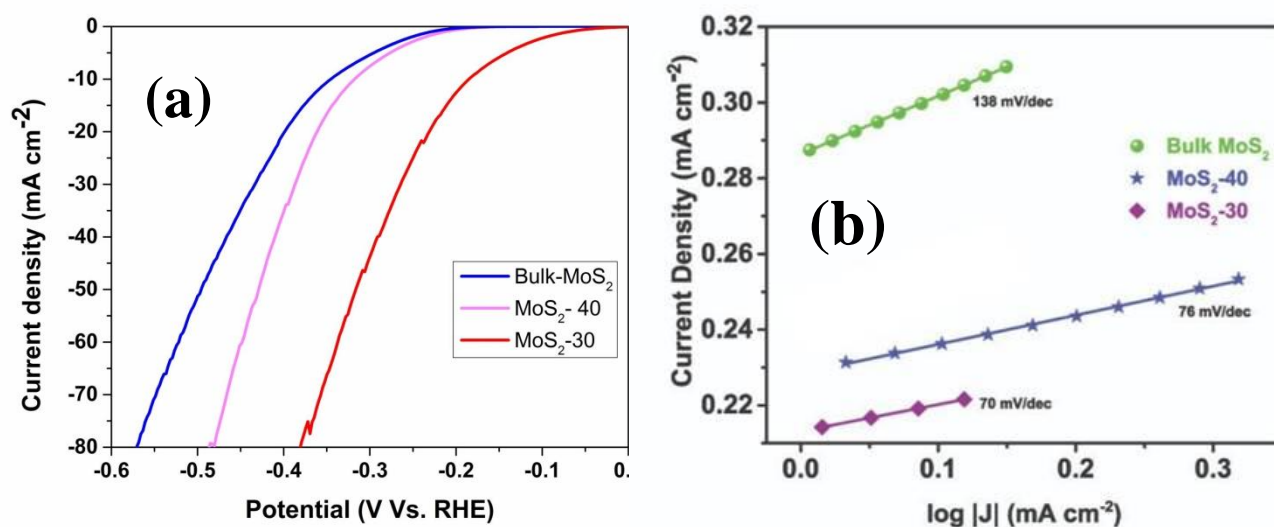


**Fig. 6.4(a, b):** (a) LSV polarization curves for HER of Bulk-MoS<sub>2</sub> and different Zn doped MoS<sub>2</sub> in N<sub>2</sub>-saturated 0.5 M H<sub>2</sub>SO<sub>4</sub> solution with a scan rate of 10 mV s<sup>-1</sup> respectively, (b) Tafel slopes of bulk MoS<sub>2</sub>, MoS<sub>2</sub>-30 and MoS<sub>2</sub>-40.

More importantly, the long-time cycling durability is another significant factor for any catalytic reaction. As illustrated in **Fig. 6.5**, it is nearly depicted the current density is almost unchanged over 1000 cycles of continuous tests, demonstrating the superior stability of the MoS<sub>2</sub>-30 catalyst during the HER process. Therefore, with the lower overpotential, faster enhancement of the HER rate with the increase in potential (by analyzing the lowest Tafel plot) of MoS<sub>2</sub>-30 manifests Zn doping enhances conductivity and greater number of available active sites for HER kinetics.

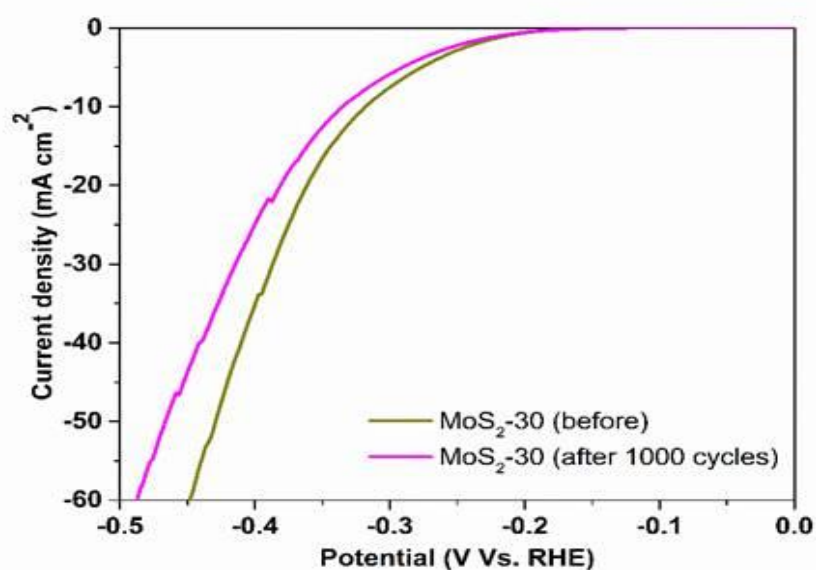


**Fig. 6.5** Stability tests by measuring the polarization profiles for MoS<sub>2</sub>-30 catalyst before and after 1,000 cyclic potential scans in 0.5 M H<sub>2</sub>SO<sub>4</sub> at a scan rate of 10 mV s<sup>-1</sup>.

**Table 6.1** : HER activity comparison of both Zn-doped MoS<sub>2</sub> catalysts in 0.5 M H<sub>2</sub>SO<sub>4</sub> electrolyte. The potential has been calculated in RHE.

Materials	Over Potential ( $\eta$ ) At 10 mA cm <sup>-2</sup> (mV)	J <sub>Onset</sub> (mV)	Tafel Slope (mV/decade)
Bulk MoS <sub>2</sub>	482	350	138
MoS <sub>2</sub> -30	303	180	70
MoS <sub>2</sub> -40	314	200	76

### 6.3.5 Experimental ORR activity

The ORR catalytic activity of bulk-MoS<sub>2</sub> and Zn-doped MoS<sub>2</sub> (MoS<sub>2</sub>-30 and MoS<sub>2</sub>-40) was investigated via comparative Cyclic Voltammograms in Oxygen saturated 0.1 M KOH solution at a sweep rate of 10 mV/s. ORR activities are studied through linear sweep voltammograms (LSVs) using the rotating disk electrode technique (RDE) by varying the rotation speed from 100 rpm to 1600 rpm as shown in **Fig. 6.6(a, b)**. From the LSV polarisation curve, the onset potential ( $E_{\text{onset}}$ ) of MoS<sub>2</sub>-30 and MoS<sub>2</sub>-40 exhibit quite similar values of 0.68 V vs. RHE and 0.66 V vs. RHE respectively at 1600 rpm. Moreover, the limiting-diffusion current density ( $J_L$ ) at 1600 rpm obtained for the MoS<sub>2</sub>-30 was -4.60 mA cm<sup>-2</sup> and for MoS<sub>2</sub>-40 it was -3.41 mA cm<sup>-2</sup> at -0.8 V vs. Ag/AgCl (0.1 V vs. RHE).

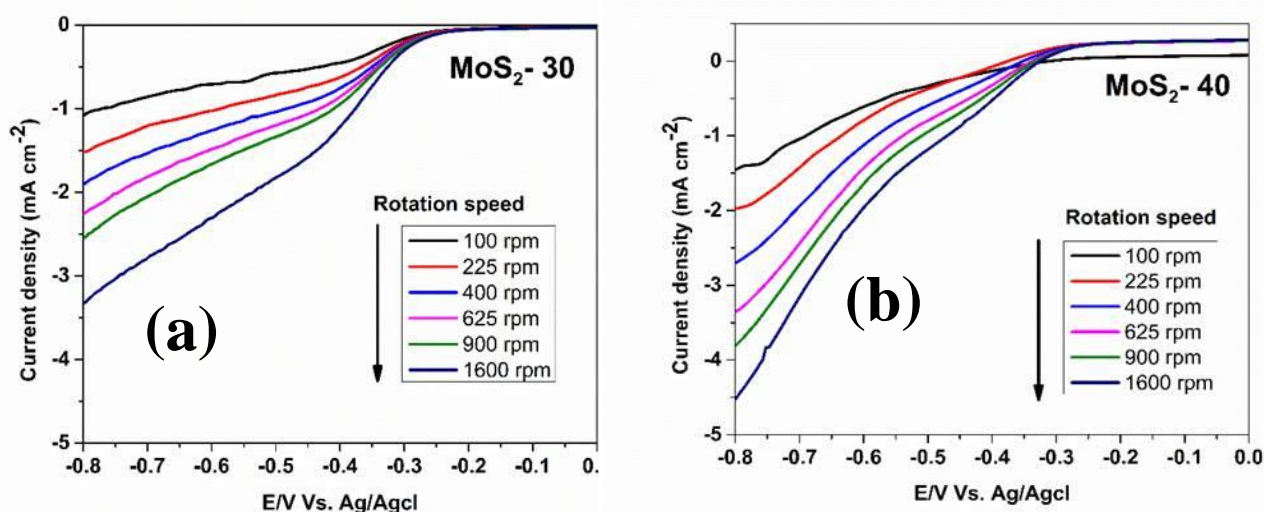


**Fig. 6.6 (a, b):** RDE plots with different rotation speeds (a) MoS<sub>2</sub>-30, (b) MoS<sub>2</sub>-40

The linear fitting of the Koutecky–Levich (K–L) plots of both the synthesized samples at different potentials reveals 1st order reaction kinetics as shown in **Fig. 6.7(a, b)**. It is obvious that the inactive basal plane and high charge transfer resistance of MoS<sub>2</sub> inhibit the ORR performance owing to two electron transfer processes. The observed kinetic current density ( $J_k$ ) was 4.70 mA cm<sup>-2</sup> and 8.71 mA cm<sup>-2</sup> at -0.8V vs. Ag/AgCl for MoS<sub>2</sub>-40 and MoS<sub>2</sub>-30 respectively.



The slope (B) can be obtained to deduce the number of electrons transferred (n), which is calculated to be 3.8 and 4.1 in case of MoS<sub>2</sub>-30 and MoS<sub>2</sub>-40, revealing a Pt-like single step nearly 4-electron transfer pathway leading to direct formation of H<sub>2</sub>O.

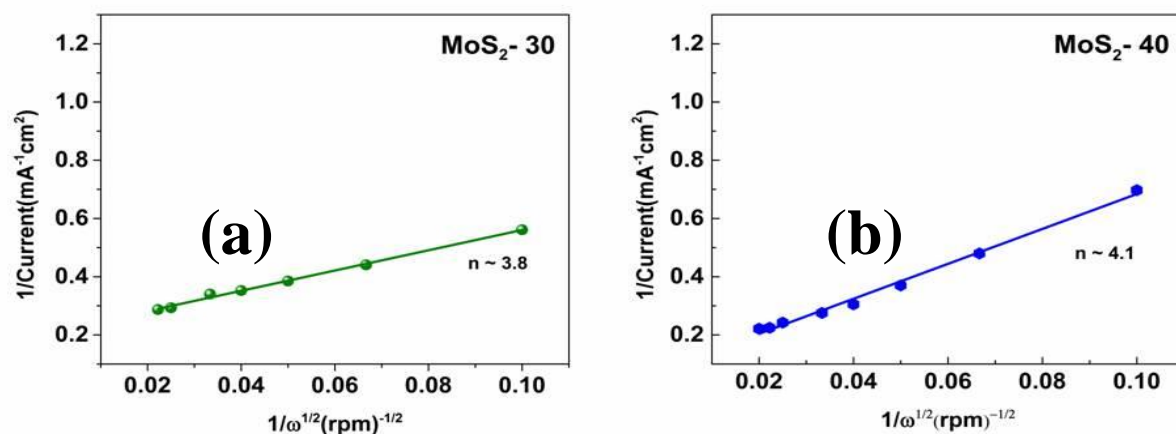


**Fig. 6.7(a, b):** Koutecky-Levich (K-L) plot at different potential from -0.8 V to -0.6 V vs. Ag/AgCl (a) MoS<sub>2</sub>-30, (b) MoS<sub>2</sub>-40

The kinetic behavior has been illustrated by the Tafel slope where MoS<sub>2</sub>-30 exhibit very low Tafel slopes of 120 mV dec<sup>-1</sup> compared to MoS<sub>2</sub>-40 (236 mV dec<sup>-1</sup>) as shown in **Fig. 6.8**. Thus, the doping effect overcomes the potential barrier for HER and ORR kinetics w.r.t bulk MoS<sub>2</sub>.

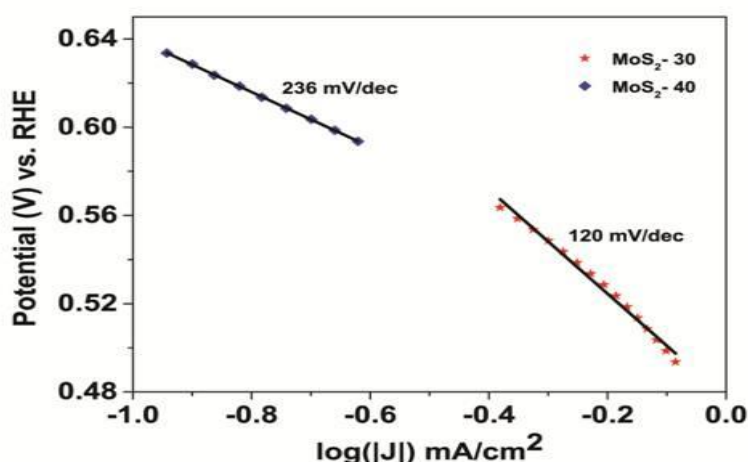


**Fig. 6.8:** Tafel plot of MoS<sub>2</sub>-30 and MoS<sub>2</sub>-40

**Table 6.2 :** Comparison of various ORR parameters for both materials. The potential has been calculated in RHE.

Catalysts	E <sub>Onset</sub> (V)	J <sub>L</sub> at 1600 rpm (mA/cm <sup>2</sup> )	J <sub>K</sub> at 0.1 (V) (mA/cm <sup>2</sup> )	n	Tafel Slope (mV/Decade)
MoS <sub>2</sub> -30	0.68	-4.60	8.71	3.8	120
MoS <sub>2</sub> -40	0.66	-3.41	4.70	4.1	236

## 6.4 Conclusion

In this work, we have reported that Zn-doped MoS<sub>2</sub> exhibits increased electrochemical activity when compared to pure MoS<sub>2</sub>. The produced Zn-doped MoS<sub>2</sub> (MoS<sub>2</sub>-30) exhibits outstanding HER and ORR performance and has a low Tafel slope of 70 mV/dec with the shortest onset potential (180 mV) as well as good stability. Therefore, this work provides a reliable strategy to design other low-cost and high-powered transition-metal dichalcogenide electrocatalysts to exhibit four electron ORR pathways rather than toxic H<sub>2</sub>O<sub>2</sub> production at the intermediate. This work presents a feasible technique for modifying the electronic structure of electrocatalysts for efficient hydrogen production and oxygen reduction. It also provides experience in designing extremely effective Earth-abundant electrocatalysts for different applications in future energy.

## References:

1. J. Alper Water splitting goes au nature (2003) 1686-1687.
2. Q. Liu , J. Tian, , J. W. Cui, , P. Jiang, , N. Cheng, , A.M. Asiri, and X. Sun, , Carbon nanotubes decorated with CoP nanocrystals: a highly active non- noble- metal nanohybrid electrocatalyst for hydrogen evolution. *Angew. Chem. Int. Ed.* 53 (2014) 6710-6714.
3. L. Cheng, W. Huang, Q. Gong, C. Liu, Z. Liu, Y. Li, and H. Dai. Ultrathin WS<sub>2</sub> nanoflakes as a high- performance electrocatalyst for the hydrogen evolution reaction. *Angew. Chem. Int. Ed.* 126 (2014) 7994-7997.
4. B. Wolter, M.G. Pullen, M. Baudisch, M. Sclafani, M. Hemmer, A. Senftleben, C.D. Schröter, J. Ullrich, R. Moshhammer, and J. Biegert, Strong-field physics with mid-IR fields *Physical Review X* 5 (2015) 021034.
5. N. Laosiripojana, and S. Assabumrungrat, Catalytic steam reforming of methane, methanol, and ethanol over Ni/YSZ: The possible use of these fuels in internal reforming SOFC. *J. Power Sources* 163 (2007) 943-951.
6. V. ed. Dusastre, *Materials for sustainable energy: a collection of peer-reviewed research and review articles from Nature Publishing Group.* World Scientific (2011) 171-179.
7. M. De Rosa, C. Nardini, C. Piccolo, C. Corsi, and F. D'amato, Pressure broadening and shift of transitions of the first overtone of HCl. *Applied Physics B* 72 (2001) 245-248.
8. J. Kibsgaard, T.R. Hellstern, S.J. Choi, B.N. Reinecke, and T.F. Jaramillo, Mesoporous ruthenium/ruthenium oxide thin films: active electrocatalysts for the oxygen evolution reaction." *ChemElectroChem* 4 (2017) 2480-2485.
9. D. Kong, J.J. Cha, H. Wang, H.R. Lee, and Y. Cui, First-row transition metal dichalcogenide catalysts for hydrogen evolution reaction. *Energy & Environmental Science* 6 (2013) 3553-3558.
10. M.S. Faber, R. Dziejic, M.A. Lukowski, N.S. Kaiser, Q. Ding, and S. Jin, High-performance electrocatalysis using metallic cobalt pyrite (CoS<sub>2</sub>) micro-and nanostructures." *J. Am. Chem. Soc.* 136 (2014) 10053-10061.
11. D. A. C. Brownson, D. K. Kampouris and C. E. Banks, *J. Power Sources*, 2011, 196, 4873-4885.



12. D. -W. Wang and D. Su, *Energy Environ. Sci.*, 2014, 7, 576-591.
13. D. Higgins, P. Zamani, A. Yu and Z. Chen, *Energy Environ. Sci.*, 2016, 9, 357-390.
14. X. Zhou, J. Qiao, L. Yang and J. Zhang, *Adv. Energy Mater.*, 2014, 4, 1301523-1301547.
15. Morozan, B. Jousselme and S. Palacin, *Energy Environ. Sci.*, 2011, 4, 1238-1254.
16. N. Markovic, T. Schmidt, V. Stamenkovic and P. Ross, *Fuel Cells*, 2001, 1, 105-116.
17. K. Uosaki, G. Elumalai, H. Noguchi, T. Masuda, A. Lyalin, A. Nakayama and T. Taketsugu, *J. Am. Chem. Soc.*, 2014, 136, 6542-6545.
18. O. T. Holton and J. W. Stevenson, *Platinum Met. Rev.*, 2013, 57, 259-271.
19. M. Gara and R. G. Compton, *New J. Chem.*, 2011, 35, 2647-2652.
20. D. Geng, Y. Chen, Y. Chen, Y. Li, R. Li, X. Sun, S. Ye and S. Knights, *Energy Environ. Sci.*, 2011, 4, 760-764.
21. E. P. Randviir and C. E. Banks, *Electroanalysis*, 2014, 26, 76-83.
22. U. Kramm, in *Encyclopedia of Applied Electrochemistry*, ed. G. Kreysa, K. -i. Ota and R. Savinell, Springer, New York, 2014, ch. 204, pp. 909-918.
23. J. Yin, J. Jin, H. Zhang, M. Lu, Y. Peng, , B. Huang, P. Xi, and C.H. Yan, Atomic Arrangement in Metal- Doped NiS<sub>2</sub> Boosts the Hydrogen Evolution Reaction in Alkaline Media. *Angew. Chem. Int. Ed.* 131.51 (2019) 18849-18855.
24. M.A. Lukowski, A.S. Daniel, F. Meng, A. Forticaux, L. Li, and S. Jin, et al. "Enhanced hydrogen evolution catalysis from chemically exfoliated. *J. Am. Chem. Soc.* 135 (2013) 10274.
25. K. Jiang, B. Liu, M. Luo, , S. Ning, M. Peng, Y. Zhao, Y.R. Lu, T.S. Chan, F.M. de Groot, and Y. Tan, Single platinum atoms embedded in nanoporous cobalt selenide as electrocatalyst for accelerating hydrogen evolution reaction *Nat. Commun.* 10. (2019)1-9.
26. C. Liu, T. Gong, J. Zhang, X. Zheng, J. Mao, H. Liu, Y. Li, and Q. Hao, Engineering Ni<sub>2</sub>PNiSe<sub>2</sub> heterostructure interface for highly efficient alkaline hydrogen evolution. *Applied Catalysis B: Environmental* 262 (2020) 118245.
27. D. Gao, J. Zhang, T. Wang, W. Xiao, K. Tao, D. Xue, and J. Ding, Metallic Ni<sub>3</sub>N nanosheets with exposed active surface sites for efficient hydrogen evolution. *J. Mater. Chem. A.* 4 (2016) 17363-17369.
28. Q. Hao, S. Li, H. Liu, J. Mao, Y. Li, C. Liu, J. Zhang, and C. Tang, Dual tuning of nickel sulfide nanoflake array electrocatalyst through nitrogen doping and carbon

- coating for efficient and stable water splitting. *Catal. Sci. Technol.* 9 (2019) 3099-3108.
29. Y. Jing, X. Mu, C. Xie, H. Liu, R. Yan, H. Dai, C. Liu, and X.D. Zhang, Enhanced hydrogen evolution reaction of WS<sub>2</sub>-CoS<sub>2</sub> heterostructure by synergistic effect. *Int. J. Hydrog. Energy* 44(2019) 809-818.
  30. H. Tian, C. Fan, G. Liu, S. Yuan, Y. Zhang, M. Wang, and E. Li, Ultrafast broadband photodetector based on SnS synthesized by hydrothermal method. *Appl. Surf. Sci* 487 (2019) 1043-1048.
  31. P.M. Pataniya, M. Tannarana, C.K. Zankat, S.A. Bhakhar, S. Narayan, G.K. Solanki, K.D. Patel, P.K. Jha, and V.M. Pathak, Low-temperature Raman investigations and photoresponse of a detector based on high-quality WSe<sub>2</sub> crystals. *J. Phys. Chem. C* 124 (2020) 2251-2257.
  32. H. Tian, C. Fan, G. Liu, S. Yuan, Y. Zhang, M. Wang, and E. Li, Ultrafast broadband photodetector based on SnS synthesized by hydrothermal method. *Appl. Surf. Sci* 487 (2019) 1043-1048.
  33. X. Yang, and B. Li, Monolayer MoS<sub>2</sub> for nanoscale photonics. *Nanophotonics* 9 (2020): 1557-1577.
  34. J.Y. Xue, F.L. Li, Z.Y. Zhao, C. Li, C.Y. Ni, H.W. Gu, D.J. Young, and J.P. Lang, In situ generation of bifunctional Fe-doped MoS<sub>2</sub> nanocanopies for efficient electrocatalytic water splitting. *Inorg. Chem.* 58 (2019) 11202-11209.
  35. B. Hinnemann, P.G. Moses, J. Bonde, K.P. Jørgensen, , J.H. Nielsen, S. Horch, I. Chorkendorff, and J.K. Nørskov, Biomimetic hydrogen evolution: MoS<sub>2</sub> nanoparticles as catalysts for hydrogen evolution. *J. Am. Chem. Soc.* 127 (2005)5308-5309.
  36. D. Roy, S. Sarkar, S. Bhattacharjee, K.; Panigrahi, B.K. Das, K. Sardar, S. Sarkar, K.K. Chattopadhyay, Site specific nitrogen incorporation in reduced graphene oxide using imidazole as a novel reducing agent for efficient oxygen reduction reaction and improved supercapacitive performance. *carbon* 166 (2020 )361-373.
  37. D. Roy, K. Panigrahi, B.K. Das, U.K. Ghorui, S. Bhattacharjee, M. Samanta, S. Sarkar, K.K. Chattopadhyay, Boron vacancy: a strategy to boost the oxygen reduction reaction of hexagonal boron nitride nanosheet in hBN-MoS<sub>2</sub> heterostructure. *Nanoscale Adv.* 3 (2021) 4739-4749.
  38. L. Zeng, K. Sun, X. Wang, Y. Liu, Y. Pan, Z. Liu, D. Cao, Y. Song, S. Liu, and C. Liu, Three-dimensional-networked Ni<sub>2</sub>P/Ni<sub>3</sub>S<sub>2</sub> heteronanoflake arrays for highly

- enhanced electrochemical overall-water-splitting activity. *Nano Energy* 51 (2018) 26-36.
39. S.R. Kadam, A.N. Enyashin, L. Houben, R. Bar-Ziv, and M. Bar-Sadan, Ni–WSe<sub>2</sub> nanostructures as efficient catalysts for electrochemical hydrogen evolution reaction (HER) in acidic and alkaline media. *J. Mater. Chem. A*. 8.3 (2020)1403-1416.
  40. D. Escalera-López, Y. Niu, J. Yin, K. Cooke, N.V. Rees, and R.E. Palmer, Enhancement of the hydrogen evolution reaction from Ni-MoS<sub>2</sub> hybrid nanoclusters. *ACS Catal* 6.9 (2016) 6008-6017.
  41. S.R. Kadam, A.N. Enyashin, L. Houben, R. Bar-Ziv, and M. Bar-Sadan, Ni–WSe<sub>2</sub> nanostructures as efficient catalysts for electrochemical hydrogen evolution reaction (HER) in acidic and alkaline media. *J. Mater. Chem. A*. 8.3 (2020)1403-1416.
  42. P. Hu, G. Long, A. Chaturvedi, S. Wang, K. Tan, Y. He, L. Zheng, G. Liu, Y. Ke, Y. Zhou, and H. Jiang, Agent-assisted VSSe ternary alloy single crystals as an efficient stable electrocatalyst for the hydrogen evolution reaction. *J. Mater. Chem. A*. 7 (2019) 15714-15721.
  43. Ho, Yen-Teng, et al. "Layered MoS<sub>2</sub> grown on c-sapphire by pulsed laser deposition." *physica status solidi (RRL)–Rapid Research Letters* 9.3 (2015): 187-191.
  44. Q. Ni, Y. Bai, S. Guo, H. Ren, G. Chen, Z. Wang, F. Wu, C. Wu, Carbon nanofiber elastically confined nanoflowers: A highly efficient design for molybdenum disulfide-based flexible anodes toward fast sodium storage, *ACS Appl. Mater. Interfaces* 11 (2019) 5183-5192.
  45. T. Sun, J. Wang, X. Chi, Y. Lin, Z. Chen, X. Ling, C. Qiu, Y. Xu, L. Song, W. Chen, C. Su, Engineering the electronic structure of MoS<sub>2</sub> nanorods by N and Mn dopants for ultra-efficient hydrogen production, *ACS Catal.* 8 (2018) 7585-7592.

**CHAPTER 7**  
**CONCLUSION AND**  
**SCOPE FOR FUTURE**  
**WORKS**

## 7.1 Conclusion

In our first work, we have successfully separates the different layers of 2H-MoS<sub>2</sub>. Our inability to efficiently and precisely monitor nanosheet size, thickness, or concentration limits the use of liquid exfoliation, a crucial production technique. Using a standard tabletop centrifuge, we have created a straightforward and adaptable centrifugation method based on probe sonication to fast and efficiently separate liquid-suspended TMDs according to their mass. A variety of fractions (samples) with distinctly varied extinction spectra were produced by this process. The concentration measurement is based on the size independence of the low-wavelength extinction coefficient, whereas the measurements of size and thickness are based on the influence of edges and quantum confinement on the optical spectra. Because of the resulting controllability of concentration, size, and thickness, it is easier to create dispersions with certain properties, such as high monolayer content.

In our second work, we show that, as compared to pure MoS<sub>2</sub>, Zn doped MoS<sub>2</sub> has higher electrochemical activity for HER and ORR. More importantly, among the two Zn doped catalysts, MoS<sub>2</sub>-30 exhibits the highest HER and ORR performance with the shortest onset potential and the lowest Tafel plot, as well as good stability. This work thus offers a legitimate method for designing additional high-performance, low-cost transition-metal dichalcogenide electrocatalysts that exhibit four electron ORR pathways rather than the generation of hazardous H<sub>2</sub>O<sub>2</sub> at the intermediate.

## 7.2 Scope for Future works

The two-dimensional nanomaterial MoS<sub>2</sub> is incredibly intriguing because of both its new physical characteristics and its application potential. For a number of reasons; we view this as a noteworthy result. A simple spectroscopic method for determining thickness and lateral dimensions will be essential since it will make it much simpler to characterise dispersions of liquid-exfoliated nanosheets. These discoveries will also facilitate the fabrication of liquid-suspended nanosheets with controlled distributions of length and thickness. This will be essential for determining how size influences the fundamental physical properties of layered inorganic materials as well as for applications where nanosheet size is important (for example, by fluorescence spectroscopy in solution). These techniques are generic and can be used to a wide range of two-dimensional materials, including WS<sub>2</sub>, MoSe<sub>2</sub>, and WSe<sub>2</sub>. This study stresses the effect of the edge on the nanosheet's overall electrical and optical properties.

For the advancement of future energy, non-noble metal electrocatalysts with superior performance and financial advantages for the hydrogen evolution reaction (HER) and oxygen reduction reaction (ORR) are essential. MoS<sub>2</sub> based materials in particular, which are two-dimensional transition-metal sulphides, are thought to be excellent substitute catalysts for the HER and ORR, where doping engineering has shown to be an efficient technique to modify their electrocatalytic activity. Therefore, this work provides a reliable strategy to design other low-cost and high-powered transition-metal dichalcogenide electrocatalysts to exhibit four electron ORR pathways rather than toxic H<sub>2</sub>O<sub>2</sub> production at the intermediate. This work offers a feasible method to modulate the electronic structure of electrocatalysts for effective hydrogen production and oxygen reduction and provides an experience to design highly efficient Earth abundant electrocatalysts for future energy applications.